



5-2017

Development of Nuclear UnderGround Engineered Test Surrogates for Technical Nuclear Forensics Exploitation

Robert Boone Gilbreath
University of Tennessee, Knoxville, rgilbre2@vols.utk.edu

Follow this and additional works at: https://trace.tennessee.edu/utk_gradthes

 Part of the [Defense and Security Studies Commons](#), [Geochemistry Commons](#), [Military and Veterans Studies Commons](#), [Nuclear Commons](#), [Nuclear Engineering Commons](#), [Radiochemistry Commons](#), and the [Terrorism Studies Commons](#)

Recommended Citation

Gilbreath, Robert Boone, "Development of Nuclear UnderGround Engineered Test Surrogates for Technical Nuclear Forensics Exploitation. " Master's Thesis, University of Tennessee, 2017.
https://trace.tennessee.edu/utk_gradthes/4708

This Thesis is brought to you for free and open access by the Graduate School at TRACE: Tennessee Research and Creative Exchange. It has been accepted for inclusion in Masters Theses by an authorized administrator of TRACE: Tennessee Research and Creative Exchange. For more information, please contact trace@utk.edu.

To the Graduate Council:

I am submitting herewith a thesis written by Robert Boone Gilbreath entitled "Development of Nuclear UnderGround Engineered Test Surrogates for Technical Nuclear Forensics Exploitation." I have examined the final electronic copy of this thesis for form and content and recommend that it be accepted in partial fulfillment of the requirements for the degree of Master of Science, with a major in Nuclear Engineering.

John D. Auxier II, Major Professor

We have read this thesis and recommend its acceptance:

Howard L. Hall, Lawrence H. Heilbronn

Accepted for the Council:

Dixie L. Thompson

Vice Provost and Dean of the Graduate School

(Original signatures are on file with official student records.)

Development of Nuclear UnderGround Engineered Test Surrogates
for Technical Nuclear Forensics Exploitation

A Thesis Presented for the
Master of Science
Degree
The University of Tennessee, Knoxville

Robert Boone Gilbreath

May 2017

Copyright © 2017 by R. Boone Gilbreath
All rights reserved.

DEDICATION

To my family, with love:

My wife, Jessica, and our sons, Thomas and Samuel. Thank you for your unconditional love, abiding support, and longsuffering which enable me to chase my dreams.

My parents, Lonnie and Donna. Among countless other things too numerous to mention here, thank you for instilling in me the importance of education and the pursuit of academic excellence.

My brother, Bart. Thank you for your counsel and for unwittingly, incessantly motivating me to conquer the next obstacle in an endless quest to match your achievements.

ACKNOWLEDGEMENTS

I am exceedingly grateful to Dr. John Auxier, II whose steadfast friendship, guidance, and pursuit of excellence were critical to the success of this work. Thanks to Dr. Howard Hall for providing the impetus, counsel, and resources with which this endeavor was completed. Likewise, the consummate instruction and direction of Dr. Lawrence Heilbronn was crucial to this effort. Thank you all for serving as members of my thesis committee.

Dr. Matthew Cook, Dr. Vince Jodoin, and Mr. Richard Warren were invaluable in assisting with all manner of MCNP6, FAT, and PGG processes, respectively. Furthermore, I would like to recognize the contributions of Dr. Jerrad Auxier, Mr. Jonathan Gill, Dr. Andrew Giminaro, and MAJ Joshua Molgaard whose prior and concurrent work informed the processes and models essential to this work.

Thanks also to the gentlemen of Joint Task Force FATE: LTC Mike Shattan, MAJ Eric Francis, LCDR Saul King, LCDR J. R. Powers-Luhn, CPT Mark Quint, and CPT Adam Seybert. Your intellect, advice, and camaraderie made this experience both educational and enjoyable.

To my many family members, friends, teachers, and professors not aforementioned: thank you for your constant prayer, instruction, support, and confidence through this endeavor.

Most importantly I thank God, the Creator of all things, for the ability and opportunity to attempt understanding His handiwork. Without His infinite blessing, grace, and mercy I can do nothing: "...He that abideth in me, and I in him, the same bringeth forth much fruit: for without me ye can do nothing," John 15:5, KJV [1].

Funding of the research supporting this thesis and degree by the United States taxpayers through the United States Army's Advanced Civil Schooling program and the United States Military Academy Department of Physics and Nuclear Engineering is gratefully acknowledged. Any opinions, findings, conclusions, or recommendations expressed in this document are those of the author and do not necessarily reflect the views of the United States Army.

ABSTRACT

A method for formulation and production of Nuclear UnderGround Engineered Test Surrogates (NUGETS) based on notional improvised nuclear device (IND) detonations in an underground environment analogous to the Nevada National Security Site (NNSS) is presented. Extensive statistical analyses of precursory geochemical and geophysical characteristics are combined with an augmented surrogate debris cooling technique and predictive IND contributions from the ORIGEN Fallout Analysis Tool. Precursory and resultant elemental compositions, cooling curve calculations, and visual comparison of NUGETS to genuine underground debris are reported. Application of NUGETS methodology to future studies in urban, underground post-detonation technical nuclear forensic (TNF) analysis is suggested.

TABLE OF CONTENTS

Chapter One: Introduction	1
1.1 Impetus for Study.....	1
1.2 Technical Nuclear Forensics Applications	2
Chapter Two: Literature Review and Background.....	3
2.1 Effects of Underground Nuclear Weapon Detonations	3
2.1.1 Detonation Timeline	3
2.1.2 Ionizing Radiation	7
2.1.3 Thermal Radiation.....	9
2.1.4 Shock and Pressure Effects.....	11
2.2 Underground Nuclear Explosive Melt Debris	13
2.2.1 Precursor Composition	13
2.2.2 Formation Mechanisms	14
2.2.3 Physical Characteristics.....	18
2.2.4 Radioactive Properties	23
2.2.5 Surrogate Nuclear Explosive Melt Debris.....	25
Chapter Three: Simulation and Calculation Methods	27
3.1 Conditions and Assumptions	27
3.1.1 Notional Improvised Nuclear Device Characteristics	27
3.1.2 Model Environment – Geometry	29
3.1.3 Model Environment – Geophysical & Geochemical	33
3.2 Fission and Activation Product Models.....	38
3.2.1 Neutron Transport Model in Geologic Medium.....	38
3.2.2 Fallout Analysis Tool Simulations	39
3.3 Underground Debris Cooling Profile	40
Chapter Four: Statistical Calculation and Computer Modeling Results	44
4.1 Geochemical Precursor Composition.....	44
4.2 MCNP Neutron Transport Model Results	47

4.3	Fallout Analysis Tool Model Results	48
4.4	Cooling Function	52
Chapter Five: NUGETS Experimental Production Method.....		53
5.1	Equipment	53
5.1.1	Furnace	53
5.1.2	Crucibles.....	53
5.1.3	Analytical Balances	54
5.1.4	Infrared Thermometer.....	54
5.2	Chemical Matrix Preparation.....	55
5.3	Sample Firing Process.....	55
5.3.1	Furnace Heating.....	55
5.3.1	Olsen Cooling Program.....	56
Chapter Six: NUGETS Production Experimental Results		58
6.1	Visual Debris Characteristics and Comparison	58
6.2	Void Fraction Estimates.....	62
Chapter Seven: Conclusions and Future Work.....		63
7.1	Conclusions	63
7.2	Future Work	64
References.....		65
Appendices.....		71
Appendix I: Fission Yield Calculations.....		72
Appendix II: ANOVA Test Results		73
AII.1	ANOVA Results for Analyte Weight Fraction by Location, Indexed Alphabetically by Analyte	73
AII.2	ANOVA Results for Density by Depth, Location, Lithology, and Stratigraphy.....	90
AII.3	ANOVA Results for Water Content by Depth, Location, Lithology, and Stratigraphy.....	93
Appendix III: MCNP Input Deck.....		96
Appendix IV: Rash Oxide Matrices		103

Appendix V: Fallout Analysis Tool Data.....104
AV.1 WGPu IND Mass Fraction Results by Mass Number (A) and Time105
AV.2 WGPu IND Mass Fraction Results by Atomic Number (Z) and Time. 115
AV.3 WGU IND Mass Fraction Results by Mass Number (A) and Time120
AV.4 WGU IND Mass Fraction Results by Atomic Number (Z) and Time ..130
Vita134

LIST OF TABLES

Table 3.1 – WGPu IND characteristics.....	28
Table 3.2 – WGU IND characteristics.....	28
Table 3.3 – Elemental composition of 2017 Al alloy.....	29
Table 3.4 - Cavity radius estimates based on various methods.	32
Table 4.1 - Elemental composition of hydrous geochemical model precursor by mass percent.....	45
Table 4.2 – NNSS Area 20 geochemical precursor NUGETS matrix.	46
Table 5.1 – Furnace cooling program parameters.	56

LIST OF FIGURES

Fig. 2.1 – Graphic representation of a supercritical fission chain reaction [12].....	4
Fig. 2.2. – Illustration of an underground nuclear detonation cavity and chimney formation [13].....	6
Fig. 2.3 – Computer model of temperature profiles following the Anvil Cheshire detonation below the static water level [13].	19
Fig. 2.4 – Temperature profile of the post-detonation debris cavity five months after the Plumbbob Rainier test [26].	19
Fig. 2.5 – Beads (l & r) and elongated droplets (c) from Plumbbob Rainier (l & c) [27] and Whetstone Scaup (r) shots [17].	20
Fig. 2.6 – Representative U-NEMD sample textures: massive with lithic inclusions (l), highly vesicular (c) [17], and pumiceous (r) [27].	21
Fig. 3.1 – Surface sample location RR-31 relative to the U20N borehole site in the NNSS (red outline) [41], [42].....	34
Fig. 3.2 - Analyte concentration of the top ten major compounds found in NNSS geology for five representative locations by mass percent.	34
Fig. 3.3 – Geochemical analyte (t), bulk density (m), and water content (b) sample locations relative to U20N within Area 20 of the NNSS [41], [42]. ..	37
Fig. 4.1 – Cell-averaged neutron flux as a function of energy from the 1.50-m MCNP6 model with the total cross-section of ²³ Na.....	48
Fig. 4.2 - Isobaric mass fraction vs. time plot of WGPu-fueled IND debris as projected by FAT simulation.....	50
Fig. 4.3 - Isobaric mass fraction vs. time plot of WGU-fueled IND debris as projected by FAT simulation.....	51
Fig. 4.4 – Time-temperature cavity cooling function. The horizontal line represents ambient temperature ($T_{\infty}=26.85\text{-}^{\circ}\text{C}$).	52
Fig. 5.1 – Idealized cooling curve plot representing cavity cooling (blue) and furnace-controlled cooling (red).	57

Fig. 6.1 – Initial NUGETS production samples NV1-1A (l) and NV1-1B (r). 58

Fig. 6.2 – NUGETS samples NV1-1C (top-l) and NV1-1D (top-r) as compared to
beaded U-NEMD recovered from the Plumbbob Rainier cavity (bottom) [27].
..... 59

Fig. 6.3 – Two NUGETS NV2 samples (top) as compared to two U-NEMD
samples from Niblick Bilby (bottom-l) and Anvil Cheshire (bottom-r) [17]. 60

Fig. 6.4 – Experimental cooling profile for sample NV2-2.1B.....61

Fig. 6.5 – NV2-series samples prepared simultaneously in sealed, stacked
crucibles..... 62

LIST OF ABBREVIATIONS AND ACRONYMS

ANOVA – analysis of variance

App. – appendix

BSE – back-scatter electron (scanning electron microscopy)

CAS RN[®] – Chemical Abstracts Service Registration Number

Ch. – chapter

d – day

DOB – depth of burst

DOD – United States Department of Defense

DTRA – Defense Threat Reduction Agency

EMPA – electron microprobe analysis

FAT – Fallout Analysis Tool

g – gram; also, gravitational acceleration constant

h – hour

IND – improvised nuclear device

k_{eff} – effective neutron multiplication factor

kg – kilogram

kt – kiloton (of TNT)

MC&A – material collection and analysis

MCNP6 – Monte Carlo for n-Particles 6

MIDAS – materials identification and debris analysis solutions program

min – minute

ml – milliliter

mol – mole

NEMD – nuclear explosive melt debris

NNSS – Nevada National Security Site, formerly known as the Nevada Test Site
(NTS)

NUGETS – Nuclear UnderGround Engineered Test Surrogates

ORIGEN – Oak Ridge Isotope Generation and depletion code

OTA – Office of Technology Assessment

PGG – Petrographic, Geochemical, and Geophysical (database)

ppm – parts per million

s – second

SCALE – Standard Computer Analysis for Licensing Evaluation modular code
system

SEM-EDX – scanning electron microscopy with energy dispersive x-ray
spectrometry

shake – 1×10^{-8} s

RDX –hexahydro-1,3,5-trinitro-1,3,5-triazine, research department explosive;
CAS RN®: 121-82-4

SI-MS – secondary ion mass spectrometry

SQ – significant quantity

t – metric ton (i.e., tonne); also, time

TNF – technical nuclear forensics

TNT – 2-methyl-1,3,5-trinitro-benzene, trinitrotoluene; CAS RN®: 118-96-7

UCLRL – Lawrence Radiation Laboratory, University of California-Livermore;

now known as Lawrence Livermore National Laboratory

U-NEMD – underground nuclear explosive melt debris

USGS – United States Geological Survey

UT-RCOE – University of Tennessee Radiochemistry Center of Excellence

V&V – verification and validation

WG – weapon grade

wk – week

XRF – x-ray fluorescence

yr – year

CHAPTER ONE

INTRODUCTION

This chapter discusses the reasons for study of underground nuclear melt glass and the application of this study to post-detonation nuclear forensics—specifically as it pertains to surrogate underground nuclear explosive melt debris production.

1.1 Impetus for Study

The threats of both nuclear proliferation and nuclear terrorism have existed for over a decade and persist at present [2]. Because a credible attribution capability is believed to deter such acts, a set of mechanisms to achieve attribution is necessary. One such mechanism is nuclear forensics, which is defined as “the analysis of nuclear materials recovered from either the capture of unused materials [pre-detonation], or from the radioactive debris following a nuclear explosion [post-detonation] [3].” Thus, a nation’s capability to conduct nuclear forensics analysis is of crucial national importance and contributes to deter, mitigate, and attribute events of nuclear terrorism. The development of such capabilities is the subject of U.S. law, among the principle missions of numerous U.S. government agencies, and the focus of much professional and academic research [3], [4].

Each of the three most-recent breakout nuclear weapons states, North Korea (2006), Pakistan (1998), and India (1974) conducted its initial nuclear weapon test underground [5]. From the perspectives of stealth and radionuclide containment, it seems logical that any future proliferators may follow suit. Moreover, the threat of malicious non-state actors acquiring the materials and technology with which to execute acts of nuclear terrorism abides. These reasons have given rise to the focus of this investigation: understanding a portion of the myriad characteristics of underground post-detonation nuclear debris, the material which generally consists

a variably vitreous matrix that carries information on the composition and origin of the device.

Specifically driving this work is the plausibility of an attack wherein an improvised nuclear device (IND) is detonated in deep, subterranean, urban infrastructure (e.g., a subsurface parking structure below a high-rise building, a major subway station, etc.). While the probability of such an attack is open to debate, the catastrophic consequences resulting therefrom demand these incredible risks be addressed. It is proposed here that by understanding the contribution of geochemical and device constituents to forensic radiochemical indicators in debris formed in a “controlled” environment—one where many conditions and specifications of the system are well-characterized—that conclusions may be drawn about the same effects in an uncontrolled setting. In this case, the controlled environment is a sealed underground test cavity representative of the Nevada National Security Site (NNSS).

1.2 Technical Nuclear Forensics Applications

In this study, hypothetical values for nuclear forensics indicators are produced for two notional INDs detonated in representative NNSS geology using the Oak Ridge Isotope Generation (ORIGEN) Fallout Analysis Tool (FAT). These data inform chemical formulations which are employed with an empirically derived cooling function for the creation of a new type of surrogate nuclear debris, known here as Nuclear UnderGround Engineered Test Surrogates (NUGETS). These post-detonation surrogate debris samples may be exploited in a number of different ways to support material collection and analysis (MC&A), verification and validation (V&V), and paradigm-altering thrust areas within the current Defense Threat Reduction Agency (DTRA) materials identification & debris analysis solutions (MIDAS) program and the technical nuclear forensics (TNF) community at large [6].

CHAPTER TWO

LITERATURE REVIEW AND BACKGROUND

The literature review which follows covers journal articles, technical reports, and other information reported in the literature regarding topics specifically germane to this work from 1958 to present. This review is intended to provide a cohesive background with regard to the topics of radiation and physical damage mechanisms in nuclear detonations along with the phenomenology of those mechanisms in production of both genuine and surrogate post-detonation underground nuclear weapon debris.

2.1 Effects of Underground Nuclear Weapon Detonations

The effects of any nuclear detonation are a complex, multifaceted result of perhaps the even more complicated process which causes the detonation—prompt supercritical fission. An exhaustive presentation of the physical and thermodynamic processes involved in nuclear detonations is given by Bridgman and is well-supplemented for practicality by Moody, Grant and Hutcheon; Glasstone and Dolan; and Serber [7]–[10]. For ease of discussion, the effects of an underground nuclear detonation considered in this study are categorized into three areas: ionizing radiation, thermal radiation, and shock/pressure. While these three are not mutually exclusive because one or more often contribute to the other(s), it is convenient to think of the effects in this way. The application of these effects is addressed further in §2.2 with regards to influence on the formation of underground nuclear debris.

2.1.1 Detonation Timeline

Before delving how the specific effects of an underground nuclear detonation are achieved, it is instructive to deliver a general timeline of events which occur

during and immediately following the fission detonation itself. Various sources report the numerous aspects of the detonation timeline, but a 1989 report by the U.S. Congress Office of Technology Assessment (OTA) provides an excellent summary [11]. The following discussion is derived principally from the OTA document with additional details provided by other sources as noted.

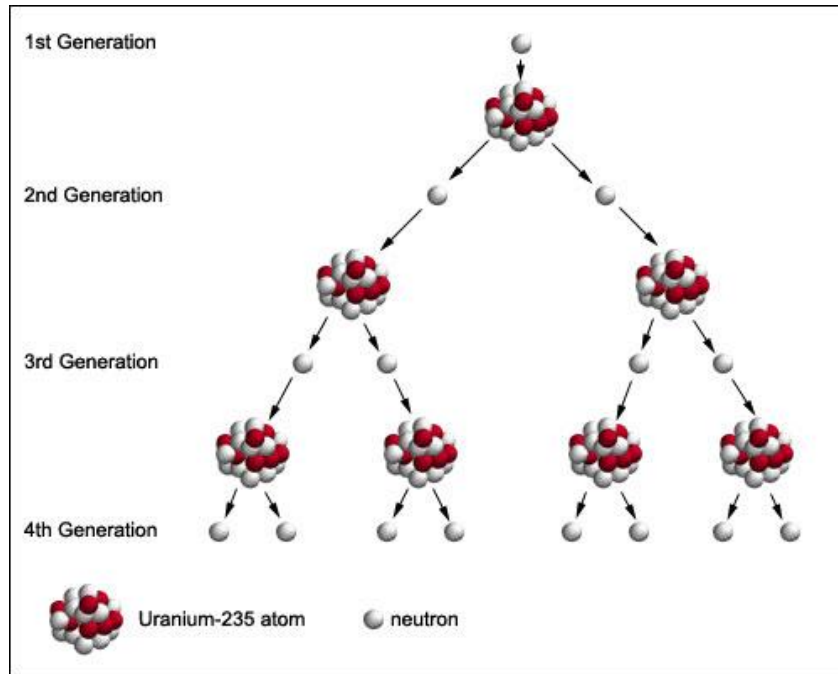


Fig. 2.1 – *Graphic representation of a supercritical fission chain reaction* [12].

Prior to the time of ignition, referred to here as $t_0 = t = 0$, interactions of firing mechanisms and other weapon elements modify the subcritical fissile material in the device's core such that prompt supercriticality ($k_{\text{eff}} \gg 1$) is achieved (cf. Fig. 2.1). With these modifications, a quantity of free neutrons introduced to the system gives rise to the first generation of fissions within the fissile material. Given the supercritical configuration, the first generation of fission neutrons begets a larger second generation which produces an even greater third generation and so forth. The exact measure of a neutron's lifetime—that is the time from which it is

introduced or “born” into the system until it is absorbed or leaves the system—is variable with the physical state of the system, but a common approximation of this time is 1×10^{-8} s, or 1 “shake,” colloquially [7].

As tens of generations of fissions occur, the very high energy density of the fissioning fuel causes the device to expand at an explosive rate. This expansion combined with depletion of the fissile mass by the fission process itself, drives the fuel out of the supercritical state [7]. Eventually the fission reaction ceases ($k_{\text{eff}} = 0$) in a process commonly referred to as mechanical disassembly. During the fractions of a microsecond (<100 shakes) for which the supercritical fuel assembly is maintained, several moles of fuel atoms fission, each releasing approximately 200 MeV—on the order of several tens of kilotons (kt) of 2-methyl-1,3,5-trinitrobenzene (i.e., TNT, CAS RN®: 118-96-7) total. Pressures generated by this activity reach the order of 10^6 psi, and temperatures generated in the device reach the order of 10^8 K. At this point, the explosive energy deposition creates a shock wave which begins to move outward from the device [9], [11].

Within the following milliseconds (10^5 shakes), the remaining matter from the device and the immediate, surrounding geologic media are vaporized. The intense heat creates a gaseous bubble of very high pressure. This pressure, added to explosive momentum created by the rapid expansion of the device (shock wave) begins to create a spherical cavity within the underground media [11].

In the next few tenths of a second (10^7 shakes), the pressure and momentum previously imparted to the surroundings are equalized by the pressure of the bounding rock and soil. At this point, the cavity reaches its maximum dimensions. The shock wave continues outward from the cavity, crushing rock immediately beyond the cavity, permanently compressing the rock beyond that, and elastically compressing rock and soil even farther out. The elastically compressed media

subsequently relaxes creating seismic waves which propagate through the surrounding earth similar to the action of an earthquake [11].

On the order of a few seconds ($10^8 - 10^9$ shakes), the vaporized and molten debris begins to condense and solidify on the surfaces of the cavity (cf. §2.2, Fig. 2.2). As the cavity cools, pressure drops, and the fluid rock begins to flow down the walls, pooling in the bottom of the cavity [11].

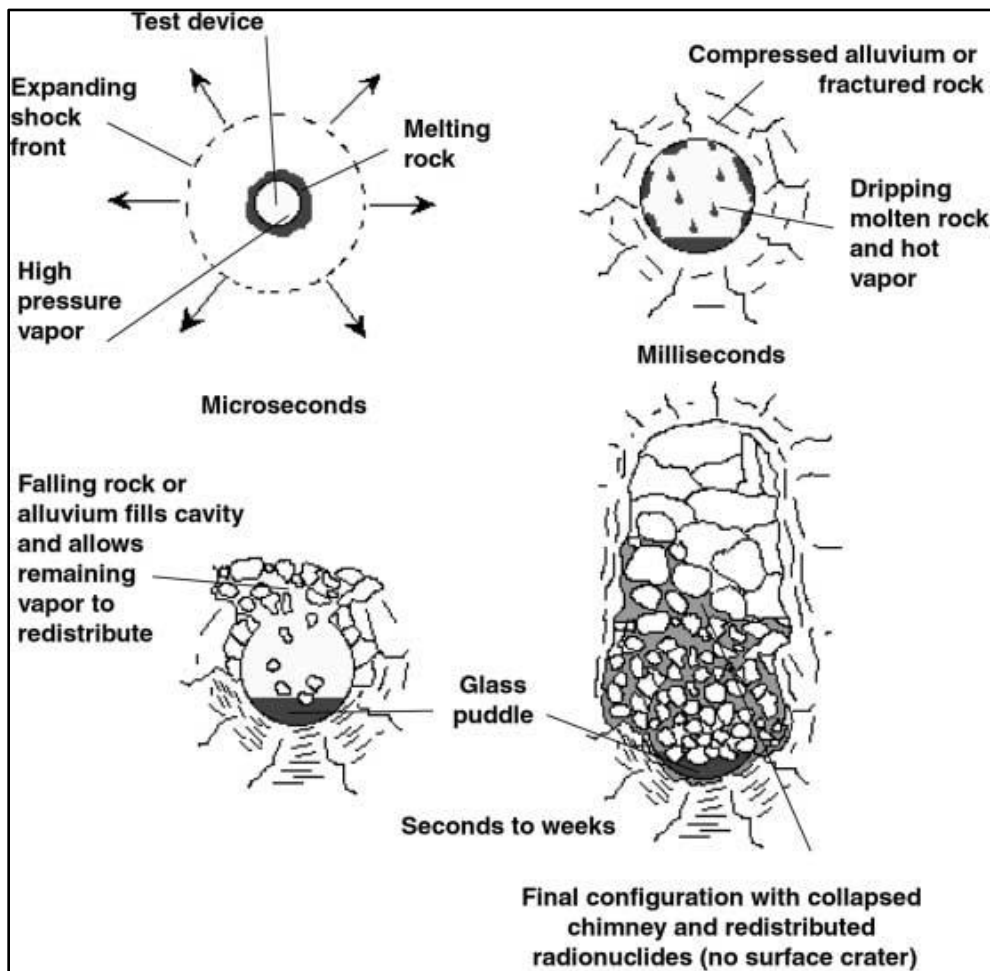


Fig. 2.2. – Illustration of an underground nuclear detonation cavity and chimney formation [13].

Finally, in the following minutes, hours, or longer ($>10^{10}$ shakes), the glass pool at the bottom of the cavity cools and solidifies. As the cavity cools, the gas pressure within the cavity drops such that it is exceeded by the weight of the overburden. If the overburden is highly fractured or otherwise unstable, a chimney is created by the crushed rock falling from above and filling in the cavity (cf. Fig. 2.2). This effect continues upward until the void is stabilized by mutually supporting rubble, unaffected rock is able to support the remaining overburden, or the chimney reaches the surface forming a retarc (i.e., a subsidence crater). The chimney and retarc formation processes are generally the last notable effects of the detonation and may take months ($>10^{12}$ shakes) to occur [11].

2.1.2 Ionizing Radiation

The ionizing radiations resulting from a nuclear weapon detonation takes many forms and arise from many diverse processes. Alpha (α) particles, beta (β^\pm) particles, photons (γ -rays and x-rays), and neutrons (n), of myriad energies are released from the fuel, fission fragments, and irradiated device components [7], [9]. This mixed radiation field may be further subcategorized into two very general time-dependent groups, prompt and delayed (residual). Prompt radiation is loosely defined as that which occurs within 1 min of the detonation [9]. For purposes of this study, the prompt fraction is of primary concern as most physical processes involved in debris formation result from this portion.

Forsaking a rigorous presentation of fission thermodynamics and particle transport which may be found in Bridgman's text, the processes which drive the prompt ionizing radiation source term in a nuclear detonation are summarized here [7]. The majority of the discussion will focus on photon production and interaction, as some 70-80% of the weapon yield occurs in the form of photon radiation [7], [9]. Nonetheless, a discussion of this type which neglects the other forms of radiation would be incomplete at best.

Alpha and both charge states of β particulate radiation result predominantly from the unstable state of the fissile material and the resulting fission fragments, respectively. While significant contributors to the overall residual radioactivity (and decay heat load) at late times, the contribution of these source terms to the prompt inventory is largely insignificant [9]. For these reasons, discussion of α and β^\pm radiations are often minimized in the literature. Likewise, the direct contribution of neutrons and prompt gamma rays to physical detonation effects are somewhat insignificant ($\approx 3\%$ of the total energy) [9]. While these radiations emanate from various processes and produce notable dosimetric effects, the influence of neutron and gamma radiation on physical, debris-producing damage is relatively small. Beyond physical damage, the IND's neutron spectrum and flux do play a vital role in driving the radiochemical composition of the post-detonation debris through activation interactions with device components and elements of the local blast environment [9].

The dominant form of prompt ionizing radiation produced in a nuclear detonation is that of x-rays. The large population of x-rays which emanates from a nuclear weapon are first born of fission in the weapon's fissile core within the first 100-shakes. Kinetic interactions of fission fragments with neighboring matter drive temperatures of the core exponentially higher within the first few tens of generations. As the internal system energy increases, ionization occurs, freeing high-energy electrons which undergo coulombic interactions with nuclei, ions, and other free electrons producing bremsstrahlung photons. These photons subsequently undergo Compton and Rayleigh scatter as well as photoelectric interactions according to the photon wavelength and applicable material cross-sections. As temperatures in the core rise to $>10^7$ K (on the order of keV), free electrons are driven to local thermodynamic equilibrium with the surrounding system. This gain of kinetic energy along with the short mean free path between coulombic interactions with other ions in the system produces increasing numbers of even higher energy photons [7].

As these photons propagate through media surrounding the fissile material (e.g., high-Z tamper, low-Z chemical explosive byproducts, medium-Z case, etc.), they continue to undergo scattering and absorption reactions according to energy and material cross-sections. With each successive interaction, the photon spectrum decreases in total intensity, although it may become harder (due to absorption of low-energy photons), or softer where scattering interactions dominate. As these interactions occur, energy is imparted to the surrounding materials in a very short amount of time which corresponds to the length of the x-ray pulse (i.e., a few shakes). Given this extreme energy deposition in an infinitesimal time, inertia forbids significant movement of the absorber atoms which essentially undergoes an instantaneous internal energy gain. This rapid change in systemic energy density causes ionization and reemission of secondary photons at close ranges and is the driving force behind thermal and pressure effects which will be discussed in the following subsections [7].

2.1.3 Thermal Radiation

Oftentimes in the literature, thermal radiation is often directly associated with or considered part and parcel of the prompt ionizing radiations discussed in §2.1.2. Thus, what is meant by prompt “thermal radiation” in the context of this work shall be specified. Adhering to the previous delineation between prompt and residual radiation, thermal radiations in this discussion are those which (regardless of initial form) have downscattered into the ultraviolet, visible, or infrared spectra, imparting thermal energy (i.e., heat) to the immediate surrounding media by absorption and inelastic scatter. Thermal radiation results from approximately half the total x-ray yield of the device (i.e., $\approx 35\%$ of the total energy yield) [9].

Aside from the negligible thermal energy released by the conventional explosives, essentially all thermal radiation and damage resulting therefrom is produced secondary to the x-ray pulse described in §2.1.2. The intense x-ray pulse

from an underground detonation is absorbed and reradiated in a distance on the order of 10^3 less than in air [7]. As the ionization and reradiation processes take place, a plasma sphere or “fireball” is created. The fireball’s growth is best considered in three stages: burnout, diffusion, and hydrodynamic growth [7].

Following its development, the fireball very quickly radiates to an extent at which downscatter, absorption, and radial dispersion preclude the photons from completely ionizing the environment to any greater extent. This point—at which all the prompt fission x-radiation is considered consumed—is commonly referred to as burnout [7].

After burnout, the fireball continues to grow via thermal diffusion. The thermal reradiation created by burnout x-rays expands ever outward, depositing photon energy over an increasing spherical volume at ever decreasing temperatures. As this effect propagates, the fireball growth rate eventually falls below the speed of sound in the surrounding medium—a point referred to as hydrodynamic separation. The temperatures at hydrodynamic separation in an underground detonation are of the order of 10^7 K; pressures at this point reach 10^7 psi [7]. The thermal radiation combined with the compression caused by kinetic energy transfer and surface ablation (i.e., the causes of the shock wave) at the moment of hydrodynamic separation are sufficient to ionize, vaporize, and melt the rock surrounding the device at hydrodynamic separation. Because of the density of the surrounding geologic media, hydrodynamic separation in an underground blast is estimated to occur at the outer skin of the fully ionized device [7].

During the hydrodynamic growth phase, the fireball continues to grow, ever more slowly as it is outpaced by the phonon shock front [7]. Because the many visual and spectroscopic techniques used to characterize fireball growth in atmospheric testing are precluded by the earth itself, underground fireball propagation is not as well defined [9]. Nevertheless, the hydrodynamic phase of

underground fireball growth may be considered as sequential absorption and reradiation of thermal energy across differential radii of a growing sphere behind the shock front. This process will continue outward until essentially all photons are absorbed and the fireball is extinguished.

2.1.4 Shock and Pressure Effects

Shock and pressure effects in an underground detonation occur principally by the near-instantaneous deposition of x-radiation energy into the medium surrounding the device [7]. This rapid deposition affects the absorbing medium in one of two ways. In the first case, the x-radiation is so intense that it exceeds the latent heat of vaporization of the material. The vaporized material is blown off and imparts an exhaust momentum into the adjacent layer of material in a very short amount of time. In the second case, the x-radiation intensity is such that it remains below the material's vaporization threshold, but still imparts significant energy very rapidly. The pressure created by this impulse of energy is shown in eq. 2.1.

$$p(x) = \gamma_s \rho_o E_{dep}(x) \quad (2.1) [7]$$

where

- $p(x)$ is the pressure at depth, x , in the material,
- γ_s is the Grüneisen constant, a material property,
- ρ_o is the original material density, and
- $E_{dep}(x)$ is the internal energy deposited at depth x .

Like the fireball, once initiated, the shock wave propagates outward from the device in three sequential phases: hydrodynamic, plastic, and elastic [7]. While the plastic and elastic phases are of crucial importance in estimating physical damage to coupled structures, they are of little import to debris formation. Thus, this study is most concerned with the hydrodynamic phase of the shock wave. As discussed in §2.1.3, the temperature and pressure of the shock wave at the time of

hydrodynamic separation are of the order of 10^7 at a fraction of a meter from the point of detonation (i.e., the surface of the device casing) [7].

The hydrodynamic shock wave will propagate outward, losing energy as it travels. In the early time, the kinetic energy transfer will remain sufficient to shock melt the surrounding geologic media by means of compression out to several meters from the working point [11]. The extent of this melt will later be assisted by the diffusive growth of the thermal fireball behind it, but is bound by the material properties of the earth at the shock front location. In order to shock melt the rock, the E_{dep} term of eq. 2.1 must exceed the latent heat of fusion of the material according to the current equation of state, as a function of geochemistry, water content, and material phase under high temperature and pressure.

Immediately following the hydrodynamic phase comes the plastic phase of the shock wave. It is in this phase where the maximum cavity dimensions are achieved in a contained underground detonation [7], [9]. This dimension will drive the cooling of the cavity and the, ionized, vaporized, and melted debris within it and will be dealt with specifically in §3.1.2 [14]. In the plastic phase, the shock wave has lost enough energy that it is no longer able to ionize or melt the medium through which it is traveling. However, its pressure is sufficient to plastically deform the layers of rock just beyond the shock-melted mass. Due to these intense compressive forces, the medium's modulus of elasticity is exceeded and it is unable to rebound to its original position. Subsequently, the further degraded shock wave continues outward, elastically disturbing the soil and rock at distances greater than three cavity radii from the working point [11]. These elastic compression and relaxation cycles form the beginning of seismic disturbances felt at great distances from the detonation [7].

2.2 Underground Nuclear Explosive Melt Debris

Discussed in this section are the composition, mechanisms of formation, physical properties, and radiological properties of underground nuclear explosive melt debris (U-NEMD). The acronym U-NEMD is adapted from Smith's NEMD terminology due to the variable crystalline and vitreous nature of the debris (cf. §2.2.3) [15]. In this context, U-NEMD is considered as those substances which are physically altered from their original (usually crystalline or metallic) state by the heat and pressure of the nuclear explosion such that they condense and solidify in a vitreous matrix upon return to ambient temperature and pressure. Generally, the discussion is concerned with the bulk melt debris contained within the cavity described in the preceding sections. It is noteworthy, however, that glassy debris may be found in the extra-cavity environment where temperatures exceed material melting points, or where plasma and vapor condensate are promptly injected into preexisting fissures during the detonation process [16], [17].

A brief discussion of various methods of surrogate nuclear melt debris formulation and production is included as reference for the attempt made at surrogate U-NEMD production in this work.

2.2.1 Precursor Composition

Given the essentially closed nature of the system involved in a deep underground nuclear detonation, the composition of the debris precursor is somewhat easily bound. The expected elemental composition of the debris is derived primarily from the host geochemistry with additional contributions from residual device components (e.g., case, high explosive, tamper, fissile material, etc.), activation products (including portions of both previous categories), and fission products corresponding to the consumed fuel and tamper masses [15], [18]–[21]. In a testing environment, significant contributions may be expected

from stemming materials (i.e., media used to backfill an underground test emplacement borehole), and to a lesser degree, downhole instrumentation and other associated infrastructure within the cavity radius [15]. In the case of an urban detonation, the composition is likely to become significantly convoluted by the presence of various layers of infrastructure (e.g., building materials, pipelines, subway trains, etc.) with highly variable bulk compositions [22].

Estimates reported in the literature, which vary by a factor of five, claim between 500 and 2,500 metric tons of geologic media are vaporized or melted per kiloton yield in an underground detonation [14], [15], [21], [23]–[27]. Given the relatively small mass of an IND and the even smaller mass of fuel—and thus, fission products—present, the major contributors to debris mass are the surrounding geology and the activation products induced in situ. Host geochemical and geophysical properties which directly affect debris composition and formation are diverse and multivariate (cf. §3.1.3). Variability notwithstanding, in the case of the United States testing program, pre-shot geochemical inventories were acquired and catalogued. These data aid in predicting debris composition, and thusly, serve as a baseline for this study. From a forensics perspective, geophysical and geochemical variation may be confounding in the case of investigating clandestine or illicit testing in restricted areas, but construction records and land survey data should provide limited assistance in bounding urban scenarios.

Detonation phenomenology and the rate of cavity cooling affect the debris formation process, final nuclide composition, physical, and radiological properties [15]. These factors are discussed in the following sections.

2.2.2 Formation Mechanisms

In the past seven decades, a great deal has been composed on the effects of underground nuclear detonations vis-à-vis debris formation mechanisms and

phenomena. This discussion considers sixteen such documents composed from 1958-2016 and focuses on data that is pertinent to bulk debris formation [7], [13]–[17], [19], [21], [24]–[31]. Moreover, it focuses on that which pertains to surrogate debris formulation and production in a laboratory setting.

The generally espoused U-NEMD formation process centers on phenomenology which occurs shortly after the blast cavity reaches its maximum size. At this point, the cavity is essentially filled with a mix of fully and partially ionized matter, vaporized matter, and superheated steam at high pressure. At the same time, it is lined with shock-heated molten and fused layers of rock which are held in place for a short time by the elevated cavity pressure [7], [17]. The condensate and precipitate from the plasma and vapor along with the molten and fused cavity lining which compose the bulk U-NEMD are those in which this study is primarily interested [17], [19], [30].

Within the next few seconds, expansion of the plasma and gas within the chamber and through fissures in the crushed rock as well as conductive heat transfer to the surrounding earth cause the cavity to begin cooling. As this cooling occurs, deionization and condensation processes ensue. It has been reported in multiple cases that the cooling and deionization processes in a post-detonation environment results in the alteration of the relative concentrations of naturally present oxidation states of debris species [19], [24], [25]. Specifically, Fe is seen enriched in the divalent versus the trivalent state when compared with the geochemical precursor in which Fe^{2+} is rarely reported as it is uncommon in nature [19], [25]. Likewise, one study reports redox effects on U and Pu species in both underground and near-surface nuclear detonations [19]. In the samples considered, U is found oxidized from the metallic state to the hexavalent and tetravalent states with U^{6+} being the dominant form. Plutonium is reported only as oxidized to the tetravalent state. Such phenomena are highly variable and seem to demonstrate tenuous relationships to the proximity of the element to any

quenching device (e.g., surrounding rock, air, water, etc.) as well as the redox state of the precursor media [19], [25].

Upon dissipation of the plasma, the quickly cooling matter begins to undergo phase transitions as a function of partial vapor pressures, boiling points, and freezing points [13], [21]. The order in which elements and compounds tend to condense and solidify leads to a classification of debris constituents as generally refractory or generally volatile. These definitions vary widely based upon the detonation scenario (i.e., underground, underwater, near-surface, above ground, high-altitude) and are employed here in a manner befitting those products which will remain gaseous, suspended vapors, or surface deposits (volatile) versus those which will remain in the liquid or solid phase (refractory) as the cavity environment returns to ambient temperature and pressure.

As a matter of course, the most refractory species condense first. Condensable gasses liquefy and begin to collect on the surface of cavity walls while a small fraction are reported to condense and begin to solidify in suspension [15], [19]. The refractory species include approximately 60-85% of fission and activation products, residual fuel actinide species (i.e., U and Pu), and the majority of geophysical precursor material [15], [25], [26]. On the same order of time (several seconds), pressure within the cavity decreases such the molten condensate on the ceiling and walls of the cavity begins flowing downward under the influence of gravity [13], [19], [21], [26]–[29]. As the melted debris flows down the walls, mixing occurs between shock melted debris, molten refractory debris, condensing vapors, and crushed solids from the roof and walls of the cavity [15], [28]. This flow ultimately collects in a thick, lens-shaped pool of U-NEMD on the floor of the cavity which contains 95-98% of all glassy U-NEMD formed during the detonation [15], [17], [19], [21], [24], [26], [27].

The U-NEMD that pools on the cavity floor consists primarily of refractory debris products and is well-depleted in volatile products [15], [17], [21], [24], [26], [30]. It is reported that the pooled melt is generally well-mixed and shows no major elemental migration, but microscopically the glass demonstrates chemical heterogeneity [24]. As the cavity continues to cool and pressures continue to decline toward the ambient, more volatile species condense and are deposited on the surface of bulk debris and within fissures adjacent to the cavity [15]. This process is the unique nature of fractionation within a contained underground detonation versus the field-wide fractionation experienced in an above ground detonation [30].

As noted in numerous studies, a critical difference between underground debris formation and that in other detonations is the duration of cooling [30], [31]. The thermal gradient and prolonged cooling in the post-detonation cavity influences debris morphology, mixing, and chemistry [19]. Dissipation of a thermal source term which has driven many thousands of tons of rock to temperatures at least on the order of 10^3 K through highly insulating media is a very slow process compared to that of an air or water burst [14], [26], [27]. In order to estimate the cooling duration, a 1967 study by Olsen applies Newtonian cooling principles to the cavity cooling problem. He derives an empirical relationship between cavity temperature and time as a function of cavity radius, yield, bulk water content, and various thermophysical properties of the local geology [14]. While the relationship fits experimental data well, several thermophysical properties are not well-defined in the very unique environment with which the study is concerned. It appears at present that Olsen's derivation is the only readily accessible means by which to evaluate the time-dependent temperature of the post-detonation cavity. Thus, his method is employed in this work as a surrogate U-NEMD production modifier (cf. §3.3 and §5.3.1).

It suffices to say, the debris solidification process begins within seconds of detonation and extends over many subsequent minutes, hours, or days [15], [17], [19]. The exact time to solidification is difficult to ascertain as it is a function of many variables including chemical composition, location within the debris puddle relative to an ambient temperature source, yield of the weapon, etc. [17]. The cavity cooling and debris solidification processes are also affected by various external phenomena. Internal pressure and temperature gradients ($\leq 3.6 \times 10^4$ K/cm at the wall-melt interface) cause crushed overburden to fall from the chimney and spall from walls into the cavity becoming entrained in the molten pool of debris [7], [14], [15], [17], [21], [26], [29]. The introduction of this relatively cool geologic media as well as the reintroduction of groundwater in detonations below the water table into contact with the melt pool accelerate the cooling by natural conduction [13]. These intrusions cause localized debris quenching and chemical alteration layer formation to occur. A computer model of one such scenario where groundwater flow contributed to cavity cooling in the Anvil Cheshire shot is shown in Fig. 2.3. According to the empirically derived model by Maxwell, et al, a duration of 50 years or greater may be necessary to fully dissipate the initial thermal load from a large detonation in saturated volcanic tuff. A similar study by Johnson, et al, recorded temperatures in excess of 77 K above ambient in the Plumbbob Rainier melt pool five months post-detonation (cf. Fig. 2.4) [26].

2.2.3 Physical Characteristics

The aforementioned formation mechanisms (cf. §2.2.2) result in a collection of very diverse, heterogeneous U-NEMD both inside and immediately adjacent to the blast cavity. Underground debris varies in physical shape, size, texture, color, crystallinity, location, and amount and type of inclusions.

As noted, the majority of U-NEMD is contained in a large, continuous, lens-shaped puddle which coalesces at the bottom of the post-detonation cavity and

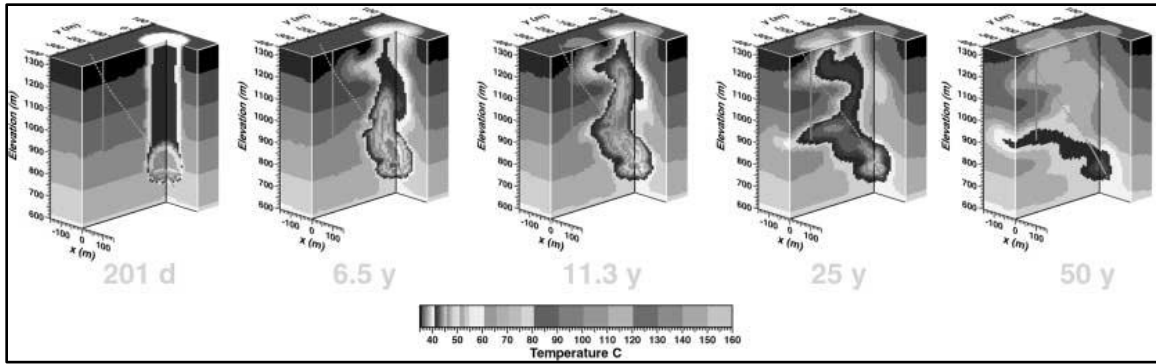


Fig. 2.3 – Computer model of temperature profiles following the Anvil Cheshire detonation below the static water level [13].

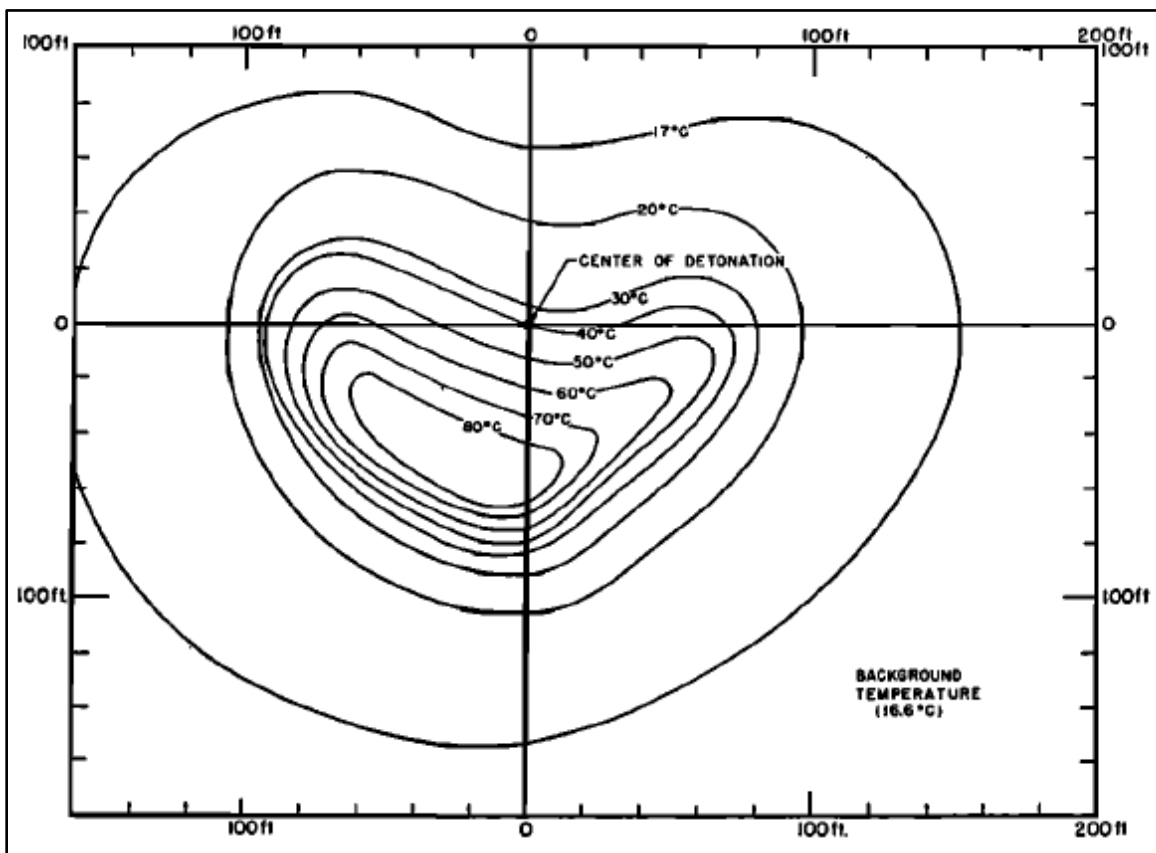


Fig. 2.4 – Temperature profile of the post-detonation debris cavity five months after the Plumbbob Rainier test [26].

may be up to 20-ft thick [17], [32]. However, numerous studies have recorded various physical forms of U-NEMD in addition to the puddled debris. The large puddle is usually accompanied by coatings, splashes, and smears of U-NEMD on the walls, ceiling, and fractured host rock debris throughout the cavity which is formed when crushed host rock falls into the molten pool [21], [24], [32]. Additionally, prompt injection of vaporized and/or molten debris into preexisting fissures in the host geology forms thin seams of glassy debris [17], [32]. Stringers of debris may hang from the cavity ceiling, frozen in place by the high viscosity of the molten debris and the rapid cooling of the cavity [17].

Ubiquitous to most underground detonations is the formation of numerous teardrop-shaped to spheroidal beads of U-NEMD in a wide range of sizes from dust-like to larger beads with diameters in excess of $\frac{3}{4}$ in (cf. Fig. 2.5). These debris typically result from rapid vapor condensation of Si compounds and from molten debris dripping from wall and ceiling surfaces. Some remain essentially round implying solidification before impact on the cavity floor, while others exhibit flattened bottom surfaces suggesting a viscous property remained at impact [27].

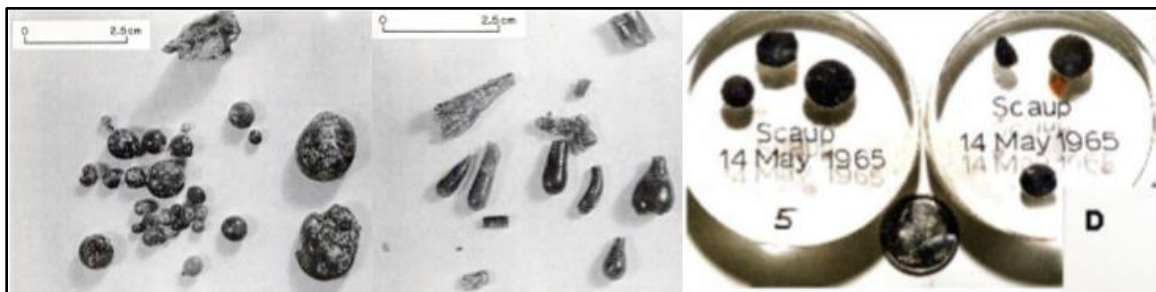


Fig. 2.5 – Beads (l & r) and elongated droplets (c) from Plumbbob Rainier (l & c) [27] and Whetstone Scaup (r) shots [17].

The various physical forms of U-NEMD demonstrate heterogeneous textures, both in an individual specimen and throughout the blast cavity as a whole.

Individual samples exhibit a wide range of vesicularity. Some are massive and void of vesicles, some highly vesicular, and others are pumiceous [17], [24], [30]. Vesicularity seems to indicate outgassing of incondensable gasses as cavity pressure drops while the debris remains near the liquidus temperature [32]. Particularly, steam is thought to be outgassed at this point which is demonstrated by the relative dehydration of U-NEMD compared to the precursor [24], [27]. The complex volume of U-NEMD which composes the puddled debris residing at the bottom of the cavity is characterized as dark, continuous, and variably vesicular with light, brecciated, lithic and mineral inclusions [13], [15], [17], [21], [32]. Debris beads are similarly variable in vesicularity. Generally, the thin coatings and splashes of debris which are found in direct contact with host rock are less vesicular than bulk debris due to rapid quenching [17]. In addition to vesicularity, some U-NEMD also exhibit preferentially oriented microfractures which are likely due to redistribution of residual internal stresses during the cooling process [21]. The U-NEMD from numerous detonations demonstrates no obvious relationship between debris texture and host rock type or device type [15], [17], [30]. Three representative samples of various U-NEMD textures are shown below in Fig. 2.6.

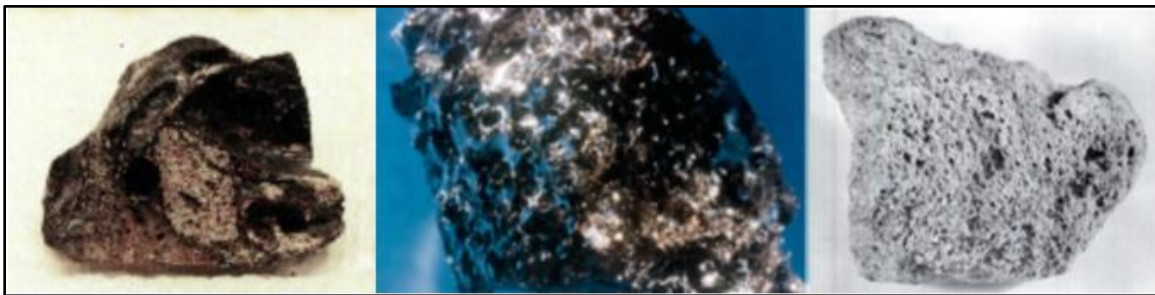


Fig. 2.6 – Representative U-NEMD sample textures: massive with lithic inclusions (l), highly vesicular (c) [17], and pumiceous (r) [27].

A wide variety of colors is characteristic of U-NEMD. Ranging the full spectrum from essentially black to nearly colorless, U-NEMD has been recorded in various

shades of brown, gray, green, red, and off-white [17], [28], [30], [32]. Color, not unlike many other characteristics appears to be heterogeneous, sometimes occurring in bands, laminae, or marbled swirls [24], [28]. Tenuous relationships have been drawn between color and chemical content, location, and radioactive properties (cf. §2.2.4). The majority of bulk U-NEMD found in the puddle tends to be dark brown or black. Greens and reds tend to occur in fused material above the puddled U-NEMD [32]. Dark brown glasses seem to be higher in Fe and Ti content while lighter “colorless” samples tend to have higher Si and Al content [24]. Darker glasses also seem to indicate higher concentrations of radioactive species than do lighter debris specimens [21], [24], [28].

The final major physical characteristic of U-NEMD is its crystalline or amorphous (i.e., vitreous) nature. The variation in crystallinity is likely due to duration of cooling in bulk melt debris and to the degree of shock melting in non-vaporized media. Classically speaking, as cooling time increases, so does crystallinity. Empirical investigations of debris from a number of tests indicate a mix of variable proportions of glass and crystal phases in any given debris field due to non-uniform quenching [15], [21]. The mere presence of crystallinity in U-NEMD is ubiquitous, however. Crystals tend to consist of Na-Ca feldspars, quartz, and K-feldspars. Residual phenocrysts entrained in U-NEMD from host rock rubble are also noted in the crystalline phases [15]. Crystallinity also exhibits a relationship to the refractory or volatile nature of its components. Refractory species seem to be contained strictly in vitreous U-NEMD whereas volatile species are found in both glassy and crystalline samples [15]. Volatile elements tend to reside on exposed surfaces, in glass seams, and within vesicles in glassy debris.

In addition to the major physical characteristics, U-NEMD is sometimes subject to the creation of alteration layers on exposed surfaces and in open vesicles [28], [30]. These chemical alteration layers result from the interaction of U-NEMD with liquefied explosion products resulting from pressure and temperature reduction

over time or from the reintroduction of natural groundwater in shots below the static water table level. In either case, the liquid-solid interface creates an environment several microns in thickness where alkali elements and water form a distinct concentration gradient. External to that layer is a gel zone of Si network dissolution. Most affected elements are incorporated into an alteration phase of clays, zeolites, oxides, and/or hydroxides [21]. Forensically, these alteration layers are of interest due to their dissolution of any surface-deposited volatile species and a general alteration of other radiochemical indicators contained in an altered specimen.

2.2.4 Radioactive Properties

Of high forensic interest is any evidence provided by the radionuclide inventory held within the U-NEMD; hence, radioactivity has been named among its most useful attributes [30]. The total radioactive source term in an underground nuclear detonation is governed by the amount of fissile material present, the fission-to-fusion ratio, and the total device yield [15]. The radiations inherent to U-NEMD are a mixed field. Predominant forms are γ and β^- ; but, small contributions from β^+ , α , and delayed neutrons (in the early time) also exist. Sources of these radiations are outlined in §2.1.2 and include residual fuel and tamper materials, fission products, activation products from the device and surrounding media, radiochemical tracers (in testing environments), and the copious progeny of the aforementioned [13], [15], [21], [29], [30], [33]. Thus, it is useful to understand the distribution of radionuclides in the debris field when considering collection and further analysis.

Several studies report that the vast majority of radioactive species—including greater than 98% of residual actinides and 60-85% of bulk fission products—are contained in U-NEMD [25], [26], [28]. These nuclides are indicative of many telling aspects of the device which created the debris. Fuel type and enrichment,

tamper material composition, fusion-to-fission ratio, yield, efficiency, etc. may be ascertained through radiochemical analyses [20], [29], [30].

Consistent with many physical and chemical traits, radioactivity is heterogeneously distributed through individual aliquots of U-NEMD. Most radionuclides also demonstrate heterogeneity in the bulk U-NEMD. While a wide-area fractionation problem is not of concern in a contained underground nuclear detonation, the process does affect radionuclide distribution throughout the post-detonation chamber and chimney. As discussed in the preceding section, refractory species (i.e., alkaline earth elements, lanthanide elements, actinide elements, Zr, and Tc) are generally found in the puddled debris [13], [15], [21], [29], [30]. Volatile species (i.e., ^3H , alkali metals, noble gasses, Ru, Sb, and Te) are generally dispersed throughout the chimney region and upon the surface of U-NEMD while the bulk melt is depleted of those species [13], [21], [30]. Johnson's study of early underground detonations reports U-NEMD depleted in refractory radionuclides with gaseous precursors by as much as two orders of magnitude [26].

Fractionation of refractory nuclides is also reported to occur as a function of crystallinity and as a function of depth within the pooled debris. While both crystalline and vitreous debris demonstrate radioactivity, refractory elements are not generally found in crystalline debris [15]. Borg's study of the Flintlock Pile Driver shot records U-NEMD found higher in the puddle and chimney as enriched in volatile species and consequently depleted in refractory species [25]. Specifically, ^{137}Cs is only 20% contained in the glass. Its gaseous parent, ^{137}Xe , has a 3.818-min half-life which allows it to diffuse for a considerable amount of time before deposition. Conversely, ^{90}Sr and ^{106}Ru , were 40-80% contained in U-NEMD. The half-life of ^{90}Kr , the gaseous antecedent of ^{90}Sr , is only 32.32 seconds, and ^{106}Ru ancestors are all solid at ambient temperature and pressure. Cerium-144 was found to be uniformly distributed vertically through the puddle glass, and was used as a benchmark for comparison in the Pile Driver study.

A number of studies demonstrate spatial correlation of radionuclides by autoradiography [18], [20], [21], [28]. All report that higher α -emitting radionuclide densities correspond to darker glasses within any given sample. Interestingly, α track density is generally homogeneous within the dark glass but is implicitly heterogeneous throughout a multi-colored sample as a function of color. In a study by Eaton and Smith, Pu distribution in dark glass was generally uniform, but isotopic distribution was found to be heterogeneous [28]. It is unclear whether the dark color is evidence of radiolytic damage or of chemical composition. Actinide α activity shows no correlation to specific textural features (e.g., vesicles) [28]. Fahey, et al, found a correlation between areas of high Pu- α activity and areas of high Ca concentrations through comparison of autoradiographs with secondary ion mass spectrometry (SI-MS), x-ray fluorescence (XRF), and back-scatter electron (BSE) microscopy images of Trinitite. In the same study, U and Th were also found heterogeneously dispersed in the matrix but without correlation with any other major element concentration [20]. Similarly, a study by Bonamici, et al, found no correlation between α or β activity and major elemental composition in aerodynamic Trinitite debris [18].

2.2.5 Surrogate Nuclear Explosive Melt Debris

Numerous attempts over the last several years to create realistic surrogate NEMD appear in the literature. A number of the studies focus on replicating various aspects of Trinitite (i.e., morphologically, chemically, radioactively), perhaps the most ubiquitous nuclear debris as it is the only specimen available on the open market [30], [31], [33], [34]. Chemical compositional planning toward the creation of urban debris surrogates which represent that expected from a nuclear attack on a modern city has been reported [22]. Others have pursued generic nuclear explosive debris which attempts to radiochemically replicate aerodynamic fallout debris [35].

Among these studies production and activation methods vary and include furnace heating (Molgaard, et al; Carney, et al), high-flux neutron irradiation (Cook, et al; Carney, et al), CO₂ LASER heating (Lieziers, et al). All focus on surface-deposited or aerodynamic fallout debris surrogates. None, to date, have investigated the production of underground surrogate nuclear melt glass. While Molgaard contends that this is perhaps the most fundamental surrogate debris type to pursue, he notes that it is also useful as a benchmarking procedure [30]. This gap is one which the present work contends to bridge. Beyond benchmarking the debris production process, this work begins to explore prolonged cooling which replicates an underground detonation; and, it sets the stage for investigations into the combined urban-underground surrogate debris development.

CHAPTER THREE

SIMULATION AND CALCULATION METHODS

One goal of this effort is to lay the groundwork for creation of a useful U-NEMD surrogate. This surrogate is ideally engineered to be chemically, morphologically, and ultimately, radioactively analogous to actual U-NEMD from the NNS in the case of this study. In subsequent work, the idea is to produce an urban variant analogous to debris created from an IND detonation in deep urban infrastructure. The following sections outline the methods undertaken to calculate the chemical and physical process parameters necessary to create such a material, hereafter known as Nuclear UnderGround Engineered Test Surrogates (NUGETS).

3.1 Conditions and Assumptions

A number of initial modeling conditions and assumptions pertaining to the several models conducted in this work are addressed in this section. While many of these conditions would be unknown variables in an actual, malicious detonation scenario, they are required in order to produce NUGETS with a reasonable degree of accuracy.

3.1.1 Notional Improvised Nuclear Device Characteristics

The detonation scenarios and chemical recipes presented in the following chapters are based on two notional INDs with the characteristics shown in Table 3.1 and Table 3.2. Actual weapon designs and components should not and will not be discussed here. However, the use of various types and enrichments of fissile material as fuel and the presence of a tamper mass in nuclear weapons is common knowledge [10]. The notional devices presented here are assumed to achieve the same yield (20-kt) using 1 SQ of weapon-grade (WG) U or Pu as the fissile fuel material, and both employ 100 kg of natural U as a tamper [8], [36]. Nuclear yield

Table 3.1 – WGPu IND characteristics.

Device Type	Fission
Fuel	WGPu
Mass	8.000 kg
Enrichment	93 w/o ²³⁹ Pu 7 w/o ²⁴⁰ Pu
Tamper	U
Mass	100.0 kg
Enrichment	Natural
Nuclear Efficiency	13.68%
Conventional Explosive	RDX
Mass	2400 kg

Table 3.2 – WGU IND characteristics.

Device Type	Fission
Fuel	WGU
Quantity	25.00 kg
Enrichment	90 w/o ²³⁵ U 10 w/o ²³⁸ U
Tamper	U
Mass	100.0 kg
Enrichment	Natural
Nuclear Efficiency	4.504%
Conventional Explosive	RDX
Mass	2400 kg

efficiency calculations are available in App. I. A 2400-kg quantity of hexahydro-1,3,5-trinitro-1,3,5-triazine (i.e., RDX, CAS RN: 121-82-4) is included as the conventional high explosive component; 150 kg of 2017 Al alloy (cf. Table 3.3) is included as an assumption for device casing and other accompanying components.

Table 3.3 – *Elemental composition of 2017 Al alloy.*

Element	Mass %
Al	94.25
Mg	1.000
Mn	0.7500
Cu	4.000

3.1.2 Model Environment – Geometry

For the calculations and simulations conducted in this work, an environment is assumed wherein the IND is detonated in a specified geology which is geochemically and geophysically analogous to that of Area 20 in Pahute Mesa at the NNSS at a depth-of-burst (DOB) equal to 609.6 m (2,000 ft) below grade. This DOB was chosen based on very early background work while referring to cavity radius estimations given by Glasstone and Dolan (cf. eq. 3.2) [9]. In order to determine the proper post-shot geometry for cooling profile calculations, it is necessary to determine the post-shot cavity dimensions, and the related mass consumed. A general assumption made across studies of this nature is that the cavity which is formed following a contained, underground, nuclear detonation is generally spherical in shape. Therefore, all calculations which follow adhere to this assumption. Six various approaches to performing such a calculation are found in the literature. Each method is discussed below in order of increasing complexity.

Johnson, et al, correlate cavity radius, R_c , to the cube root of the weapon yield, W [kt], based largely on evidence collected during post-shot analysis of the Plumbbob Rainier shot conducted in volcanic tuff at the NNSS [26]. The relationship is given below in eq. 3.1.

$$R_c = 50 \left[\frac{\text{ft}}{\sqrt[3]{\text{kt}}} \right] * \sqrt[3]{W} \approx 15.24 \left[\frac{\text{m}}{\sqrt[3]{\text{kt}}} \right] * \sqrt[3]{W} \quad (3.1)$$

Glasstone and Dolan present a similar simple relationship which predicts R_c as a function of W [kt] based on a given constant corresponding to the “moderately deep” working point geology [9]. For silicate rocks such as the volcanic tuff found at the NNSS, the relationship is as follows in eq. 3.2a. Detonations in carbonate rocks produce cavity radii given in accordance with eq. 3.2b.

$$R_c = 35 \left[\frac{\text{ft}}{\sqrt[3]{\text{kt}}} \right] * \sqrt[3]{W} \approx 10.67 \left[\frac{\text{m}}{\sqrt[3]{\text{kt}}} \right] * \sqrt[3]{W} \quad (3.2a)$$

$$R_c = 25 * \sqrt[3]{W} \approx 7.620 * \sqrt[3]{W} \quad (3.2b)$$

Based on French empirical measurements presented by Smith and Bourcier, another estimation of R_c [m] is made as a function of W [kt] and DOB, d [m] [21]. The estimation is given by eq. 3.3.

$$R_c = 100 \left[\frac{\sqrt[3]{\text{m}^4}}{\sqrt[3]{\text{kt}}} \right] * \sqrt[3]{\frac{W}{d}} \quad (3.3)$$

Based on early U.S. underground nuclear weapon tests, the University of California’s Lawrence Radiation Laboratory (i.e, UCLRL, now Lawrence Livermore National Laboratory) estimated 700 t of soil or rock are vaporized or melted per kt yield, W [14]. From this estimate, using the local geophysical bulk density, a cavity volume and radius estimation may be extrapolated. This method

is likely to prove an underestimate because it inherently neglects the effects of the pressure wave, specifically plastic compression of rock which permanently increases the effective cavity radius. Nonetheless, it is included as a first-order approximation. Given the total mass of altered rock in the cavity, M_c [kg], and the average bulk density of the surrounding geologic media, $\langle\rho_c\rangle$ [kg/m^3], R_c [m] is calculated thusly:

$$\sum M_c = 7 \times 10^5 * W$$

$$V_c = \frac{\sum M_c}{\langle\rho_c\rangle} = \frac{4\pi}{3} R_c^3$$

$$R_c = \sqrt[3]{\frac{2.1 \times 10^6 W}{4\pi \langle\rho_c\rangle}} \quad (3.4)$$

Boardman, et al, present a method based on further analysis of empirical data from thirty-five subsurface detonations conducted between 1957 and c.1963 [37]. In this method, the calculations account for adiabatic expansion of the cavity to the extent that the vapor pressure in the cavity is equal to that of the lithostatic pressure—the pressure exerted on the cavity by the overburden. Equation 3.5 considers d [m]; W [kt]; average bulk density of the surrounding geologic media, ρ [g/cm^3]; and a constant, C [$\text{Mg}^{1/4} \cdot \text{m}^{1/2} \cdot \text{kt}^{-1/3}$], which is empirically derived from the ratio of specific heats of geologic media involved in a number of tests. Boardman gives a range of C for ten events in tuff between 72.6 and 81.9 where the average value is 78.1. For the case of volcanic tuff which is of interest in this work, the cavity radius in m is given by:

$$R_c = \frac{C^3 \sqrt[3]{W}}{\sqrt[4]{\langle\rho_c\rangle} d} = \frac{78.1^3 \sqrt[3]{W}}{\sqrt[4]{\langle\rho_c\rangle} d} \quad (3.5)$$

Finally, Bridgman gives a very similar approach based upon data from *The Constructive Uses of Nuclear Explosives* that incorporates data from at least ten various tests in three media types [7]. From Bridgman's derivation, the cavity radius in welded tuff, where the units remain consistent with Boardman except density which is given in kg/m^3 and the coefficient which is given in $\text{kg}^{1/4} \cdot \text{m}^{1/2} \cdot \text{kt}^{-1/3}$, is calculated as:

$$R_c = \frac{430 \sqrt[3]{W}}{\sqrt[4]{(\rho_c)d}} \quad (3.6)$$

Table 3.4 - *Cavity radius estimates based on various methods.*

Method	Estimated Cavity Radius R_c [m]
Johnson [26]	41.37
Glasstone/Dolan [9]	28.96
Smith/Bourcier [21]	32.01
UCLRL [14]	11.95
Boardman [37]	36.07
Bridgman [7]	35.32
Mean Radius	30.95
less UCLRL	34.75
Median Radius	33.67
<i>Modeling Radius</i>	<i>35.50</i>

The six methods presented were used to estimate a cavity radius based on the specified scenario (cf. Table 3.4). The derived relationship using UCLRL's

consumed mass measurements is, as expected, an obvious outlier. The Boardman and Bridgman values agree within 1 m, and both methods account more thoroughly for a number of variables upon which the final cavity radius depends than do the others. Thus, the studies in this work assume a nominal cavity radius of 35.50 m.

3.1.3 Model Environment – Geophysical & Geochemical

As noted in §2.2.1, the geochemistry of the detonation site in a remote underground detonation is the primary driver of the elemental composition of the resulting U-NEMD. In order to predict the reasonable elemental composition of a debris surrogate, it is then very important to understand the elemental composition of the precursor. In order to do so, a thorough statistical evaluation of the geochemistry, bulk density, and water content of sample sites in Area 20 of the NNSS was conducted based centrally on the data from the U20N borehole and its nearest neighbors.

Early working models of the geochemistry involved in this effort were developed from results of surface geochemical analyses conducted by Rash [38]. However, this preliminary method was judged a poor approximation based on the vertical and lateral displacements from the NNSS—609.6 m and 100 km, respectively (cf. Fig. 3.1).

Subsequently a, more robust model was developed based on data collected by the United States Geological Survey (USGS) during borehole drilling and sampling operations at the NNSS [39]. This compilation of data is collectively referred to as the Petrographic, Geochemical, and Geophysical (PGG) database. The U20N borehole which was the site of the 1976 Anvil Cheshire shot was chosen as a reference datum [40]. The data available from PGG in Area 20, near U20N, along



Fig. 3.1 – Surface sample location RR-31 relative to the U20N borehole site in the NNSS (red outline) [41], [42].

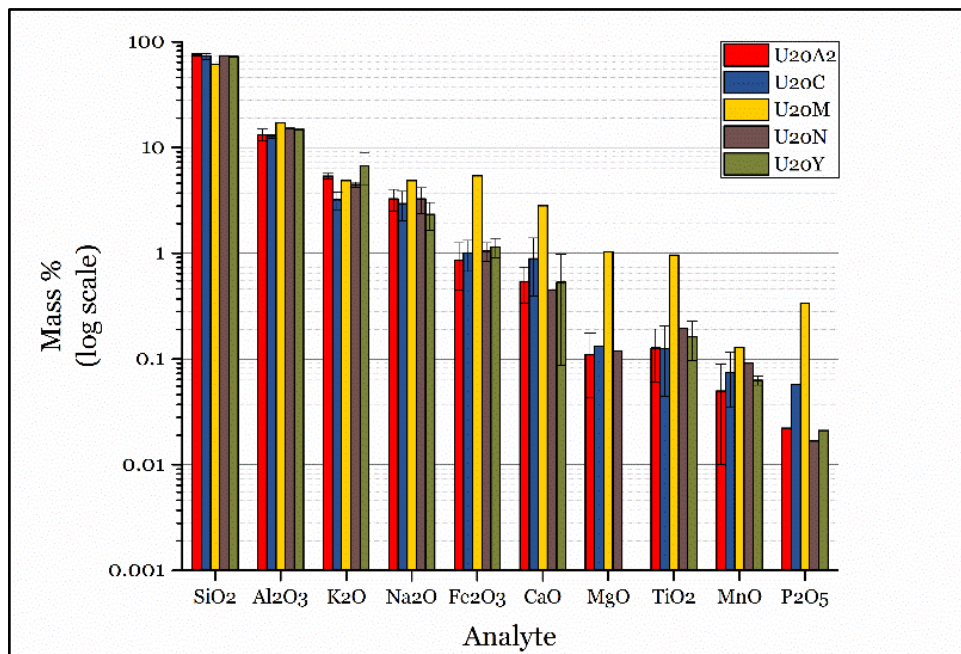


Fig. 3.2 - Analyte concentration of the top ten major compounds found in NNSS geology for five representative locations by mass percent.

with pictorial and descriptive records of the debris produced from the Cheshire shot made this choice clear [17], [39].

Preliminary analysis showed the concentration of many analytes appeared to vary, sometimes drastically, as a function of location (cf. Fig. 3.2). Likewise, bulk density and downhole water content appeared variable with respect to a number of recorded conditions (i.e., location, depth, lithology, and stratigraphy) upon initial inspection. In order to give further credence to the elemental composition, bulk density, and moisture content estimates represented in models used in this work a series of analysis of variance (ANOVA) tests were applied to data from the PGG database.

The ANOVA test establishes the statistical significance of variance in analyte mass fraction, bulk density, and water content with respect to the variables mentioned. The Microsoft® Excel® 2013 (v. 15.0.4903.1002) one-way ANOVA test was used in this study to provide test statistics and p-values based on the following null and alternate hypotheses. For these analyses, the null hypothesis (H_0) is considered true if $p > 0.15$. Results of the ANOVA tests on a case-by-case basis are given in App. II.

For precursor geochemical weight fraction:

$$H_{0,w/0}: \mu_{i,loc-n} = \mu_{i,loc-n+1} = \dots \mu_{i,loc-n+6}$$

$$H_{A,w/0}: \text{At least one } \mu_i \text{ is different.}$$

For precursor geophysical bulk density:

$$H_{0,\rho,1}: \mu_{i,above Rc} = \mu_{i,in Rc} = \mu_{i,below Rc}$$

$$H_{A,\rho,1}: \text{At least one } \mu_i \text{ is different.}$$

$$H_{0,\rho,2}: \mu_{i,loc-n} = \mu_{i,loc-n+1} = \dots = \mu_{i,loc-n+10}$$

$H_{A,\rho,2}$: At least one μ_i is different.

$$H_{0,\rho,3}: \mu_{i,lith-n} = \mu_{i,lith-n+1} = \dots = \mu_{i,lith-n+10}$$

$H_{A,\rho,3}$: At least one μ_i is different.

$$H_{0,\rho,4}: \mu_{i,strat-n} = \mu_{i,strat-n+1} = \dots = \mu_{i,strat-n+27}$$

$H_{A,\rho,4}$: At least one μ_i is different.

For precursor water content weight fraction:

$$H_{0,H_2O,1}: \mu_{i,above Rc} = \mu_{i,in Rc} = \mu_{i,below Rc}$$

$H_{A,H_2O,1}$: At least one μ_i is different.

$$H_{0,H_2O,2}: \mu_{i,loc-n} = \mu_{i,loc-n+1} = \dots = \mu_{i,loc-n+7}$$

$H_{A,H_2O,2}$: At least one μ_i is different.

$$H_{0,H_2O,3}: \mu_{i,lith-n} = \mu_{i,lith-n+1} = \dots = \mu_{i,lith-n+10}$$

$H_{A,H_2O,3}$: At least one μ_i is different.

$$H_{0,H_2O,4}: \mu_{i,strat-n} = \mu_{i,strat-n+1} = \dots = \mu_{i,strat-n+27}$$

$H_{A,H_2O,4}$: At least one μ_i is different.

The ANOVA tests employed in this study were ultimately constrained by the data available in Area 20 for the characteristics of interest. The accuracy an ANOVA test lends to predictive capabilities is directly affected by that availability. For instance, many geochemical analytes were available only in single locations or in single aliquots at a given location. Some of these sample sites, shown in Fig. 3.3,

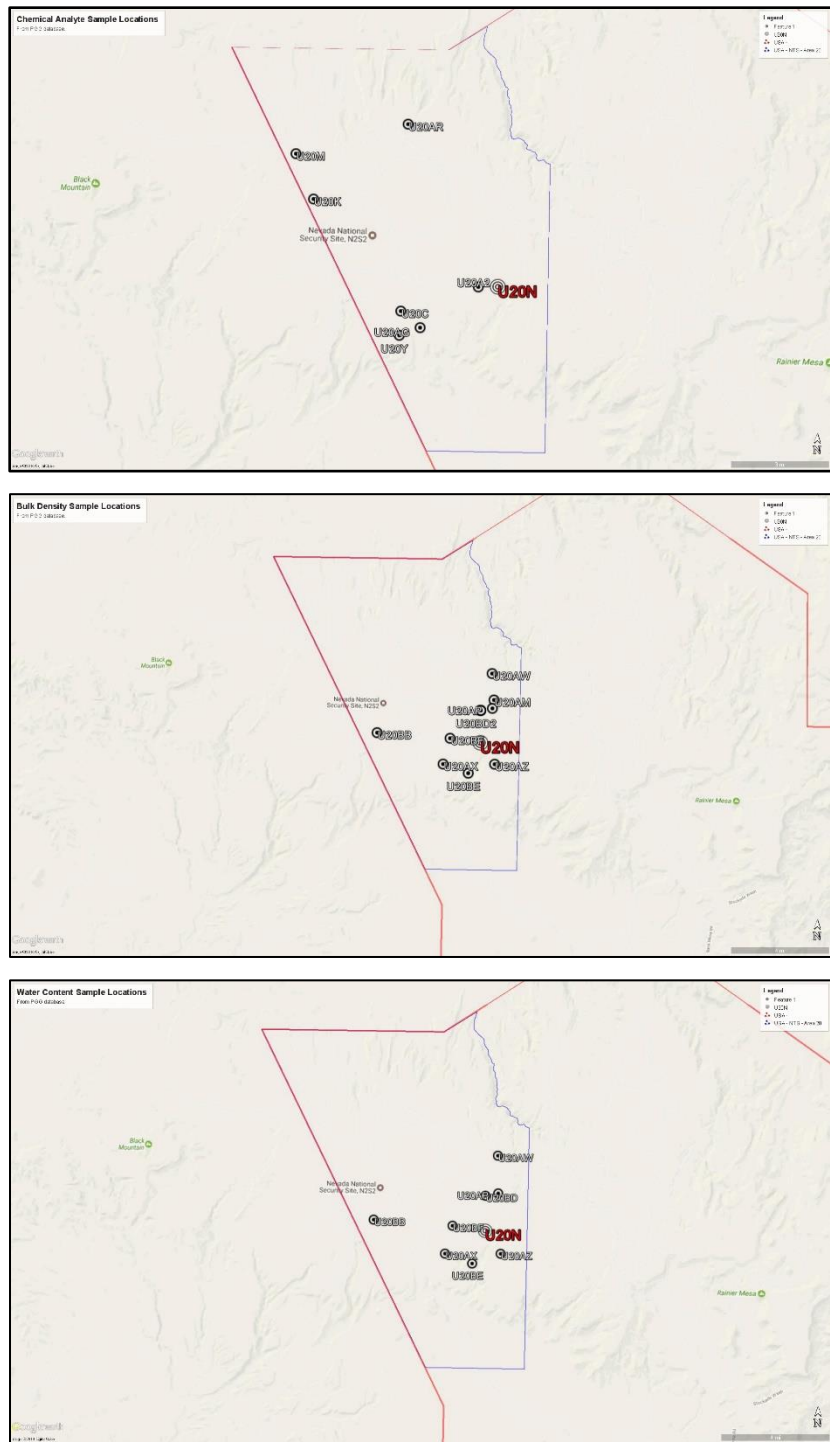


Fig. 3.3 – Geochemical analyte (t), bulk density (m), and water content (b) sample locations relative to U20N within Area 20 of the NNSS [41], [42].

were quite distant from U₂₀N, the site of interest. Bulk density and water content sample sites were generally available closer to the site of interest.

3.2 Fission and Activation Product Models

Beyond geochemical contributions, fission and activation products created during the IND detonation must also be considered when determining the proper chemical composition of a NUGETS matrix. The ORIGEN Fallout Analysis Tool (FAT) was employed to estimate the resulting inventory of fission and activation products which should be present in a NUGETS sample for the chosen geology and IND type specified.

3.2.1 Neutron Transport Model in Geologic Medium

In an attempt to ensure proper estimations of neutron activation products, a preliminary Monte Carlo for n-Particles 6 (MCNP6) test case was employed. The model was composed of series of nested, concentric spheres composed of the geologic precursor media (cf. §4.1 for composition) at a temperature of 600 K (the maximum, as limited by MCNP6). The innermost sphere served as an outward-facing surface neutron source which produces a ²³⁵U(fn,f) Watt spectrum.

Iterative, energy-dependent, surface flux (F2) tallies were taken on the outermost surface of each sphere to permit observation of total flux attenuation and spectral shifts. Energy bins were specified according to the 200-group SCALE 6 neutron library. A cosine tally was employed to limit results to those neutrons leaving an inner sphere and entering the next outer sphere. Weight window generation and weight window mesh tallies were employed as variance reduction measures. To determine the success of models employed, a precision cutoff (i.e., STOP) card was used which instructed the model to cease generation of neutrons once the most distant tally converged to $\leq 0.5\%$ relative error. Additionally, all ten

standard statistical checks performed by MCNP6 were validated. In the case that both the relative error value was met and the model passed all ten statistical checks, it was considered successful.

Due to the immense size of the cavity and the great mass involved, the largest successful MCNP6 simulation involved a 2.00-m radius mass of geologic media with an internal void about the origin of radius 50.0 cm. The internal void served as the outwardly focused source. Thus, the effective transport distance considered is 1.50 m.

A full-size, monolithic model of the post-detonation cavity was attempted but failed to reach an acceptable level of relative error within the available time for computational modeling in this work. The results of the 1.50-m MCNP6 simulation are presented in §4.2. The corresponding input deck is available in App. III.

3.2.2 Fallout Analysis Tool Simulations

The following step in developing a representative surrogate composition of U-NEMD is to calculate the fission and activation product concentrations resulting from each type of detonation. To accomplish this, two ORIGEN FAT simulations were conducted—one for each type of IND proposed. Both models employed the ORIGEN fast neutron spectrum option. The 200-group SCALE 6 neutron spectrum and the 47-group SCALE 6 photon spectrum were chosen. The detonation ran for 100.0 shakes in ten steps. Decay times were specified at 1 s, 1 min, 1 h, 1 d, 1 wk, 1 mo, and 1 yr. These times were chosen to demonstrate nuclide inventories at time steps considered reasonable for field collection and analysis in an actual post-detonation environment. Ten decay steps were generated for each decade of seconds up to the maximum specified time (i.e., 1 yr or 3.156×10^7 s).

The FAT essentially models a point reactor burning the specified type and enrichment of U and/or Pu fuel at a very high power level scaled to the specified weapon yield for a very short duration of time chosen by the user. Structural materials (i.e., weapon components and environmental constituents) may also be added for activation product calculations. The structural materials are treated homogeneously by the FAT application. While it is likely that stratigraphy and lithology of the working point will cause some localized heterogeneity in the chemical composition of the U-NEMD, stratified geochemical data was not readily ascertained from the PGG. Moreover, the major element composition of U-NEMD is certainly more greatly affected by the refractory or volatile nature of individual elements than by stratigraphy.

Based on the UCLRL estimates of 700 t/kt, a mass of 1.4×10^{10} g of geologic media is assumed to be vaporized or melted in this scenario. Both FAT cases conducted in this study employed the full mass of geochemical precursor in the relative abundances determined by the ANOVA analysis and only differ in the type of primary fuel (cf. Table 3.1 and Table 3.2). Since neutron flux is attenuated to 0.1% of the original in the first 1.50 m, it is understood that this simulation should be taken as an approximation. It is likely that some activation product inventories will be overestimated in this process.

Results of the FAT simulations are provided in §4.3 and App. V.

3.3 Underground Debris Cooling Profile

In Olsen's 1967 study, he derived an expression for underground cavity temperature and pressure as a function of time based upon Newtonian cooling principles [14]. In order to create realistic NUGETS samples which are visually, texturally, and morphologically similar to U-NEMD found in the literature, the constraints of the system modeled in this study were applied to Olsen's cooling

formula. While visual and textural similarity are not necessarily forensically important, the prolonged cooling of surrogates should permit the creation chemical compounds and crystal lattices which are found in genuine U-NEMD. These traits are known to affect debris solubility, a factor upon which two forensically significant processes—destructive analyses and environmental transport—rely [21].

Olsen adheres to the UCLRL estimate that 700 t of rock is consumed per kt of weapon yield and further ratios the resulting mass value to the amount of water (i.e., steam) present in the cavity. The first attempt in applying this method to the system under study at present relied upon relating the nominal cavity radius of 35.50 m to the total mass consumed by a volume-density conversion which neglects the appreciable plastic deformation of cavity walls by the pressure impulse of detonation (cf. also eq. 3.4). Neglecting that effect permits a gross overestimate of consumed mass—and, consequently, water content—and should be avoided. Calculations using the UCLRL estimates, achieve a more reasonable answer.

The first step in deriving a cooling expression for the post-detonation cavity is to calculate T_0 [K] which is an expression of the initial cavity temperature immediately following detonation. This initial temperature value is found by applying boundary constraints to eq. 3.7:

$$T_0 = \frac{P_0 V}{nR} \quad (3.7)$$

where

P_0 [atm] is the internal cavity pressure at time, $t_0=t=0$;

V [l] is the volume of the cavity;

n [mol] is the amount of water in the cavity; and,

R is the molar gas constant, $0.0821 \text{ atm}\cdot\text{l}/\text{mol}\cdot\text{K}$.

As seen from the ANOVA results (cf. §4.1, App. II.3), the H₂O mass fraction in the geologic precursor is approximately 17%. The amount of water in moles is found using the following relationship:

$$n_{H_2O} = \frac{7 \times 10^8 \gamma_{H_2O} W}{m_{M,H_2O}} \quad (3.8)$$

where

γ_{H_2O} is the water mass fraction,
 W is the weapon yield, and
 m_{M,H_2O} is the molar mass of water.

Based on the specified nominal cavity radius, the cavity volume is 1.1874×10^8 l. The initial pressure is taken equal to the lithostatic overburden pressure, P_0 , which may be estimated by eq. 3.9:

$$P_0 = \rho g d \quad (3.9)$$

where

ρ [kg/m³] is the geophysical bulk density,
 $g=9.807$ m/s² is the gravitational constant, and
 d [m] is DOB.

By application, T_0 is found as shown in eq. 3.7a:

$$T_0 = \frac{115.5 \text{ atm} * 1.874 \times 10^8 \text{ l}}{1.321 \times 10^8 \text{ mol} * 0.0821 \frac{\text{l-atm}}{\text{mol-K}}} = 1997 \text{ K} \quad (3.7a)$$

Next, the exponential cooling function must be defined by application of constraints to the Newtonian cooling equation (eq. 3.10).

$$\frac{T-T_{\infty}}{T_0-T_{\infty}} = e^{-\left(\frac{hA}{c_v n}\right)t} \quad (3.10)$$

where

t [s] is time,

T [K] is temperature at t ,

T_0 [K] is temperature at $t=0$,

$T_{\infty} = 300$ K is the ambient temperature,

$h = 0.004$ cal/cm²-s-K is the surface heat transfer coefficient,

$A = 1.584 \times 10^8$ cm² is the surface area of the cavity,

$c_v = 6.5$ cal/mol-K is the constant-volume molar heat capacity, and

$n = 1.321 \times 10^8$ mol is the amount of water in the cavity.

Values from Olsen's paper were applied to this study for T_{∞} , h , and c_v . While Olsen notes that values for h are not well-defined in the given scenario, no more-pertinent data was available at the time of this study. After application of values to eq. 3.10, the time-temperature cooling function is found as shown in eqs. 3.10a and 3.10b where time is in seconds and minutes, respectively.

$$T(t) = 1697e^{-7.379 \times 10^{-4}t} + 300 \quad (3.10a)$$

$$T(t) = 1697e^{-0.0443t} + 300 \quad (3.10b)$$

CHAPTER FOUR
STATISTICAL CALCULATION AND COMPUTER
MODELING RESULTS

4.1 Geochemical Precursor Composition

As noted in §3.1.3, the initial surrogate matrices developed in this effort were based on a surface geochemical analysis from northern Nye County, Nevada [38]. The matrices consist of an arithmetic average of two survey points, RR-23 and RR-24. Version 1 (v. 1) solely represents the geochemical precursor matrix, while v. 2 also includes estimated amounts of major fission products and residual U fuel from a nominal device not necessarily represented by Table 3.1 or Table 3.2. For reasons of completeness and continuity, these two chemical oxide recipes are included in App. IV.

The ANOVA results (cf. App. II) show that geochemical concentration is dependent upon location for 23 of the 39 analytes considered. Also, statistical dependence was demonstrated for each variable (i.e., depth, location, lithology, and stratigraphy) with regard to both bulk density and water content.

As pertaining to the geochemical precursor, modeled values were ascertained based on normalized average values for the 16 analytes which demonstrated no statistical dependence on location. For the remaining 23 which were statistically dependent on location, the average value of the analyte recorded in the U20N borehole was used. Model values for water content and density were found by inspection of data from the nearest neighbor (i.e., U20Z) at the appropriate depth. No such data for U20N was available in the version of the PGG database consulted.

The arithmetic mean density value for Area 20 boreholes at the depth of interest is 1.957 g/cm^3 . This value was calculated in initial working models before ANOVA

tests were applied to bulk density data. Following the ANOVA tests, that value was found to agree well with statistical averages and was retained for use in cavity radius calculations and MCNP models. Water mass fraction was determined to be 0.17 based on the ANOVA test results which considered both location and depth. When compared with average values of the lithologies and strata involved, 0.17 agrees well and is well within the statistical variance. The resulting precursor model geochemistry, including 0.17 water mass fraction, is shown by elemental mass percent in Table 4.1.

Table 4.1 - *Elemental composition of hydrous geochemical model precursor by mass percent.*

Element	Mass %	Element	Mass %	Element	Mass %
O	56.07	Zr	1.691×10^{-4}	U	3.852×10^{-6}
Si	29.35	Ce	1.486×10^{-4}	Yb	2.195×10^{-6}
Al	6.379	Rb	1.413×10^{-4}	Sc	1.852×10^{-6}
K	3.135	La	7.061×10^{-5}	As	1.700×10^{-6}
Na	2.055	Zn	4.729×10^{-5}	W	1.353×10^{-6}
H	1.902	Sr	4.618×10^{-5}	Mo	1.269×10^{-6}
Fe	0.6176	Y	2.640×10^{-5}	Ta	1.210×10^{-6}
Ca	0.2710	Nd	2.157×10^{-5}	Tb	5.370×10^{-7}
Ti	9.826×10^{-2}	Nb	2.080×10^{-5}	Sb	4.526×10^{-7}
Mg	6.050×10^{-2}	Th	2.009×10^{-5}	Lu	3.299×10^{-7}
Mn	5.765×10^{-2}	Hf	4.441×10^{-6}	Co	2.960×10^{-7}
P	6.198×10^{-3}	Cs	4.229×10^{-6}	Eu	2.397×10^{-7}
Ba	1.954×10^{-4}	Sm	4.103×10^{-6}	Au	4.060×10^{-9}

Elemental concentrations are very useful as input parameters for neutron transport models as well as fission and activation product generation and depletion

codes (e.g., MCNP, ORIGEN (FAT), et al). Such data is also pertinent for comparison with results of quantitative elemental analysis techniques (e.g., XRF, SI-MS, SEM-EDX, EMPA).

Conversely, elemental compositions are not directly useful for the production of surrogate debris in a laboratory setting. In order to present the geochemical precursor in a more useful form, the elemental weight percentages were stoichiometrically converted to common metal oxide and hydroxide forms. Hydrogen and oxygen are abundant in both the underground cavity and laboratory environments. Thus, a mass balance of these two elements is not necessarily conserved in matrix formulation. Neglecting H and O, the top ten contributing elements are reported in Table 4.2. Beyond the tenth major contributor, masses involved in creating a 10-g lot of matrix become small enough that fidelity of measurement is sacrificed by the resolution of a standard laboratory balance. The minor trace elements should not, however, be disregarded in their forensic utility.

Table 4.2 – NNSS Area 20 geochemical precursor NUGETS matrix.

Compound	Mass %
SiO ₂	75.64
Al ₂ O ₃	14.52
K ₂ O	4.551
NaOH	3.337
Fe ₂ O ₃	1.064
CaO	0.4569
TiO ₂	0.1975
MgO	0.1209
MnO	0.0897
P ₂ O ₅	0.0171

It is of note, that $\text{Ca}_3(\text{PO}_4)_2$ is usually substituted for P_2O_5 in NUGETS production due to the highly reactive nature of the latter. For the same reason, KOH is typically substituted for K_2O . In executing such substitutions, stoichiometric conversions and subsequent normalization must be applied to conserve the elemental mass balance. The oxide forms are presented here for simplicity.

4.2 MCNP Neutron Transport Model Results

The MCNP6 simulations performed yielded only nominally useful results. Because of the large problem undertaken to model, only a small portion was completed successfully. As expected, thermalization and attenuation of the Watt fast fission neutron spectrum is noted, along with a number of interesting scatter and capture artifacts.

An overall attenuation of 1.165×10^{-3} is found over the 1.50 m thickness considered with a relative error of $<0.5\%$. At this range, given approximately 10^{24} free neutrons remaining at the end of detonation, a population on the order of 10^{21} would still remain at 1.50 m. Thus, it is evident a much larger model is appropriate in order to properly scale neutron activation in the underground environment. This model should also include effects of neutron albedo which are not accounted for by this model which employed an outwardly biased cosine tally.

A spectral shift toward thermal energies is immediately evident at and beyond the tally at 30 cm into the geologic media. At 30 cm, the fast and thermal distribution is relatively even, but beyond that point, thermal neutrons begin to dominate the population. Significant scattering and absorbing elements within the media also alter the shape of the spectrum in the first few tens of centimeters. At 30 cm, individual valleys in the flux plot corresponding to energies where high scatter and absorption occur are well-established and remain consistent out to 150

cm. One such feature occurs at 2.814 keV where the total neutron cross-section of ^{23}Na reaches 379.1 barns. Given that Na composes 2.055 wt-% of the geochemistry and that ^{23}Na is the sole naturally occurring Na isotope, it seems reasonable to attribute this phenomenon to ^{23}Na . Fig. 4.1 depicts the six recorded tally series results along with the total neutron cross section of ^{23}Na .

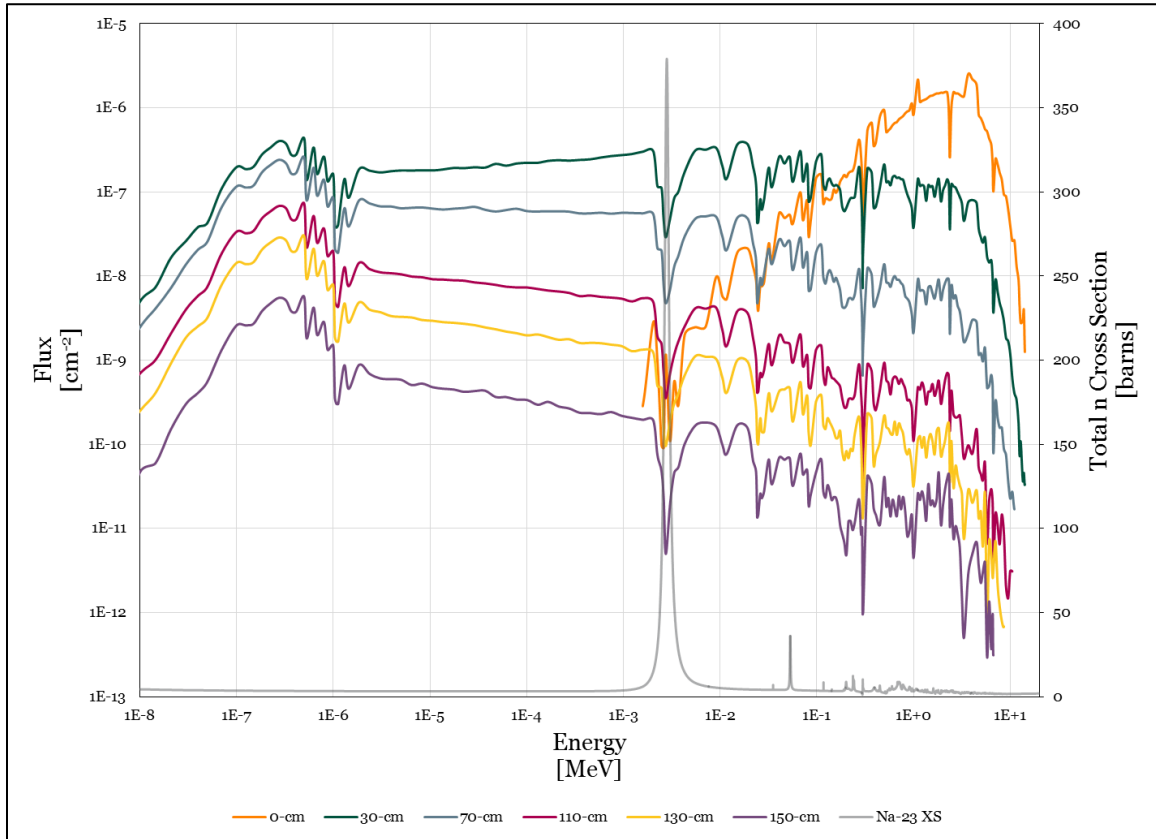


Fig. 4.1 – Cell-averaged neutron flux as a function of energy from the 1.50-m MCNP6 model with the total cross-section of ^{23}Na .

4.3 Fallout Analysis Tool Model Results

Results of both Fallout Analysis Tool models are presented in tabular form in App. V. The data include mass fraction of the debris indexed by both atomic

number (Z) and mass number (A). Seven time steps are included in each table: 0 (precursor composition without IND), 1 s, 1 min, 1 d, 1 wk, 1 mo, and 1 yr. The same results are depicted in Fig. 4.2 and Fig. 4.3.

The rapid ingrowth of fission and activation products is clear in the resulting data. Also evident are regions of isobaric interference with “peak” and “wing” mass numbers caused by the abundance of natural precursor isotopes. This interference is very forensically significant, as a number of major fission product isotopes (e.g., ^{99}Mo , ^{90}Y) are common reference points for determining weapon yield and fuel type. No major elemental composition changes occurred between pre- and post-blast. The largest compositional changes were seemingly artificial injections of ^{13}C (1.208×10^6 g) and Ar (2.128×10^6 g) at 1 s.

No Ar and only 3.887×10^5 g of C are accounted for by the precursor and IND components. Furthermore, no short-lived activation parent nuclides are present in the precursor or IND components in sufficient quantities to support the generation of such appreciable masses. Future investigation into the sensitivity of FAT to generating fission and activation products in large-mass fields is indicated by these discrepancies. A scaled approach may be necessary for applicability of FAT to unconventional uses such as this. Beyond the two anomalous increases of ^{13}C , Ar, and their progeny, IND component materials such as C, N, He, and U are the next most notable additions produced by the detonation.

Based on the data found in App. V, it is determined that the matrix formulation for a typical 10-g batch of NUGETS will change only slightly with respect to major chemical proportion as a result of activation products, fission products, and residual IND component materials. A larger, 100-g or 1-kg matrix would benefit from the addition of residual actinide fuels and major fission products in masses large enough to be accurately measured with standard laboratory equipment.

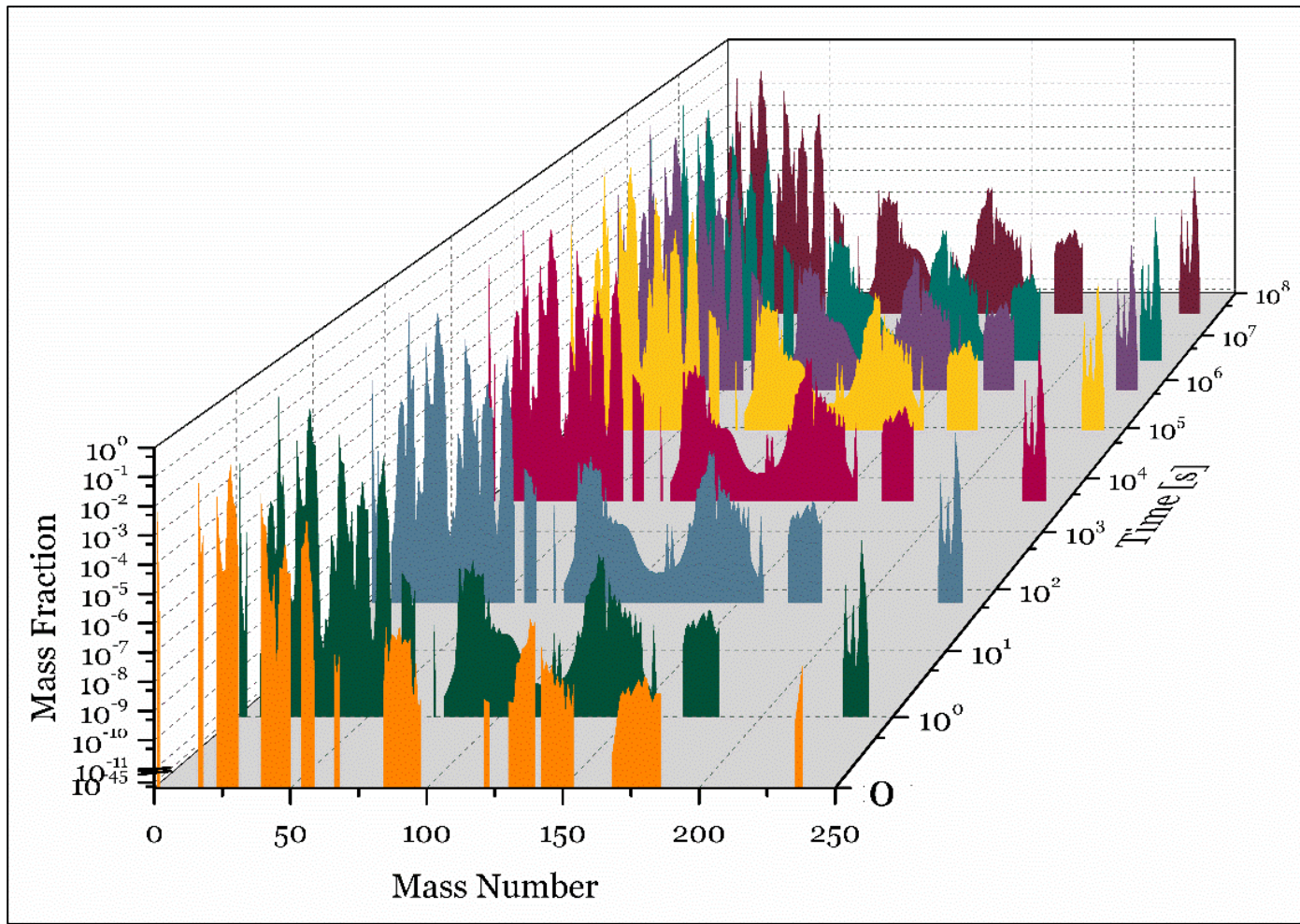


Fig. 4.2 - Isobaric mass fraction vs. time plot of WGPu-fueled IND debris as projected by FAT simulation.

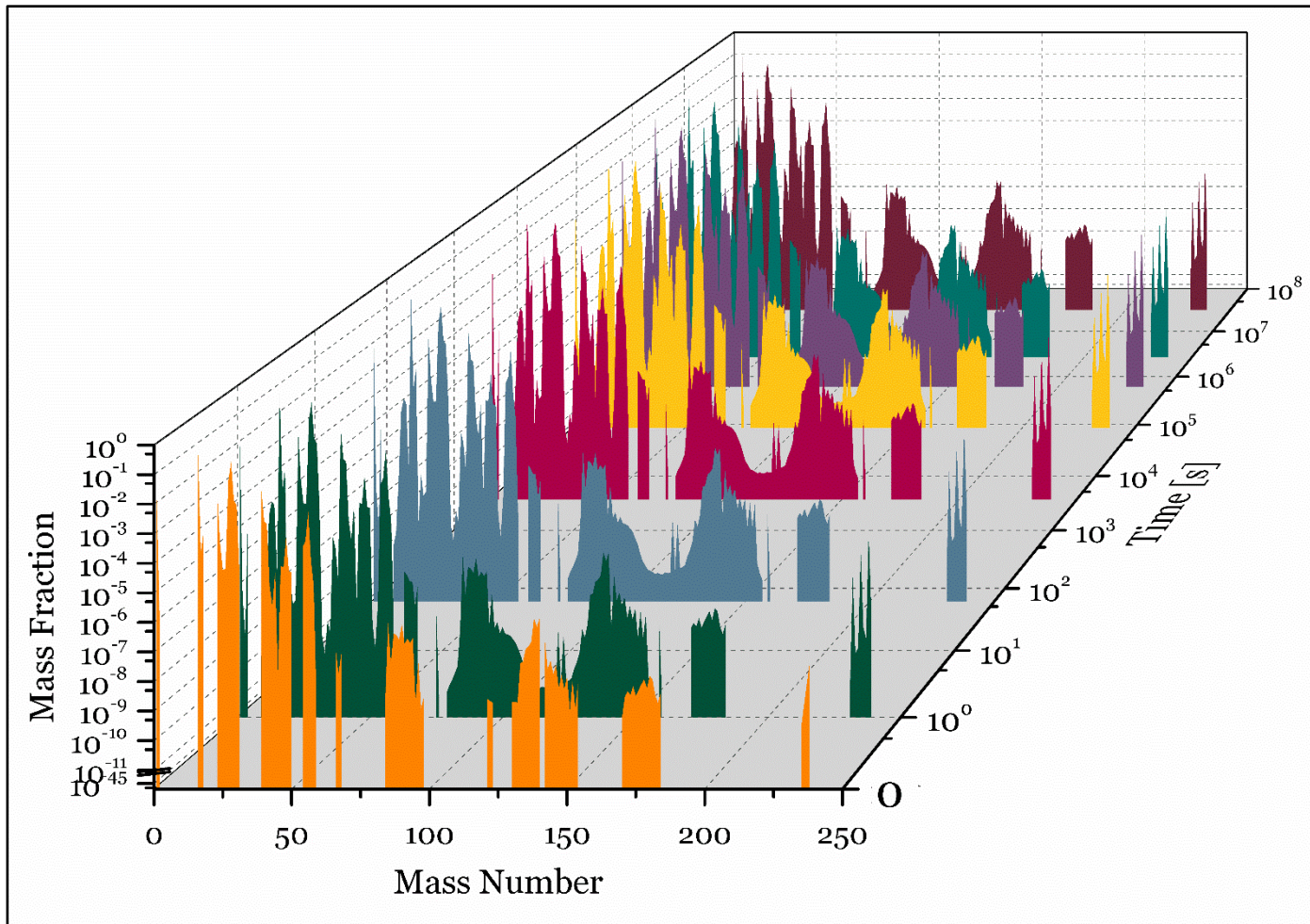


Fig. 4.3 - Isobaric mass fraction vs. time plot of WGU-fueled IND debris as projected by FAT simulation.

4.4 Cooling Function

Fig. 4.4 illustrates the derived Olsen cooling function given by eq. 3.10:

$$T(t) = 1697e^{-0.0443t} + 300 \quad (3.10b)$$

An adapted version of the same cooling curve for laboratory use with the furnace used in production of NUGETS samples is provided in §5.3.1.

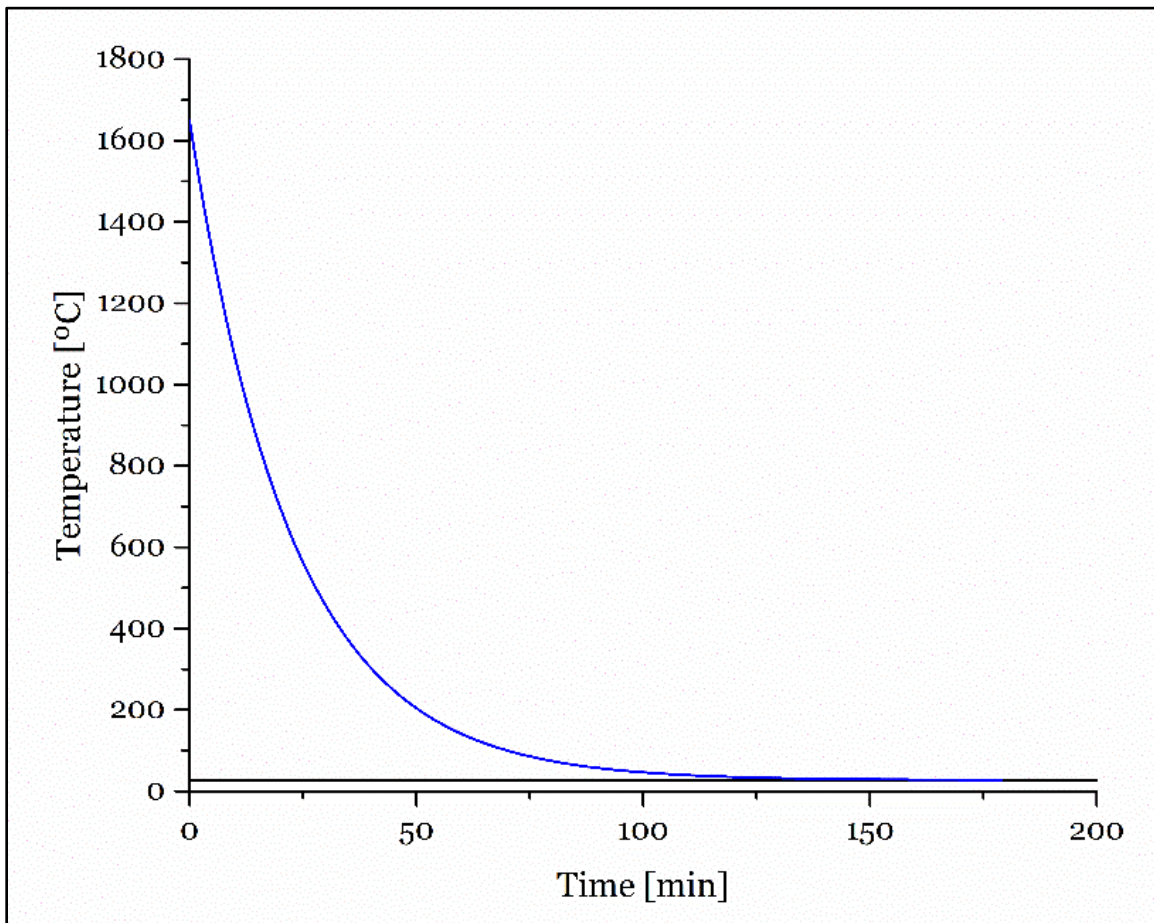


Fig. 4.4 – Time-temperature cavity cooling function. The horizontal line represents ambient temperature ($T_{\infty}=26.85\text{-}^{\circ}\text{C}$).

CHAPTER FIVE

NUGETS EXPERIMENTAL PRODUCTION METHOD

Production of NUGETS is achieved by the firing of a well-mixed chemical oxide/hydroxide powder matrix according to the formulation for a given scenario in an electric furnace. After sufficient time is allowed for the matrix to reach melting point, an automatic, step-wise adaptation of the Olsen cooling function is applied.

5.1 Equipment

5.1.1 Furnace

Production of the samples involved in this study was performed in a CM Furnaces 1700 Series Rapid Temp Lab Furnace (SN: 140884). The furnace is capable of a maximum operating temperature of 1700 °C, and employs electrically driven MoSi₂ heating elements. The control unit is capable of executing a 12-segment heating/cooling profile which is essential to production of underground surrogate debris. Beginning with the first segment, each odd numbered segment (i.e., 1, 3, 5,...,11) executes a temperature increase/decrease (a.k.a., “ramp”) at a specified rate [°C/min]. Each even segment (i.e., 2, 4, 6,...,12) permits “soaking” at the desired temperature set point for a specified amount of time up to 100 h.

5.1.2 Crucibles

Exploration of different crucible types and sizes for surrogate NEMD production has been conducted at the University of Tennessee’s Radiochemistry Center of Excellence (UT-RCOE) [30]. In these investigations, graphite crucibles produced good results. High-purity (2 ppm total impurity content) graphite crucibles sourced from SPEX Sample Prep were used in the firing of NUGETS samples. The crucibles are 32 ml in volume (1.500 in h x 2.000 in r_o) and come

with high-purity graphite lids which were employed in the production of two samples.

5.1.3 Analytical Balances

Two types of analytical balances were used to measure chemicals for creation of the NUGETS matrices. The primary balance used is an Ohaus Explorer Pro model EP64C (SN: N313 1123403626 P). The capacity of the EP64C is 62 g with a resolution of $0.1 \text{ mg} \pm 0.2 \text{ mg}$. With the exception of YCl, this balance was used for measurement of all compounds. Measurement of the YCl was conducted on an A&D model GH-202 dual range analytical balance (SN: 15107939). The GH-202's capacity is 220 g with $0.1 \text{ mg} \pm 0.2 \text{ mg}$ resolution in the standard range; its capacity is 51 g with $0.01\text{-mg} \pm 0.03 \text{ mg}$ resolution in the precision range. Both balances employed draft shields which were closed during all measurements.

Standard disposable low-nitrogen weigh papers or polystyrene weighing boats were used for chemical mass measurement. A new paper or boat was used for each new chemical, and the analytical balance was tared between each measurement in order to ensure the highest degree of precision possible.

5.1.4 Infrared Thermometer

A Fluke model 568 infrared (IR) thermometer (SN: 33920087WS) was used to determine the cooling rate of several samples after removal from the CM furnace. The model 568 measures temperatures from $-40 \text{ }^{\circ}\text{C}$ to $800 \text{ }^{\circ}\text{C}$ with an accuracy of $\pm 1 \%$ or $1 \text{ }^{\circ}\text{C}$, whichever is greater. At a range of 300 mm, the measurement spot size is 19 mm in diameter. Measurements taken in these experiments were made at distances of less than 150 mm.

5.2 Chemical Matrix Preparation

The production of NUGETS samples begins with careful measurement and combination of chemical oxide powders in proper proportions. Each compound is individually weighed and placed in a standard ceramic laboratory mortar. It is preferable to prepare chemicals in pellet form (e.g., NaOH, KOH) by grinding separately in a low-moisture environment before measurement in order to accelerate the measurement of particularly hygroscopic compounds. This proves somewhat problematic in an inherently humid, temperate climate. Following measurement and combination of all compounds, the matrix is vigorously ground and mixed by hand with a ceramic pestle. This process continues until a smooth, uniform texture is felt through the pestle and visual homogeneity is achieved.

After preparation of the nominally homogeneous mixture, individual aliquots—typically of 1 g nominal mass—are weighed and placed in labeled sample vials, or more ideally, directly into a crucible. All samples which will not be fired within a few hours along with any residual matrix are placed in a desiccator for storage.

5.3 Sample Firing Process

5.3.1 Furnace Heating

Prior to the introduction of a sample for firing, the furnace is powered on and allowed to reach the desired operating temperature (1923 K/1650 °C) in manual mode. Once the melting temperature is achieved, the stage of the bottom-loading furnace is lowered and the crucible holding the sample matrix is introduced as quickly as practicable. Generally, a single sample is fired at a time, but in one instance, two lidded crucibles were fired simultaneously in a stacked arrangement. The effects of this arrangement are discussed in §6.1.

Since appreciable heat escapes during the sample loading process, the furnace is allowed to return to the preset temperature. The temperature overshoots the desired set point by up to 25 °C for a short period of time (i.e., ≤10 min) during recovery. The effect of this overshoot is assumed to be minimal given the reasonably short duration. Once the temperature reaches 1650 °C, the sample is soaked for approximately 30 min. This soak is intended to allow the powered sample to reach the liquidus point [30]. Beyond 30 min the furnace is placed in automatic mode and begins execution of the cooling program beginning with the first ramp section. Here, the furnace controller automatically adjusts the temperature per the pre-set ramp rates and temperature set points.

5.3.1 Olsen Cooling Program

The cooling program employed by the furnace controller is derived from eq. 3-10. The curve is translated into inputs for the CM Furnace controller in the form of six ramp segments and six temperature set (soak) points with six corresponding soak durations. In order to keep a continuous cooling profile, all soak times are set to zero. An example of the input parameters required to attain a cooling function based on eq. 3-10 are provided in Table 5.1.

Table 5.1 – Furnace cooling program parameters.

Program Segment	$\frac{\Delta T}{\Delta t}$ [°/min]	Set Point [°C]	Program Segment	$\frac{\Delta T}{\Delta t}$ [°/min]	Set Point [°C]
1	-56.91		7	-12.38	
2		1024	8		238.4
3	-37.37		9	-7.267	
4		612.9	10		151.2
5	-20.55		11	-4.275	
6		386.9	12		99.91

Based on eq. 3-10, a cooling program was developed for NUGETS production. Because the sample is exposed to 1650-°C temperatures for 30 min prior to initiation of the cooling program, there is an equal offset in the graphical data. For ease of comparison, the primary (bottom) horizontal axis represents “Furnace Time,” or the time the sample has physically been in the furnace. The secondary horizontal axis represents “Cavity Time,” or the time following detonation at which a given cavity temperature is expected to occur. The idealized cooling curve is plotted along with the step-wise cooling function based on the production furnace program in Fig. 5.1.

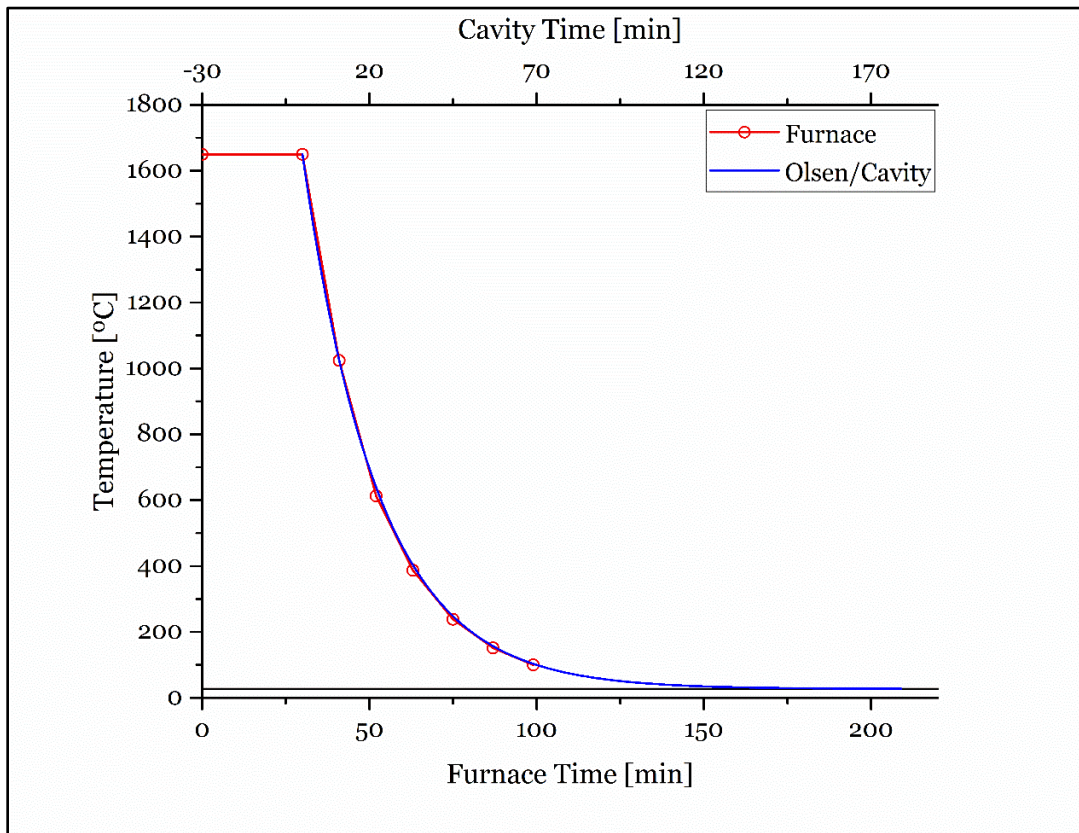


Fig. 5.1 – Idealized cooling curve plot representing cavity cooling (blue) and furnace-controlled cooling (red).

CHAPTER SIX

NUGETS PRODUCTION EXPERIMENTAL RESULTS

A number of NUGETS samples were produced using the preliminary Rash precursor matrix as part of a laboratory exercise involving United States Military Academy cadets in the early stages of this work. Several of the prepared 1-g samples are shown here as examples. Preliminary visual comparisons with genuine U-NEMD and void fraction estimates are also presented.

6.1 Visual Debris Characteristics and Comparison

The first two NUGETS samples (NV1-1A and NV1-1B) were fired below the liquidus point at 1500 °C, for 30 min, and no cooling program was applied to the firing process. The samples were incompletely melted as evidenced by a very gritty, sand-like texture. Both were black in color and displayed no apparent vesicularity. These samples are shown in Fig. 6.1.



Fig. 6.1 – Initial NUGETS production samples NV1-1A (l) and NV1-1B (r).

Two additional samples from the NV1-x series were fired at 1600 °C for 35 min (NV1-1C) and 1570 °C for 30 min (NV1-1D), respectively. The NUGETS produced

were roughly spheroidal in shape with flat bottoms. Both were black in color with some light striations throughout, and exhibited low-to-moderate vesicularity. When fractured, very light specks appeared homogeneously distributed throughout the glassy matrix of both samples. Upon visual inspection, these samples appear very similar to genuine U-NEMD droplets or globules as reported in the literature (cf. Fig. 6.2).

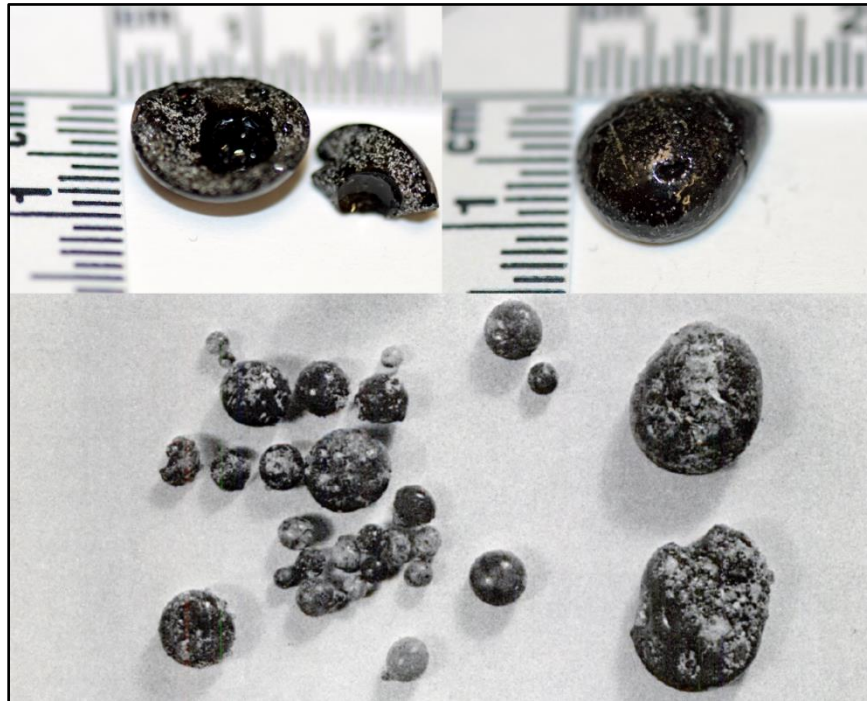


Fig. 6.2 – NUGETS samples NV1-1C (top-l) and NV1-1D (top-r) as compared to beaded U-NEMD recovered from the Plumbbob Rainier cavity (bottom) [27].

Beginning with the second series of samples—designated NV2-x—cooling programs were applied. In some instances the cooling programs were controlled by manual manipulation of the furnace power controller. The later samples were fired under automated control via a preset cooling program such as the one presented in Table 5.1. The NV2-x series of samples were also based on the early

Rash matrix, but these samples included nominal amounts of major fission product elements as outlined in App. IV. All of these samples were fired in excess of 1600-°C for at least 10-minutes before initiation of the cooling function.

The resulting NUGETS beads exhibited distinctly different coloration than the first samples. A predominance of dark gray mottled with various shades of green and white is noted in various samples. Fractured samples exhibited obvious, moderate vesicularity, and a generally heterogeneous distribution of texture and color. During the cooling process, the formation of light specks or bubbles were quite obvious in at least one sample. It is hypothesized that these are the result of outgassing or lattice formation caused by quenching in air at ambient conditions. Each of these samples demonstrated a modest visual resemblance to U-NEMD from the literature (cf. Fig. 6.3).

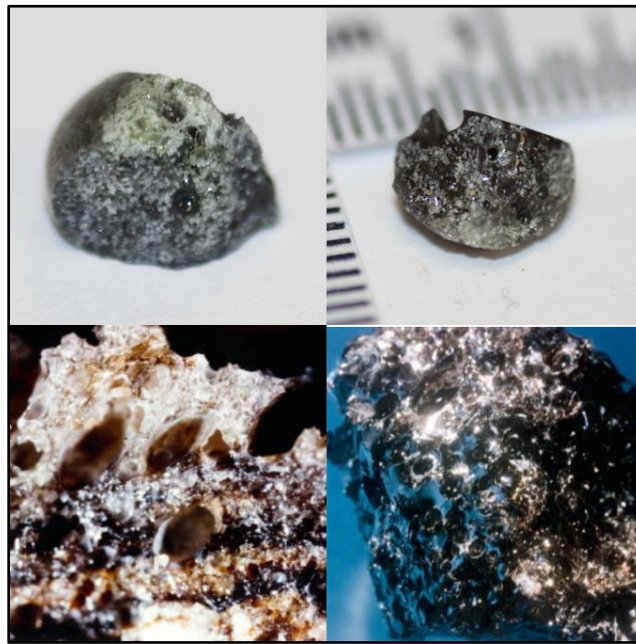


Fig. 6.3 – Two NUGETS NV2 samples (top) as compared to two U-NEMD samples from Niblick Bilby (bottom-l) and Anvil Cheshire (bottom-r) [17].

Fig. 6.4 shows the programmed and actual temperatures used in the production of sample NV2-2.1B. The small concave tail at the end of the actual cooling curve represents ambient cooling after removal from the furnace. The final 18 data points which compose the tail region were recorded with the Fluke IR thermometer at 1- to 2-minute intervals from a range of approximately 6 in.

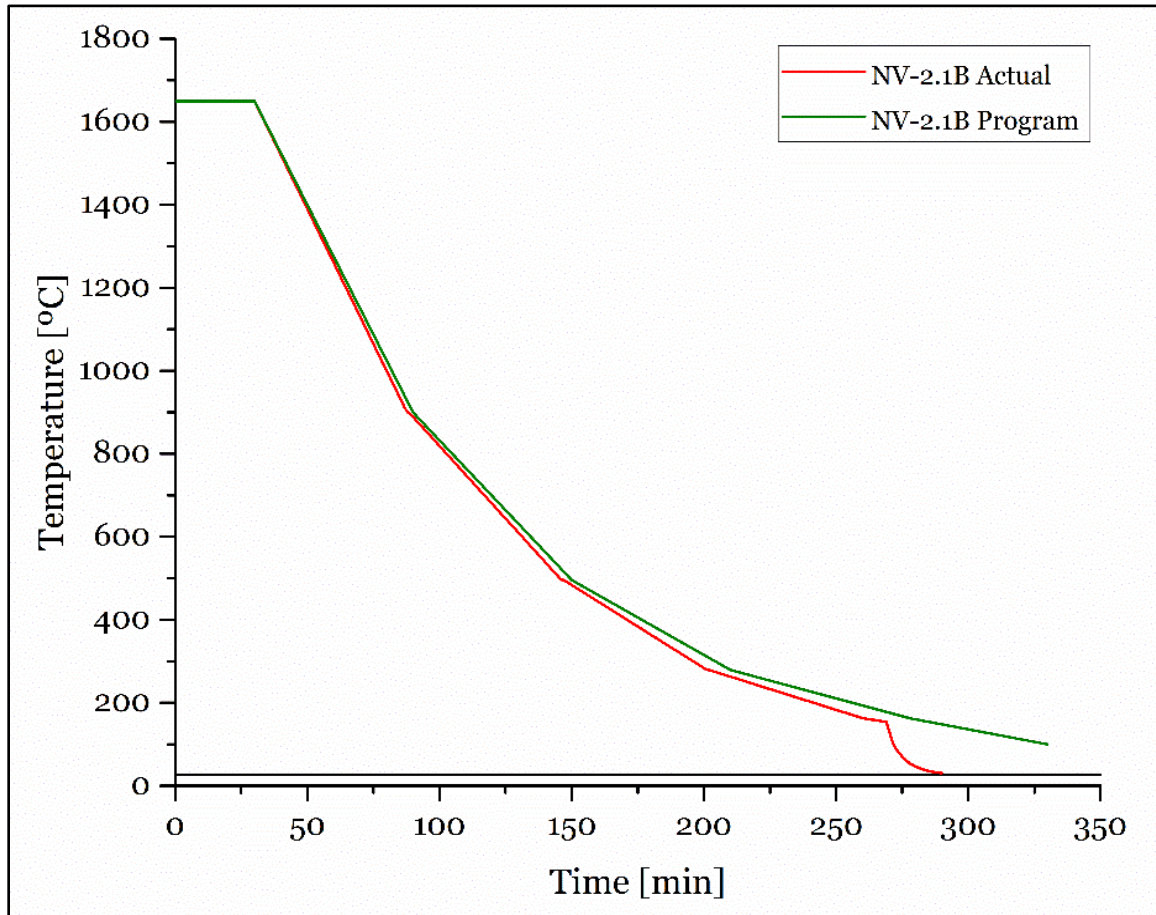


Fig. 6.4 – Experimental cooling profile for sample NV2-2.1B.

An attempt was made to accelerate sample production rate by melting two samples simultaneously with lidded crucibles. The resulting two samples lost surface tension and created a very thin layer of glassy debris on the bottom surface

of the crucible (cf. Fig. 6.5). The glassy matrix was approximately 1 mm thick at its maximum. It seems that a pressure increase due to the lids, or an effective thermal energy increase due to the higher thermal mass of the two-sample system caused a phase change in the matrix during the firing process. While no pictorial comparison was available from the literature, these NUGETS samples seem to represent the glassy coatings which are found on fractured overburden and cavity wall surfaces as described in several accounts [21], [24], [32].



Fig. 6.5 – NV2-series samples prepared simultaneously in sealed, stacked crucibles.

6.2 Void Fraction Estimates

Hydrodensitometry measurements were conducted on six NUGETS samples and one aliquot each of NV1 and NV2 precursor matrices. From these, some rudimentary approximations of density and void fraction were calculated. A void fraction of 30% is reported in the literature concerning Trinitite samples. While statistical significance cannot be attributed to these estimates due to the scant data set, the samples made during the course of this work agree well with the reported value. Of the six samples measured, the calculated average void fraction is 0.3 with a standard deviation of 6×10^{-2} .

CHAPTER SEVEN

CONCLUSIONS AND FUTURE WORK

7.1 Conclusions

The creation of a new type of surrogate nuclear explosive melt debris has been demonstrated for underground detonation scenarios. Preliminary formulation of the debris matrix was based on surface geochemistry near the NNSS. Through a thorough statistical analysis of the geochemistry and geophysical traits germane to U-NEMD production in Area 20 of the NNSS, a more-robust chemical precursor was developed. Fission and activation product inventories for two IND types were generated using the ORIGEN Fallout Analysis Tool. A scenario-specific cooling function was derived from the literature and applied to the creation of non-radioactive 1-g NUGETS samples.

It has been demonstrated that production of NUGETS according to the methods developed in this work results in samples which demonstrate similar color and texture to various U-NEMD specimens recorded in the literature. Beaded debris was produced in open graphite crucibles while samples melted in sealed crucibles yielded thin layers of debris similar to the glassy coatings found on fractured overburden and lining the walls of underground test cavities.

Neither radiochemical nor morphological comparisons to actual U-NEMD were made. However, the highly complex debris production and fractionation process discussed in §2.2 along with the exclusion of any weapons component materials would certainly cause the NUGETS samples to differ chemically from genuine U-NEMD.

7.2 Future Work

Future exploration of this field should pursue inclusion of the proper proportion of U and Pu in NUGETS matrices with subsequent high-flux, fast neutron irradiation campaigns at a facility such as the Department of Defense's (DOD) Fast Burst Reactor at White Sands Missile Range [43]. In this manner, fission and activation products may be produced in situ, thus producing a higher fidelity surrogate debris in support of MC&A and V&V efforts within MIDAS and the TNF community at large. Such an irradiation campaign should be structured to consider neutron albedo effects produced in underground environments if possible.

Predictive modeling for irradiation of NUGETS should be preceded by a sensitivity analysis of FAT for use in this unorthodox manner. If FAT/ORIGEN is not readily adaptable or scalable for underground scenarios, MCNP KCODE burn-up and depletion modeling should be explored.

Detailed physical, radiochemical, and morphological characterization of NUGETS samples along with comparison to genuine U-NEMD at the proper security level should follow. By these analyses, a determination of NUGETS' utility as a holistic U-NEMD surrogate may be ascertained.

Finally, it is imperative that further development of NUGETS augment the methods developed here to include scenarios for vented, low-yield, uncoupled detonations in an urban environment.

REFERENCES

- [1] *The Holy Bible*. King James Version. Nashville, TN: Thomas Nelson, 1988.
- [2] A. Carnsdale *et al.*, “Nuclear Forensics: A Capability at Risk (Abbreviated Version),” The National Academies Press, Washington, D.C., 2010.
- [3] M. May *et al.*, “Nuclear Forensics - Role, State of the Art, Program Needs,” American Association for the Advancement of Science, Washington, D.C., 2008.
- [4] U. S. Congress, *Nuclear Forensics and Attribution Act*. Washington, D.C., United States of America: 111th Congress, 2010, pp. 31–36.
- [5] Preparatory Commission for the Comprehensive Nuclear-Test-Ban Treaty Organization, “CTBTO World Map,” 2016. [Online]. Available: <https://www.ctbto.org/map/#mode=nuclear>. [Accessed: 16-Aug-2016].
- [6] J. Ingraham, “DTRA Nuclear Forensics Materials Collections and Analysis Program.” Defense Threat Reduction Agency, 01-Aug-2016.
- [7] C. J. Bridgman, *Introduction to the Physics of Nuclear Weapons Effects*. Fort Belvoir, VA: Defense Threat Reduction Agency, 2001.
- [8] K. J. Moody *et al.*, *Nuclear Forensic Analysis*, 2nd ed. Boca Raton, FL: CRC Press, 2015.
- [9] S. Glasstone and P. J. Dolan, *The Effects of Nuclear Weapons*, 3rd ed. Washington, D. C., United States of America: U.S. Energy Research and Development Administration, 1977.
- [10] R. Serber, *The Los Alamos Primer*. Berkeley, CA: University of California Press, 1992.
- [11] U.S. Congress Office of Technology Assessment, “The Containment of Underground Nuclear Explosions,” U. S. Government Printing Office, Washington, DC, OTA-ISC-414, Oct. 1989.
- [12] AJ Software & Multimedia, “Nuclear Chain Reactions,” *AtomicArchive.com*, 2015. [Online]. Available: <http://www.atomicarchive.com/Fission/Fission2.shtml>. [Accessed: 02-Feb-2017].
- [13] A. F. B. Tompson *et al.*, “On the evaluation of groundwater contamination

- from underground nuclear tests,” *Environ. Geol.*, vol. 42, no. 2–3, pp. 235–247, Jun. 2002.
- [14] C. W. Olsen, “Time History of the Cavity Pressure and Temperature Following a Nuclear Detonation in Alluvium,” *Journal Geophys. Res.*, vol. 72, no. 20, pp. 5037–5041, Oct. 1967.
- [15] D. K. Smith, “Characterization of Nuclear Explosive Melt Debris,” *Radiochim. Acta*, vol. 69, no. 3, pp. 157–167, Jul. 1995.
- [16] D. K. Smith *et al.*, “Transport of gaseous fission products adjacent to an underground nuclear test cavity,” *Radiochim. Acta*, vol. 73, no. 4, pp. 177–183, Aug. 1996.
- [17] A. B. Kersting and D. K. Smith, “Observations of Nuclear Explosive Melt Glass Textures and Surface Areas,” Lawrence Livermore National Laboratory, Livermore, CA, UCRL-TR-218361, Jan. 2006.
- [18] C. E. Bonamici *et al.*, “A geochemical approach to constraining the formation of glassy fallout debris from nuclear tests,” *Contrib. to Mineral. Petrol.*, vol. 172, no. 2, Jan. 2017.
- [19] J. I. Pacold *et al.*, “Chemical speciation of U, Fe, and Pu in melt glass from nuclear weapons testing,” *J. Appl. Phys.*, vol. 119, no. 19, May 2016.
- [20] A. J. Fahey *et al.*, “Postdetonation nuclear debris for attribution,” *Proc. Natl. Acad. Sci. U. S. A.*, vol. 107, no. 47, pp. 20207–20212, Nov. 2010.
- [21] D. K. Smith and W. L. Bourcier, “The Production and Dissolution of Nuclear Explosive Melt Glasses at Underground Test Sites in the Pacific Region (Preprint),” in *International Symposium on Marine Pollution, IAEA*, 1998.
- [22] A. V. Giminaro *et al.*, “Compositional planning for development of synthetic urban nuclear melt glass,” *J. Radioanal. Nucl. Chem.*, vol. 306, no. 1, pp. 175–181, Mar. 2015.
- [23] C. W. Olsen, “Site Selection and Containment Evaluation for LLNL Nuclear Events (Preprint),” in *7th Symposium on the Containment of Underground Nuclear Explosions*, 1993.
- [24] L. Schwartz *et al.*, “Glass produced by underground nuclear explosions,” *J.*

- Non. Cryst. Solids*, vol. 67, no. 1–3, pp. 559–591, Sep. 1984.
- [25] I. Y. Borg, “Radioactivity trapped in melt produced by a nuclear explosion,” *Nucl. Technol.*, vol. 26, no. 1, pp. 88–100, May 1975.
- [26] G. W. Johnson *et al.*, “Underground Nuclear Detonations,” *J. Geophys. Res.*, vol. 64, no. 10, pp. 1457–1470, Oct. 1959.
- [27] G. C. Kennedy and G. H. Higgins, “Temperatures and pressures associated with the cavity produced by the Rainier event,” University of California Radiation Laboratory, Livermore, CA, UCRL-5281, Jul. 1958.
- [28] G. F. Eaton and D. K. Smith, “Aged nuclear explosive melt glass: Radiography and scanning electron microscope analyses documenting radionuclide distribution and glass alteration,” *J. Radioanal. Nucl. Chem.*, vol. 248, no. 3, pp. 543–547, Jun. 2001.
- [29] “Final Site-Wide Environmental Impact Statement for the Continued Operation of the Department of Energy/National Nuclear Security Administration Nevada National Security Site and Off-Site Locations in the State of Nevada: Volume 2 (Appendices A through I),” Department of Energy, Las Vegas, NV, DOE/EIS-0426, Feb. 2013.
- [30] J. J. Molgaard, “Production of Nuclear Debris Surrogates for Forensic Methods Development,” M.S. thesis, Dept. Nuc. Engr., Univ. Tennessee, Knoxville, TN, 2014.
- [31] J. J. Molgaard *et al.*, “Development of synthetic nuclear melt glass for forensic analysis,” *J. Radioanal. Nucl. Chem.*, vol. 304, no. 3, pp. 1293–1301, Jun. 2015.
- [32] R. E. Wadman and W. D. Richards, “Postshot Geologic Studies of Excavations Below Rainier Ground Zero,” University of California Lawrence Radiation Laboratory, Mercury, NV, United States of America, UCRL-6586, Jul. 1961.
- [33] M. T. Cook *et al.*, “A comparison of gamma spectra from trinitite versus irradiated synthetic nuclear melt glass,” *J. Radioanal. Nucl. Chem.*, vol. 307, no. 1, pp. 259–267, Jan. 2016.

- [34] M. Liezers *et al.*, “The formation of trinitite-like surrogate nuclear explosion debris (SNED) and extreme thermal fractionation of SRM-612 glass induced by high power CW CO₂ laser irradiation,” *J. Radioanal. Nucl. Chem.*, vol. 304, no. 2, pp. 705–715, May 2015.
- [35] K. P. Carney *et al.*, “The development of radioactive glass surrogates for fallout debris,” *J. Radioanal. Nucl. Chem.*, vol. 299, no. 1, pp. 363–372, Jan. 2014.
- [36] International Atomic Energy Agency, *IAEA Safeguards Glossary*, vol. 3. Vienna, Austria: International Atomic Energy Agency, 2002.
- [37] C. R. Boardman *et al.*, “Responses of four rock mediums to contained nuclear explosions,” *J. Geophys. Res.*, vol. 69, no. 16, pp. 3457–3469, Aug. 1964.
- [38] K. B. Rash, “Geology and Geochemistry of Tertiary Volcanic Rocks in the Northern Reveille and Southern Pancake Ranges, Nye County, Nevada,” M.S. thesis, Dept. Geosci., Univ. Nevada, Las Vegas, NV, 1995.
- [39] R. G. Warren *et al.*, “A petrographic, geochemical, and geophysical database, and stratigraphic framework for the southwestern Nevada volcanic field,” Los Alamos National Laboratory, Los Alamos, NM, LA-UR-03-1503, 2004.
- [40] U.S. Department of Energy, “United States Nuclear Tests: July 1945 through September 1992,” Las Vegas, NV, United States of America, DOE/NV--209-REV 15, Dec. 2000.
- [41] “Nevada and NNSS,” *Google Earth Pro*. [Online]. Available: <https://www.google.com/earth/>. [Accessed: 04-Mar-2017].
- [42] W. R. Johnston, “Nuclear Tests--Databases and Other Material,” *Johnston's Archive*, 2016. [Online]. Available: <http://www.johnstonsarchive.net/nuclear/tests/>. [Accessed: 29-Jun-2016].
- [43] White Sands Missile Range, “Survivability Vulnerability.” [Online]. Available: <http://www.wsmr.army.mil/testcenter/org/Pages/SurvivabilityVulnerability.aspx>. [Accessed: 05-Mar-2017].

- [44] M. G. Sowerby, "Nuclear fission," *Kaye & Laby Tables of Physical & Chemical Constants*, 2015. [Online]. Available: http://www.kayelaby.npl.co.uk/atomic_and_nuclear_physics/4_7/4_7_1.html. [Accessed: 13-Jan-2017].

APPENDICES

APPENDIX I: FISSION YIELD CALCULATIONS

Given the parameters in Table 3.1, an average prompt energy liberation per fission of 189.5 MeV, and assuming that all energy liberated in the detonation comes expressly from the fission of ^{239}Pu , the notional IND explosive yield efficiency (ε) is calculated thusly [44]:

20.00 kt	$4.184 \times 10^{12} \text{ J}$	1 MeV	1 fission	1 atom
	1 kt	$1.602 \times 10^{-13} \text{ J}$	189.5 MeV	1 fission

1 mol	$239.052 \text{ g } ^{239}\text{Pu}$	1 kg ^{239}Pu	1 SQ WGPu
$6.022 \times 10^{23} \text{ atoms}$	1 mol ^{239}Pu	1000 g ^{239}Pu	7.440 kg ^{239}Pu

$$\varepsilon = 14.71\%$$

Considering the parameters from Table 3.2, an average prompt energy liberation per fission of 180.9 MeV, and assuming that all energy liberated in the detonation comes expressly from the fission of ^{235}U , the notional IND explosive yield efficiency (ε) is calculated thusly [44]:

20.00 kt	$4.184 \times 10^{12} \text{ J}$	1 MeV	1 fission	1 atom
	1 kt	$1.602 \times 10^{-13} \text{ J}$	180.9 MeV	1 fission

1 mol	$235.043 \text{ g } ^{235}\text{U}$	1 kg ^{235}U	1 SQ WGU
$6.022 \times 10^{23} \text{ atoms}$	1 mol ^{235}U	1000 g ^{235}U	22.50 kg ^{235}U

$$\varepsilon = 5.009\%$$

APPENDIX II: ANOVA TEST RESULTS

AII.1 ANOVA Results for Analyte Weight Fraction by Location, Indexed Alphabetically by Analyte

Al₂O₃

Groups	Count	Sum	Average	Variance
U20A2	5	66.14	13.228	2.92747
U20AR	1	14.03	14.03	#DIV/o!
U20C	2	25.43	12.715	0.26645
U20K	1	12.66	12.66	#DIV/o!
U20M	1	17.1	17.1	#DIV/o!
U20N	1	15.21	15.21	#DIV/o!
U20Y	2	29.58	14.79	0.0098

ANOVA						
Source of Variation	SS	df	MS	F	P-value	F crit
Between Groups	20.13790077	6	3.356316795	1.680100313	0.272116209	4.283865714
Within Groups	11.98613	6	1.997688333			
Total	32.12403077	12				

As₂O₃

Groups	Count	Sum	Average	Variance
U20C	1	0.6602	0.6602	#DIV/o!
U20N	2	9.295	4.6475	18.1262205

ANOVA						
Source of Variation	SS	df	MS	F	P-value	F crit
Between Groups	10.59904086	1	10.59904086	0.584735293	0.584395379	161.4476388
Within Groups	18.1262205	1	18.1262205			
Total	28.72526136	2				

BaO

Groups	Count	Sum	Average	Variance
U20A2	5	827.47	165.494	14388.72118
U20AR	1	361.5	361.5	#DIV/o!
U20C	2	426.5	213.25	19740.845
U20M	1	1542	1542	#DIV/o!
U20N	2	515.9	257.95	123.245
U20Y	2	473.6	236.8	1601.78

ANOVA						
Source of Variation	SS	df	MS	F	P-value	F crit
Between Groups	1658689.72	5	331737.944	29.38678093	0.000147444	3.97152315
Within Groups	79020.75472	7	11288.67925			1
Total	1737710.475	12				

BeO

Groups	Count	Sum	Average	Variance
U20A2	3	36.062	12.02066667	10.26010133
U20C	1	11.1	11.1	#DIV/o!

ANOVA						
Source of Variation	SS	df	MS	F	P-value	F crit
Between Groups	0.635720333	1	0.635720333	0.061960434	0.826652708	18.51282051
Within Groups	20.52020267	2	10.26010133			
Total	21.155923	3				

CaO

Groups	Count	Sum	Average	Variance
U20A2	5	2.6914	0.53828	0.041491672
U20AR	1	1.599	1.599	#DIV/o!
U20C	2	1.7837	0.89185	0.249429845
U20K	1	0.48	0.48	#DIV/o!
U20M	1	2.817	2.817	#DIV/o!
U20N	1	0.4483	0.4483	#DIV/o!
U20Y	2	1.0629	0.53145	0.197506125

ANOVA

Source of Variation	SS	df	MS	F	P-value	F crit
Between Groups	5.418487402	6	0.903081234	8.840698162	0.00895905	4.283865714
Within Groups	0.612902658	6	0.102150443			
Total	6.03139006	12				

Ce₂O₃

Groups	Count	Sum	Average	Variance
U20A2	2	468.5	234.25	27448.245
U20C	1	70.28	70.28	#DIV/o!
U20K	1	442.2	442.2	#DIV/o!
U20N	2	152.24	76.12	1208.3528

ANOVA

Source of Variation	SS	df	MS	F	P-value	F crit
Between Groups	107783.4908	3	35927.83027	2.507473533	0.297873478	19.16429213
Within Groups	28656.5978	2	14328.2989			
Total	136440.0886	5				

CO₂

Groups	Count	Sum	Average	Variance
U20A2	1	0.03	0.03	#DIV/o!
U20AG	8	4.5	0.5625	0.726964286
U20C	1	0.73	0.73	#DIV/o!

ANOVA						
Source of Variation	SS	df	MS	F	P-value	F crit
Between Groups	0.29829	2	0.149145	0.205161385	0.819243874	4.737414128
Within Groups	5.08875	7	0.726964286			
Total	5.38704	9				

CoO

Groups	Count	Sum	Average	Variance
U20C	1	3.814	3.814	#DIV/o!
U20N	2	0.89	0.445	0.063368

ANOVA						
Source of Variation	SS	df	MS	F	P-value	F crit
Between Groups	7.566774	1	7.566774	119.4100177	0.058096743	161.4476388
Within Groups	0.063368	1	0.063368			
Total	7.630142	2				

CS₂O

Groups	Count	Sum	Average	Variance
U20C	1	2.12	2.12	#DIV/o!
U20K	1	5.301	5.301	#DIV/o!
U20N	2	16.961	8.4805	27.5207805

ANOVA						
Source of Variation	SS	df	MS	F	P-value	F crit
Between Groups	27.8122805	2	13.90614025	0.505295998	0.705241768	199.5
Within Groups	27.5207805	1	27.5207805			
Total	55.333061	3				

CuO

Groups	Count	Sum	Average	Variance
U20A2	3	40.063	13.35433333	25.60715633
U20C	1	12.52	12.52	#DIV/o!

ANOVA

Source of Variation	SS	df	MS	F	P-value	F crit
Between Groups	0.522084083	1	0.522084083	0.02038821	0.899544866	18.51282051
Within Groups	51.21431267	2	25.60715633			
Total	51.73639675	3				

Eu₂O₃

Groups	Count	Sum	Average	Variance
U20C	1	0.3474	0.3474	#DIV/o!
U20K	1	0.2432	0.2432	#DIV/o!
U20N	2	0.7874	0.3937	0.05255282

ANOVA

Source of Variation	SS	df	MS	F	P-value	F crit
Between Groups	0.01511138	2	0.00755569	0.143773255	0.881289381	199.5
Within Groups	0.05255282	1	0.05255282			
Total	0.0676642	3				

Fe₂O₃

Groups	Count	Sum	Average	Variance
U20A2	5	4.2781	0.85562	0.162334072
U20AR	1	2.024	2.024	#DIV/o!
U20C	2	1.9951	0.99755	0.107138205
U20K	1	3.59	3.59	#DIV/o!
U20M	1	5.411	5.411	#DIV/o!
U20N	3	3.1317	1.0439	0.04491193
U20Y	2	2.2853	1.14265	0.057358845

ANOVA

Source of Variation	SS	df	MS	F	P-value	F crit
Between Groups	23.3960292	6	3.8993382	34.52050807	2.70077E-05	3.58058032
Within Groups	0.903657198	8	0.11295715			
Total	24.2996864	14				

FeO

Groups	Count	Sum	Average	Variance
U20A2	3	0.92	0.306667	0.128233
U20C	1	0.2322	0.2322	#DIV/o!

ANOVA

Source of Variation	SS	df	MS	F	P-value	F crit
Between Groups	0.004159	1	0.004159	0.032433	0.873677	18.51282
Within Groups	0.256467	2	0.128233			
Total	0.260626	3				

HfO₂

Groups	Count	Sum	Average	Variance
U20C	1	0.2358	0.2358	#DIV/o!
U20K	1	45.16	45.16	#DIV/o!
U20N	2	12.381	6.1905	10.5754005

ANOVA

Source of Variation	SS	df	MS	F	P-value	F crit
Between Groups	1281.586128	2	640.7930638	60.59279398	0.090466962	199.5
Within Groups	10.5754005	1	10.5754005			
Total	1292.161528	3				

K₂O

Groups	Count	Sum	Average	Variance
U20A2	5	26.756	5.3512	0.1056772
U20AR	1	4.245	4.245	#DIV/o!
U20C	2	6.402	3.201	0.3698
U20K	1	4.88	4.88	#DIV/o!
U20M	1	4.855	4.855	#DIV/o!
U20N	3	13.395	4.465	0.062221
U20Y	2	13.354	6.677	4.873442

ANOVA

Source of Variation	SS	df	MS	F	P-value	F crit
Between Groups	14.0957076	6	2.3492846	3.245768888	0.063686377	3.58058032
Within Groups	5.7903928	8	0.7237991			
Total	19.8861004	14				

La₂O₃

Groups	Count	Sum	Average	Variance
U20A2	3	269.72	89.90666667	5683.732933
U20C	1	15.25	15.25	#DIV/o!
U20K	1	243.6	243.6	#DIV/o!
U20N	2	85.61	42.805	248.42205

ANOVA

Source of Variation	SS	df	MS	F	P-value	F crit
Between Groups	33599.53148	3	11199.84383	2.89254956	0.203145169	9.276628153
Within Groups	11615.88792	3	3871.962639			
Total	45215.4194	6				

Lu₂O₃

Groups	Count	Sum	Average	Variance
U20C	1	0.2274	0.2274	#DIV/o!
U20K	1	1.819	1.819	#DIV/o!
U20N	2	0.887	0.4435	0.0041405

ANOVA

Source of Variation	SS	df	MS	F	P-value	F crit
Between Groups	1.60264737	2	0.801323685	193.5330721	0.050762982	199.5
Within Groups	0.0041405	1	0.0041405			
Total	1.60678787	3				

MgO

Groups	Count	Sum	Average	Variance
U20A2	4	0.4381	0.109525	0.004454903
U20AR	1	0.6991	0.6991	#DIV/o!
U20C	1	0.1326	0.1326	#DIV/o!
U20K	1	0.06	0.06	#DIV/o!
U20M	1	1.023	1.023	#DIV/o!
U20N	1	0.1186	0.1186	#DIV/o!

ANOVA

Source of Variation	SS	df	MS	F	P-value	F crit
Between Groups	0.939854993	5	0.187970999	42.1941891	0.005565798	9.013455168
Within Groups	0.013364708	3	0.004454903			
Total	0.9532197	8				

MnO

Groups	Count	Sum	Average	Variance
U20A2	5	0.24877	0.049754	0.001573911
U20AR	1	0.08929	0.08929	#DIV/o!
U20C	2	0.14988	0.07494	0.001608579
U20K	1	0.12	0.12	#DIV/o!
U20M	1	0.1286	0.1286	#DIV/o!
U20N	1	0.09075	0.09075	#DIV/o!
U20Y	2	0.12553	0.062765	4.02305E-05

ANOVA

Source of Variation	SS	df	MS	F	P-value	F crit
Between Groups	0.008798584	6	0.001466431	1.10751284	0.452257206	4.283865714
Within Groups	0.007944454	6	0.001324076			
Total	0.016743038	12				

Na₂O

Groups	Count	Sum	Average	Variance
U20A2	5	16.335	3.267	0.598533
U20AR	1	2.818	2.818	#DIV/o!
U20C	2	5.88	2.94	0.842402
U20K	1	5.78	5.78	#DIV/o!
U20M	1	4.858	4.858	#DIV/o!
U20N	3	9.822	3.274	0.806416
U20Y	2	4.665	2.3325	0.4694805

ANOVA

Source of Variation	SS	df	MS	F	P-value	F crit
Between Groups	10.92000923	6	1.820001539	2.73743796	0.094512993	3.58058032
Within Groups	5.3188465	8	0.664855813			
Total	16.23885573	14				

Nb₂O₅

Groups	Count	Sum	Average	Variance
U20A2	5	145.65	29.13	142.0039
U20AR	1	43.68	43.68	#DIV/o!
U20C	2	59.32	29.66	30.5762
U20M	1	79.02	79.02	#DIV/o!
U20N	1	35.18	35.18	#DIV/o!
U20Y	2	49.86	24.93	175.5938

ANOVA

Source of Variation	SS	df	MS	F	P-value	F crit
Between Groups	2440.832025	5	488.166405	3.783328481	0.068048704	4.387374187
Within Groups	774.1856	6	129.0309333			
Total	3215.017625	11				

Nd₂O₃

Groups	Count	Sum	Average	Variance
U20A2	1	81.64	81.64	#DIV/o!
U20C	1	31.49	31.49	#DIV/o!
U20N	2	59.49	29.745	16.99445

ANOVA						
Source of Variation	SS	df	MS	F	P-value	F crit
Between Groups	1976.82365	2	988.411825	58.16085987	0.092323187	199.5
Within Groups	16.99445	1	16.99445			
Total	1993.8181	3				

P₂O₅

Groups	Count	Sum	Average	Variance
U20A2	4	0.08853	0.0221325	0.00042799
U20AR	1	0.08025	0.08025	#DIV/o!
U20C	1	0.05728	0.05728	#DIV/o!
U20K	1	0.01	0.01	#DIV/o!
U20M	1	0.3373	0.3373	#DIV/o!
U20N	1	0.01679	0.01679	#DIV/o!
U20Y	1	0.02107	0.02107	#DIV/o!

ANOVA						
Source of Variation	SS	df	MS	F	P-value	F crit
Between Groups	0.088918601	6	0.014819767	34.62641438	0.007303623	8.940645121
Within Groups	0.001283971	3	0.00042799			
Total	0.090202572	9				

PbO

Groups	Count	Sum	Average	Variance
U20A2	3	140.05	46.68333333	618.9160333
U20C	1	8.618	8.618	#DIV/o!

ANOVA						
Source of Variation	SS	df	MS	F	P-value	F crit
Between Groups	1086.727201	1	1086.727201	1.75585563	0.316261622	18.51282051
Within Groups	1237.832067	2	618.9160333			
Total	2324.559268	3				

Rb₂O

Groups	Count	Sum	Average	Variance
U20A2	2	469.6	234.8	84.5
U20AR	1	187.5	187.5	#DIV/o!
U20C	2	200.57	100.285	12297.82445
U20K	1	310	310	#DIV/o!
U20M	1	157.6	157.6	#DIV/o!
U20N	3	602.5	200.8333333	191.2633333
U20Y	2	393.3	196.65	1496.045

ANOVA

Source of Variation	SS	df	MS	F	P-value	F crit
Between Groups	35867.61871	6	5977.936451	2.095918939	0.217071333	4.950288069
Within Groups	14260.89612	5	2852.179223			
Total	50128.51483	11				

Sb₂O₃

Groups	Count	Sum	Average	Variance
U20C	1	0.05986	0.05986	#DIV/o!
U20K	1	0.838	0.838	#DIV/o!
U20N	2	2.0475	1.02375	0.341551125

ANOVA

Source of Variation	SS	df	MS	F	P-value	F crit
Between Groups	0.633168962	2	0.316584481	0.926902176	0.591953922	199.5
Within Groups	0.341551125	1	0.341551125			
Total	0.974720087	3				

Sc₂O₃

Groups	Count	Sum	Average	Variance
U20A2	1	4.596	4.596	#DIV/o!
U20K	1	2.145	2.145	#DIV/o!
U20N	2	6.665	3.3325	0.4656125

ANOVA						
Source of Variation	SS	df	MS	F	P-value	F crit
Between Groups	3.0051445	2	1.50257225	3.227087439	0.366269041	199.5
Within Groups	0.4656125	1	0.4656125			
Total	3.470757	3				

SiO₂

Groups	Count	Sum	Average	Variance
U20A2	5	379.2	75.84	5.18375
U20AR	1	70.04	70.04	#DIV/o!
U20C	2	145.62	72.81	17.5232
U20K	1	72.17	72.17	#DIV/o!
U20M	1	61.11	61.11	#DIV/o!
U20N	1	74.22	74.22	#DIV/o!
U20Y	2	145.28	72.64	0.0128

ANOVA						
Source of Variation	SS	df	MS	F	P-value	F crit
Between Groups	192.8281231	6	32.13802051	5.038491889	0.034882144	4.283865714
Within Groups	38.271	6	6.3785			
Total	231.0991231	12				

Sm₂O₃

Groups	Count	Sum	Average	Variance
U20C	1	6.377	6.377	#DIV/o!
U20K	1	24.93	24.93	#DIV/o!
U20N	2	11.248	5.624	0.060552

ANOVA						
Source of Variation	SS	df	MS	F	P-value	F crit
Between Groups	272.6977748	2	136.3488874	2251.765216	0.014899622	199.5
Within Groups	0.060552	1	0.060552			
Total	272.7583268	3				

SrO

Groups	Count	Sum	Average	Variance
U20A2	5	279.32	55.864	1775.56443
U20AR	1	208.2	208.2	#DIV/o!
U20C	2	93.95	46.975	0.21125
U20M	1	536.9	536.9	#DIV/o!
U20N	1	64.56	64.56	#DIV/o!
U20Y	2	80.42	40.21	138.1122

ANOVA						
Source of Variation	SS	df	MS	F	P-value	F crit
Between Groups	226023.3303	5	45204.66606	37.45942349	0.000189456	4.387374187
Within Groups	7240.58117	6	1206.763528			
Total	233263.9115	11				

Ta₂O₅

Groups	Count	Sum	Average	Variance
U20K	1	8.914	8.914	#DIV/o!
U20N	2	3.492	1.746	0.050562

ANOVA						
Source of Variation	SS	df	MS	F	P-value	F crit
Between Groups	34.25348267	1	34.25348267	677.4550585	0.024447042	161.4476388
Within Groups	0.050562	1	0.050562			
Total	34.30404467	2				

Tb₂O₃

Groups	Count	Sum	Average	Variance
U20C	1	0.3452	0.3452	#DIV/o!
U20K	1	3.337	3.337	#DIV/o!
U20N	2	1.4615	0.73075	0.000595125

ANOVA						
Source of Variation	SS	df	MS	F	P-value	F crit
Between Groups	5.708310743	2	2.854155371	4795.892243	0.010210045	199.5
Within Groups	0.000595125	1	0.000595125			
Total	5.708905868	3				

ThO₂

Groups	Count	Sum	Average	Variance
U20C	1	17.07	17.07	#DIV/o!
U20K	1	47.11	47.11	#DIV/o!
U20N	2	54.05	27.025	2.85605

ANOVA						
Source of Variation	SS	df	MS	F	P-value	F crit
Between Groups	476.855025	2	238.4275125	83.48156107	0.077160144	199.5
Within Groups	2.85605	1	2.85605			
Total	479.711075	3				

TiO₂

Groups	Count	Sum	Average	Variance
U20A2	5	0.63368	0.126736	0.004332968
U20AR	1	0.287	0.287	#DIV/o!
U20C	2	0.25172	0.12586	0.006644739
U20K	1	0.25	0.25	#DIV/o!
U20M	1	0.9638	0.9638	#DIV/o!
U20N	1	0.1938	0.1938	#DIV/o!
U20Y	2	0.3225	0.16125	0.004186125

ANOVA

Source of Variation	SS	df	MS	F	P-value	F crit
Between Groups	0.62729361	6	0.104548935	22.27388572	0.000742975	4.283865714
Within Groups	0.028162738	6	0.00469379			
Total	0.655456348	12				

UO₂

Groups	Count	Sum	Average	Variance
U20C	1	3.403	3.403	#DIV/o!
U20N	2	10.331	5.1655	0.0055125

ANOVA

Source of Variation	SS	df	MS	F	P-value	F crit
Between Groups	2.0709375	1	2.0709375	375.6802721	0.032816029	161.4476388
Within Groups	0.0055125	1	0.0055125			
Total	2.07645	2				

Y₂O₃

Groups	Count	Sum	Average	Variance
U20A2	5	201	40.2	239.67145
U20AR	1	38.57	38.57	#DIV/o!
U20C	2	59.25	29.625	70.44845
U20M	1	63.52	63.52	#DIV/o!
U20N	1	28.79	28.79	#DIV/o!
U20Y	2	74.18	37.09	15.7922

ANOVA

Source of Variation	SS	df	MS	F	P-value	F crit
Between Groups	895.3338417	5	179.0667683	1.028206923	0.477056851	4.387374187
Within Groups	1044.92645	6	174.1544083			
Total	1940.260292	11				

Yb₂O₃

Groups	Count	Sum	Average	Variance
U20A2	3	12.526	4.175333333	1.729761333
U20C	1	2.277	2.277	#DIV/o!
U20K	1	16.17	16.17	#DIV/o!
U20N	2	5.909	2.9545	0.1090445

ANOVA

Source of Variation	SS	df	MS	F	P-value	F crit
Between Groups	142.0860057	3	47.3620019	39.81598189	0.006462274	9.276628153
Within Groups	3.568567167	3	1.189522389			
Total	145.6545729	6				

ZnO

Groups	Count	Sum	Average	Variance
U20A2	2	123.95	61.975	1104.97005
U20AR	1	74.04	74.04	#DIV/o!
U20C	2	78.86	39.43	0.32
U20K	1	250.1	250.1	#DIV/o!
U20M	1	139.7	139.7	#DIV/o!
U20N	3	208.75	69.58333333	17.69853333
U20Y	2	103.13	51.565	35.53245

ANOVA						
Source of Variation	SS	df	MS	F	P-value	F crit
Between Groups	38389.27853	6	6398.213088	27.19820886	0.001149623	4.950288069
Within Groups	1176.219567	5	235.2439133			
Total	39565.49809	11				

ZrO₂

Groups	Count	Sum	Average	Variance
U20A2	5	892.36	178.472	5721.52492
U20AR	1	260.8	260.8	#DIV/o!
U20C	2	156.25	78.125	601.00445
U20M	1	974.5	974.5	#DIV/o!
U20N	1	270	270	#DIV/o!
U20Y	2	479.8	239.9	6635.52

ANOVA						
Source of Variation	SS	df	MS	F	P-value	F crit
Between Groups	610189.5182	5	122037.9036	24.30822158	0.000647421	4.387374187
Within Groups	30122.62413	6	5020.437355			
Total	640312.1423	11				

AII.2 ANOVA Results for Density by Depth, Location, Lithology, and Stratigraphy

Bulk density by depth

Groups	Count	Sum	Average	Variance
Above 574.1-m	55090	107209.6	1.946080958	0.06867093
574.1 - 645.1-m	7299	14336.29	1.964144403	0.012336658
Below 645.1-m	3319	6225.92	1.875842121	0.087220139

ANOVA						
Source of Variation	SS	df	MS	F	P-value	F crit
Between Groups	18.59974181	2	9.299870904	146.8003599	0	2.995868864
Within Groups	4162.442232	65705	0.063350464			
Total	4181.041974	65707				

Bulk density by location

Groups	Count	Sum	Average	Variance
U20AM	775	1332.00	1.72	0.03
U20AP	775	1644.29	2.12	0.05
U20AW	775	1641.70	2.12	0.03
U20AX	775	1409.37	1.82	0.06
U20AZ	775	1670.64	2.16	0.06
U20BB	775	1281.84	1.65	0.04
U20BD	775	1400.28	1.81	0.07
U20BD1	775	1349.49	1.74	0.05
U20BD2	775	1349.49	1.74	0.05
U20BE	775	1351.45	1.74	0.05
U20BF	775	1314.67	1.70	0.04

ANOVA						
Source of Variation	SS	df	MS	F	P-value	F crit
Between Groups	276.0293384	10	27.60293384	584.3587646	0	1.83181215
Within Groups	402.1696823	8514	0.047236279			
Total	678.1990207	8524				

Bulk density by lithology

Groups	Count	Sum	Average	Variance
BED	22663	42090.41	1.86	0.04
DWT	1948	4248.38	2.18	0.05
FB	1852	3666.07	1.98	0.05
LA	6667	13515.89	2.03	0.04
MWT	7102	15309.12	2.16	0.05
NWT	4700	8341.11	1.77	0.03
PL	2217	4197.22	1.89	0.01
PWT	2342	4582.71	1.96	0.05
VT	649	1438.90	2.22	0.04
WT	1369	2853.18	2.08	0.04
OTHER	14199	27528.82	1.94	0.08

ANOVA						
Source of Variation	SS	df	MS	F	P-value	F crit
Between Groups	863.0020155	10	86.30020155	1708.739018	0	1.830847416
Within Groups	3318.039958	65697	0.050505197			
Total	4181.041974	65707				

Bulk density by stratigraphy

Groups	Count	Sum	Average	Variance
Tfb	540	903.56	1.67	0.05
Tfbr	444	766.78	1.73	0.03
Tfbw	319	479.47	1.50	0.02
Tgh	540	1059.45	1.96	0.04
Thp	540	922.58	1.71	0.03
Tm	540	1073.65	1.99	0.03
Tmat	540	821.55	1.52	0.02
Tmaw	540	942.57	1.75	0.07
Tmawp	540	886.62	1.64	0.01
Tmawr	441	771.76	1.75	0.04
Tmrb	85	127.52	1.50	0.01
Tmrf	540	890.14	1.65	0.01
Tmri	540	1132.61	2.10	0.03
Tmrp	540	1165.86	2.16	0.04
Tmrr	540	1018.49	1.89	0.06
Tp	540	940.32	1.74	0.02
Tpb	540	1075.77	1.99	0.05
Tpcm	540	1110.81	2.06	0.05
Tpd	540	966.25	1.79	0.03
Tpe	540	1135.27	2.10	0.06
Tpr	540	1007.28	1.87	0.04
Tps	94	164.67	1.75	0.02
Tptb	20	38.41	1.92	0.00
TPw	19	39.27	2.07	0.01
Ttp	540	952.18	1.76	0.04
Tr	540	950.72	1.76	0.08
Ttt	424	821.55	1.94	0.07
Other	540	957.03	1.77	0.02

ANOVA						
Source of Variation	SS	df	MS	F	P-value	F crit
Between Groups	387.4036883	27	14.34828475	369.1974448	0	1.486566435
Within Groups	490.3789545	12618	0.038863445			
Total	877.7826428	12645				

AII.3 ANOVA Results for Water Content by Depth, Location, Lithology, and Stratigraphy

H₂O weight fraction by depth

Groups	Count	Sum	Average	Variance
Above 574.1-m	40331	425771.9	10.55693883	32.7074715
574.1 - 645.1-m	5675	90641.6	15.97208811	16.59845942
Below 645.1-m	1396	26496.5	18.98030086	24.9053536

ANOVA

Source of Variation	SS	df	MS	F	P-value	F crit
Between Groups	227376.2516	2	113688.1258	3721.441872	0	2.995921619
Within Groups	1448014.953	47399	30.54948317			
Total	1675391.204	47401				

H₂O weight fraction by location

Groups	Count	Sum	Average	Variance
U20AP	2253	19996.6	8.875543719	17.2233137
U20AW	2253	15623.4	6.93448735	5.806167999
U20AX	2253	14448.8	6.413138038	23.6113282
U20AZ	2253	16512.3	7.329027963	23.13072894
U20BB	2253	17426.5	7.734798047	23.55234984
U20BD	2253	23679.4	10.51016423	23.45445703
U20BE	2253	16090.5	7.141810919	25.15331324
U20BF	2253	16039.9	7.119351975	17.62890597

ANOVA

Source of Variation	SS	df	MS	F	P-value	F crit
Between Groups	27671.90984	7	3953.129977	198.2008514	1.8555E-284	2.010097244
Within Groups	359330.3922	18016	19.94507062			
Total	387002.3021	18023				

H₂O weight fraction by location and depth (“IN Rc”)

Groups	Count	Sum	Average	Variance		
U20AZ	578	9848.4	17.03875433	3.857698272		
U20BD	382	6580.5	17.22643979	5.611871281		
U20BE	578	10317.2	17.84982699	8.459973973		
U20BF	578	7681.8	13.29031142	7.880564548		
U20AP	417	3565.3	8.549880096	9.278852149		
U20AW	578	9200.5	15.91782007	2.415609104		
U20AX	578	8549.4	14.79134948	5.310982231		
ANOVA						
Source of Variation	SS	df	MS	F	P-value	F crit
Between Groups	28495.61217	6	4749.268695	790.8735037	0	2.101047654
Within Groups	22110.75128	3682	6.005092689			
Total	50606.36345	3688				

H₂O weight fraction by lithology

Groups	Count	Sum	Average	Variance		
BED	10410	166590.2	16.00290106	19.98665313		
DWT	106	493.6	4.656603774	1.62819407		
FB	1180	13896.7	11.77686441	7.950007123		
LA	2624	16885.7	6.435099085	14.04918695		
MWT	3271	15222.7	4.653836747	13.7187368		
NWT	1554	19892.4	12.8007722	17.42936193		
PL	368	3929.9	10.67907609	25.71108688		
PWT	1756	19086.3	10.86919134	31.52411581		
VT	184	1482.5	8.057065217	28.59415746		
BLANKS	6404	49547.4	7.736945659	26.24381987		
ANOVA						
Source of Variation	SS	df	MS	F	P-value	F crit
Between Groups	526819.4811	9	58535.49789	2888.105997	0	1.880221226
Within Groups	564396.8786	27847	20.26778032			
Total	1091216.36	27856				

H₂O weight fraction by stratigraphy

Groups	Count	Sum	Average	Variance
Tfbr	382	5726.2	14.99005236	5.604467714
Tfbw	232	3416.6	14.72672414	9.145429915
Tgh	382	6202	16.23560209	2.883821028
Tmat	382	5367.3	14.05052356	10.69095773
Thp	382	3434.6	8.991099476	16.36984183
Tmaw	382	3666.9	9.59921466	10.03362143
Tmawp	302	3349.9	11.09238411	4.716320543
Tmawr	183	1377.9	7.529508197	7.983300306
Tmrb	54	550.8	10.2	19.81924528
Tmrf	382	5920.5	15.4986911	17.04800353
Tmri	382	2537.5	6.642670157	12.25132409
Tmrp	382	2310.4	6.048167539	11.73720136
Tmrr	361	2882.4	7.984487535	10.62931425
Tp	382	5151.6	13.48586387	15.48048206
Tpb	382	1309.8	3.428795812	6.500743428
Tpcm	382	4784.4	12.52460733	24.04002281
Tpd	379	6642.6	17.52664908	11.11735673
Tpe	195	3533.7	18.12153846	9.943038858
Tpr	14	236.9	16.92142857	0.321813187
Tps	77	1272.7	16.52857143	11.60601504
Tptb	18	323.3	17.96111111	0.148398693
TPw	10	95.7	9.57	0.917888889
Ttp	382	3185.7	8.339528796	11.25095306
Ttr	304	3836.8	12.62105263	22.37302067
Ttt	154	1072.7	6.965584416	19.9520758
BLANK	382	6455.2	16.89842932	15.10671669

ANOVA						
Source of Variation	SS	df	MS	F	P-value	F crit
Between Groups	126393.0846	25	5055.723386	418.2966217	0	1.507626921
Within Groups	87300.46604	7223	12.08645522			
Total	213693.5507	7248				

APPENDIX III: MCNP INPUT DECK

The following is the input deck employed in the MCNP6 neutron transport test case discussed in §3.2.1.

```
Neutron Transport for FAT/ORIGEN Geology Model   R. Boone Gilbreath   13 MAR 17
c BEGIN CELL CARD DECK
c Geology Spheres
1 0      99 -10 imp:n=1  tmp=8.617E-4
2 1 -1.957 10 -20 imp:n=1  tmp=1.721E-7
3 1 -1.957 20 -30 imp:n=1  tmp=1.721E-7
4 1 -1.957 30 -40 imp:n=1  tmp=1.721E-7
5 1 -1.957 40 -50 imp:n=1  tmp=1.721E-7
6 1 -1.957 50 -60 imp:n=1  tmp=1.721E-7
9 0      -99 imp:n=0  tmp=8.617E-4
c Model Space
7 0 60 -70 imp:n=1
c Model exterior
88 0 70 imp:n=0
c END CELL CARD DECK
c -----
c -----
c BEGIN SURFACE CARD DECK
10 SO 50
20 SO 80
30 SO 120
40 SO 160
50 SO 180
60 SO 200
70 SO 201
99 SO 49.999
c END SURFACE CARD DECK
c -----
c -----
c BEGIN DATA CARD DECK
c Neutron library inputs
mode n
c Define Material for Geology
M1  1001.71c  1.9018E-02
    1002.71c  2.1873E-06
    8016.71c  5.6067E-01
    11023.71c 2.0546E-02
    12024.71c 4.7792E-04
    12025.71c 6.0503E-05
    12026.71c 6.6614E-05
    13027.71c 6.3794E-02
    14028.71c 2.7066E-01
    14029.71c 1.3750E-02
    14030.71c 9.0747E-03
    15031.71c 6.1978E-05
    19039.71c 2.9241E-02
    19040.71c 3.6685E-06
    19041.71c 2.1102E-03
```

20040.71c	2.6273E-03
20042.71c	1.7535E-05
20043.71c	3.6588E-06
20044.71c	5.6536E-05
20046.71c	1.0841E-07
20048.71c	5.0682E-06
21045.71c	1.8519E-08
22046.71c	8.1067E-05
22047.71c	7.3108E-05
22048.71c	7.2440E-04
22049.71c	5.3160E-05
22050.71c	5.0900E-05
25055.71c	5.7650E-04
26054.71c	3.6101E-04
26056.71c	5.6670E-03
26057.71c	1.3088E-04
26058.71c	1.7417E-05
27059.71c	2.9605E-09
30000.71c	4.7289E-07
33075.71c	1.7002E-08
37085.71c	1.0194E-06
37087.71c	3.9310E-07
38084.71c	2.5860E-09
38086.71c	4.5533E-08
38087.71c	3.2325E-08
38088.71c	3.8135E-07
39089.71c	2.6399E-07
40090.71c	8.6992E-07
40091.71c	1.8971E-07
40092.71c	2.8997E-07
40094.71c	2.9386E-07
40096.71c	4.7343E-08
41093.71c	2.0803E-07
42092.71c	1.8434E-09
42094.71c	1.1608E-09
42095.71c	2.0096E-09
42096.71c	2.1149E-09
42097.71c	1.2179E-09
42098.71c	3.0943E-09
42100.71c	1.2458E-09
51121.71c	2.5896E-09
51123.71c	1.9369E-09
55133.71c	4.2291E-08
56130.71c	2.0715E-09
56132.71c	1.9738E-09
56134.71c	4.7235E-08
56135.71c	1.2883E-07
56136.71c	1.5349E-07
56137.71c	2.1950E-07
56138.71c	1.4012E-06
57138.71c	6.2705E-10
57139.71c	7.0543E-07
58136.71c	2.7484E-09
58138.71c	3.7289E-09
58140.71c	1.3140E-06
58142.71c	1.6511E-07
60142.71c	5.8570E-08
60143.71c	2.6261E-08
60144.71c	5.1335E-08

60145.71c	1.7889E-08		
60146.71c	3.7079E-08		
60148.71c	1.2416E-08		
60150.71c	1.2162E-08		
62144.71c	1.2595E-09		
62147.71c	6.1499E-09		
62148.71c	4.6114E-09		
62149.71c	5.6699E-09		
62150.71c	3.0278E-09		
62152.71c	1.0975E-08		
62154.71c	9.3336E-09		
63151.71c	1.1460E-09		
63153.71c	1.2510E-09		
65159.71c	5.3703E-09		
71175.71c	3.2134E-09		
71176.71c	8.5745E-11		
72174.71c	7.1048E-11		
72176.71c	2.3357E-09		
72177.71c	8.2594E-09		
72178.71c	1.2114E-08		
72179.71c	6.0480E-09		
72180.71c	1.5577E-08		
73181.71c	1.2094E-08		
74182.71c	3.5864E-09		
74183.71c	1.9367E-09		
74184.71c	4.1467E-09		
74186.71c	3.8476E-09		
79197.71c	4.0603E-11		
90232.71c	2.0090E-07		
92234.71c	2.0799E-12		
92235.71c	2.7747E-10		
92238.71c	3.8237E-08	\$ 73180.71c 1.4526E-12	74180.71c 1.6240E-11

c Source Definition

SDEF SUR=99 PAR=n ERG=D1 NRM=+1
 SP1 -3 0.966 2.842

c Surface Flux Tally

F12:n 10
 F22:n 20
 F32:n 30
 F42:n 40
 F52:n 50
 F62:n 60

C Energy Bin Specification

E0 0
 1.000E-11
 5.000E-10
 2.000E-09
 5.000E-09
 1.000E-08
 1.450E-08
 2.100E-08
 3.000E-08
 4.000E-08
 5.000E-08
 7.000E-08
 1.000E-07
 1.250E-07
 1.500E-07
 1.840E-07

2.250E-07
2.750E-07
3.250E-07
3.668E-07
4.140E-07
5.000E-07
5.316E-07
6.251E-07
6.826E-07
8.000E-07
8.764E-07
1.000E-06
1.040E-06
1.080E-06
1.125E-06
1.300E-06
1.445E-06
1.855E-06
2.382E-06
3.059E-06
3.928E-06
5.044E-06
6.476E-06
8.315E-06
1.068E-05
1.371E-05
1.760E-05
2.260E-05
2.902E-05
3.727E-05
4.785E-05
6.144E-05
7.889E-05
1.013E-04
1.301E-04
1.670E-04
2.145E-04
2.754E-04
3.536E-04
4.540E-04
5.830E-04
7.485E-04
9.611E-04
1.234E-03
1.585E-03
2.035E-03
2.249E-03
2.485E-03
2.613E-03
2.747E-03
3.035E-03
3.355E-03
3.707E-03
4.307E-03
5.531E-03
7.102E-03
9.119E-03
1.060E-02
1.171E-02

1.503E-02
1.931E-02
2.188E-02
2.358E-02
2.418E-02
2.479E-02
2.606E-02
2.700E-02
2.850E-02
3.183E-02
3.431E-02
4.087E-02
4.631E-02
5.248E-02
5.656E-02
6.738E-02
7.200E-02
7.950E-02
8.250E-02
8.652E-02
9.804E-02
1.111E-01
1.168E-01
1.228E-01
1.291E-01
1.357E-01
1.426E-01
1.500E-01
1.576E-01
1.657E-01
1.742E-01
1.832E-01
1.926E-01
2.024E-01
2.128E-01
2.237E-01
2.352E-01
2.472E-01
2.732E-01
2.873E-01
2.945E-01
2.972E-01
2.985E-01
3.020E-01
3.337E-01
3.688E-01
3.877E-01
4.076E-01
4.505E-01
4.979E-01
5.234E-01
5.502E-01
5.784E-01
6.081E-01
6.393E-01
6.721E-01
7.065E-01
7.427E-01
7.808E-01

8.209E-01
8.629E-01
9.072E-01
9.616E-01
1.003E+00
1.108E+00
1.165E+00
1.225E+00
1.287E+00
1.353E+00
1.423E+00
1.496E+00
1.572E+00
1.653E+00
1.738E+00
1.827E+00
1.921E+00
2.019E+00
2.123E+00
2.231E+00
2.307E+00
2.346E+00
2.365E+00
2.385E+00
2.466E+00
2.592E+00
2.725E+00
2.865E+00
3.012E+00
3.166E+00
3.329E+00
3.679E+00
4.066E+00
4.493E+00
4.724E+00
4.966E+00
5.221E+00
5.488E+00
5.770E+00
6.065E+00
6.376E+00
6.592E+00
6.703E+00
7.047E+00
7.408E+00
7.788E+00
8.187E+00
8.607E+00
9.048E+00
9.512E+00
1.000E+01
1.051E+01
1.105E+01
1.162E+01
1.221E+01
1.252E+01
1.284E+01
1.350E+01
1.384E+01

```
1.419E+01
1.455E+01
1.492E+01
1.568E+01
1.649E+01
1.691E+01
1.733E+01
1.964E+01
2.000E+01
c Weight Window Generation
WWG 62 0 0 4j 0
WWP:n 5 3 5 0 -1 0 0.5 0 0
c Print Cards
MESH GEOM=SPH REF=0 0 0 ORIGIN=0 0 0 AXS=0 0 1 VEC=1 0 0
    IMESH=50 200 IINTS=1 30
    JMESH=180 JINTS=1
    KMESH=360 KINTS=1
c Cosine Tally
C0 0 1
c Precision Cutoff
stop F62 0.005
print
c END DATA CARD DECK
c -----
```

APPENDIX IV: RASH OXIDE MATRICES

In the following table are preliminary chemical oxide matrices used in producing the first NUGETS sample variant based on Kelly Rash's work. The "NV-2x" matrix includes a nominal amount of uranyl nitrate hexahydrate as a surrogate for residual nuclear fuel. Barium, Rb, Sr, Zr, and Y are also included as representative fission products. Each matrix recipe is normalized to 100 wt-%; figures are as reported in the literature.

Compound	NV-1x	NV-2x
SiO ₂	71.27	70.48
Al ₂ O ₃	14.36	1.42
TiO ₂	0.34	0.32
Fe ₂ O ₃	2.48	2.45
MgO	0.75	0.75
CaO	3.58	2.67
NaOH	1.52	3.00
KOH	5.38	5.32
MnO	0.07	0.07
Ca ₃ (PO ₄) ₂	0.26	0.53
BaO	-	9.6 x 10 ⁻²
RbCl	-	1.8 x 10 ⁻²
SrO	-	4.8 x 10 ⁻²
Zr(NO ₃) ₄	-	5.6 x 10 ⁻²
YCl	-	1.0 x 10 ⁻⁴
UO ₂ (NO ₃) ₂ · 6H ₂ O	-	1.9 x 10 ⁻⁵
TOTAL	100.00	100.00

APPENDIX V: FALLOUT ANALYSIS TOOL DATA

Subsections AV.1 and AV.2 present mass fraction data from FAT simulations for the WGPu-fueled IND by mass number (A) and atomic number (Z), respectively. Subsections AV.3 and AV.4 present the same data with respect to the WGU-fueled IND. Data are grouped by time step as noted.

AV.1 WGPu IND Mass Fraction Results by Mass Number (A) and Time

A	Precursor	1 s	1 min	1 h	1 d	1 wk	1 mo	1 yr
1	1.902E-02	1.903E-02	1.903E-02	1.903E-02	1.903E-02	1.903E-02	1.903E-02	1.903E-02
2	2.187E-06	5.141E-08	5.141E-08	5.141E-08	5.141E-08	5.141E-08	5.141E-08	5.141E-08
3	0.000E+00	2.266E-09	2.266E-09	2.266E-09	2.266E-09	2.266E-09	2.266E-09	2.266E-09
4	0.000E+00	3.731E-05	3.731E-05	3.731E-05	3.731E-05	3.731E-05	3.731E-05	3.731E-05
5	0.000E+00	0.000E+00	0.000E+00	0.000E+00	0.000E+00	0.000E+00	0.000E+00	0.000E+00
6	0.000E+00	1.088E-13	1.088E-13	1.088E-13	1.088E-13	1.088E-13	1.088E-13	1.088E-13
7	0.000E+00	2.365E-12	2.365E-12	2.365E-12	2.365E-12	2.365E-12	2.365E-12	2.365E-12
8	0.000E+00	1.081E-14	6.912E-36	0.000E+00	0.000E+00	0.000E+00	0.000E+00	0.000E+00
9	0.000E+00	4.016E-10	4.016E-10	4.016E-10	4.016E-10	4.016E-10	4.016E-10	4.016E-10
10	0.000E+00	1.454E-09	1.454E-09	1.454E-09	1.454E-09	1.454E-09	1.454E-09	1.454E-09
11	0.000E+00	9.772E-08	9.772E-08	9.772E-08	9.772E-08	9.772E-08	9.772E-08	9.772E-08
12	0.000E+00	2.856E-05	2.856E-05	2.856E-05	2.856E-05	2.856E-05	2.856E-05	2.856E-05
13	0.000E+00	1.104E-04	1.104E-04	1.104E-04	1.104E-04	1.104E-04	1.104E-04	1.104E-04
14	0.000E+00	6.489E-05	6.489E-05	6.489E-05	6.489E-05	6.489E-05	6.489E-05	6.489E-05
15	0.000E+00	4.225E-07	2.824E-07	2.819E-07	2.819E-07	2.819E-07	2.819E-07	2.819E-07
16	5.593E-01	5.590E-01	5.590E-01	5.590E-01	5.590E-01	5.590E-01	5.590E-01	5.590E-01
17	2.131E-04	2.273E-04	2.273E-04	2.273E-04	2.273E-04	2.273E-04	2.273E-04	2.273E-04
18	1.149E-03	1.261E-03	1.261E-03	1.261E-03	1.261E-03	1.261E-03	1.261E-03	1.261E-03
19	0.000E+00	2.454E-09	2.454E-09	2.454E-09	2.454E-09	2.454E-09	2.454E-09	2.454E-09
20	0.000E+00	1.734E-07	1.734E-07	1.734E-07	1.734E-07	1.734E-07	1.734E-07	1.734E-07
21	0.000E+00	2.746E-08	2.746E-08	2.746E-08	2.746E-08	2.746E-08	2.746E-08	2.746E-08
22	0.000E+00	3.869E-08	3.869E-08	3.869E-08	3.869E-08	3.869E-08	3.869E-08	3.869E-08

A	Precursor	1 s	1 min	1 h	1 d	1 wk	1 mo	1 yr
23	2.055E-02	2.054E-02	2.054E-02	2.054E-02	2.054E-02	2.054E-02	2.054E-02	2.054E-02
24	4.779E-04	4.724E-04	4.724E-04	4.724E-04	4.724E-04	4.724E-04	4.724E-04	4.724E-04
25	6.050E-05	7.213E-05	7.213E-05	7.214E-05	7.214E-05	7.214E-05	7.214E-05	7.214E-05
26	6.661E-05	7.271E-05	7.271E-05	7.271E-05	7.271E-05	7.271E-05	7.271E-05	7.271E-05
27	6.379E-02	6.379E-02	6.379E-02	6.379E-02	6.379E-02	6.379E-02	6.379E-02	6.379E-02
28	2.707E-01	2.696E-01	2.696E-01	2.696E-01	2.696E-01	2.696E-01	2.696E-01	2.696E-01
29	1.375E-02	1.418E-02	1.418E-02	1.418E-02	1.418E-02	1.418E-02	1.418E-02	1.418E-02
30	9.075E-03	9.667E-03	9.667E-03	9.667E-03	9.667E-03	9.667E-03	9.667E-03	9.667E-03
31	6.198E-05	6.214E-05	6.214E-05	6.214E-05	6.214E-05	6.214E-05	6.214E-05	6.214E-05
32	0.000E+00	2.157E-09	2.157E-09	2.157E-09	2.157E-09	2.157E-09	2.157E-09	2.157E-09
33	0.000E+00	6.693E-10	6.693E-10	6.693E-10	6.693E-10	6.693E-10	6.693E-10	6.693E-10
34	0.000E+00	9.322E-09	9.322E-09	9.322E-09	9.322E-09	9.322E-09	9.322E-09	9.322E-09
35	0.000E+00	2.851E-09	2.851E-09	2.851E-09	2.851E-09	2.851E-09	2.851E-09	2.851E-09
36	0.000E+00	6.409E-06	6.409E-06	6.409E-06	6.409E-06	6.409E-06	6.409E-06	6.409E-06
37	0.000E+00	2.656E-06	2.656E-06	2.656E-06	2.656E-06	2.656E-06	2.656E-06	2.656E-06
38	0.000E+00	2.246E-07	2.246E-07	2.246E-07	2.246E-07	2.246E-07	2.246E-07	2.246E-07
39	2.924E-02	2.912E-02	2.912E-02	2.912E-02	2.912E-02	2.912E-02	2.912E-02	2.912E-02
40	2.631E-03	2.622E-03	2.622E-03	2.622E-03	2.622E-03	2.622E-03	2.622E-03	2.622E-03
41	2.110E-03	2.210E-03	2.210E-03	2.210E-03	2.210E-03	2.210E-03	2.210E-03	2.210E-03
42	1.754E-05	1.872E-05	1.872E-05	1.872E-05	1.872E-05	1.872E-05	1.872E-05	1.872E-05
43	3.659E-06	3.922E-06	3.922E-06	3.922E-06	3.922E-06	3.922E-06	3.922E-06	3.922E-06
44	5.654E-05	6.211E-05	6.211E-05	6.211E-05	6.211E-05	6.211E-05	6.211E-05	6.211E-05
45	1.852E-08	2.259E-08	2.259E-08	2.259E-08	2.259E-08	2.259E-08	2.259E-08	2.259E-08
46	8.118E-05	7.792E-05	7.792E-05	7.792E-05	7.792E-05	7.792E-05	7.792E-05	7.792E-05
47	7.311E-05	7.169E-05	7.169E-05	7.169E-05	7.169E-05	7.169E-05	7.169E-05	7.169E-05

A	Precursor	1 s	1 min	1 h	1 d	1 wk	1 mo	1 yr
48	7.295E-04	7.315E-04	7.315E-04	7.315E-04	7.315E-04	7.315E-04	7.315E-04	7.315E-04
49	5.316E-05	5.439E-05	5.439E-05	5.439E-05	5.439E-05	5.439E-05	5.439E-05	5.439E-05
50	5.090E-05	5.311E-05	5.311E-05	5.311E-05	5.311E-05	5.311E-05	5.311E-05	5.311E-05
51	0.000E+00	5.334E-09	5.334E-09	5.334E-09	5.334E-09	5.334E-09	5.334E-09	5.334E-09
52	0.000E+00	7.955E-10	7.954E-10	7.955E-10	7.954E-10	7.954E-10	7.954E-10	7.954E-10
53	0.000E+00	2.579E-08	2.579E-08	2.579E-08	2.579E-08	2.579E-08	2.579E-08	2.579E-08
54	3.610E-04	3.486E-04	3.486E-04	3.486E-04	3.486E-04	3.486E-04	3.486E-04	3.486E-04
55	5.765E-04	5.765E-04	5.765E-04	5.765E-04	5.765E-04	5.765E-04	5.765E-04	5.765E-04
56	5.667E-03	5.675E-03	5.675E-03	5.675E-03	5.675E-03	5.675E-03	5.675E-03	5.675E-03
57	1.309E-04	1.339E-04	1.339E-04	1.339E-04	1.339E-04	1.339E-04	1.339E-04	1.339E-04
58	1.742E-05	1.807E-05	1.807E-05	1.807E-05	1.807E-05	1.807E-05	1.807E-05	1.807E-05
59	2.960E-09	4.220E-09	4.220E-09	4.220E-09	4.220E-09	4.220E-09	4.220E-09	4.220E-09
60	0.000E+00	3.263E-12	3.263E-12	3.263E-12	3.263E-12	3.263E-12	3.263E-12	3.263E-12
61	0.000E+00	5.701E-11	5.701E-11	5.701E-11	5.701E-11	5.701E-11	5.701E-11	5.701E-11
62	0.000E+00	2.877E-12	2.877E-12	2.877E-12	2.877E-12	2.877E-12	2.877E-12	2.877E-12
63	0.000E+00	2.934E-07	2.934E-07	2.934E-07	2.934E-07	2.934E-07	2.934E-07	2.934E-07
64	2.325E-07	2.247E-07	2.247E-07	2.247E-07	2.247E-07	2.247E-07	2.247E-07	2.247E-07
65	0.000E+00	1.350E-07	1.350E-07	1.350E-07	1.350E-07	1.350E-07	1.350E-07	1.350E-07
66	1.311E-07	1.330E-07	1.330E-07	1.330E-07	1.330E-07	1.330E-07	1.330E-07	1.330E-07
67	1.910E-08	1.985E-08	1.985E-08	1.985E-08	1.985E-08	1.985E-08	1.985E-08	1.985E-08
68	8.725E-08	9.208E-08	9.208E-08	9.208E-08	9.208E-08	9.208E-08	9.208E-08	9.208E-08
69	0.000E+00	9.478E-12	9.478E-12	9.478E-12	9.478E-12	9.478E-12	9.478E-12	9.478E-12
70	2.885E-09	3.134E-09	3.134E-09	3.134E-09	3.134E-09	3.134E-09	3.134E-09	3.134E-09
71	0.000E+00	1.787E-13	1.787E-13	1.787E-13	1.787E-13	1.787E-13	1.787E-13	1.787E-13
72	0.000E+00	9.937E-14	9.943E-14	9.943E-14	9.943E-14	9.943E-14	9.943E-14	9.943E-14

A	Precursor	1 s	1 min	1 h	1 d	1 wk	1 mo	1 yr
73	0.000E+00	1.542E-13	1.542E-13	1.542E-13	1.542E-13	1.542E-13	1.542E-13	1.542E-13
74	0.000E+00	3.666E-13	3.681E-13	3.681E-13	3.681E-13	3.681E-13	3.681E-13	3.681E-13
75	1.700E-08	1.698E-08	1.698E-08	1.698E-08	1.698E-08	1.698E-08	1.698E-08	1.698E-08
76	0.000E+00	1.620E-11	1.620E-11	1.620E-11	1.620E-11	1.620E-11	1.620E-11	1.620E-11
77	0.000E+00	2.127E-12	2.126E-12	2.126E-12	2.126E-12	2.126E-12	2.126E-12	2.126E-12
78	0.000E+00	4.724E-12	4.732E-12	4.732E-12	4.732E-12	4.732E-12	4.732E-12	4.732E-12
79	0.000E+00	1.242E-11	1.244E-11	1.244E-11	1.244E-11	1.244E-11	1.244E-11	1.244E-11
80	0.000E+00	1.847E-11	1.867E-11	1.867E-11	1.867E-11	1.867E-11	1.867E-11	1.867E-11
81	0.000E+00	3.246E-11	3.231E-11	3.231E-11	3.231E-11	3.231E-11	3.231E-11	3.231E-11
82	0.000E+00	6.317E-11	6.317E-11	6.317E-11	6.317E-11	6.317E-11	6.317E-11	6.317E-11
83	0.000E+00	1.069E-10	1.077E-10	1.077E-10	1.077E-10	1.077E-10	1.077E-10	1.077E-10
84	2.586E-09	2.655E-09	2.688E-09	2.688E-09	2.688E-09	2.688E-09	2.688E-09	2.688E-09
85	1.019E-06	1.012E-06	1.012E-06	1.012E-06	1.012E-06	1.012E-06	1.012E-06	1.012E-06
86	4.553E-08	4.571E-08	4.571E-08	4.572E-08	4.572E-08	4.572E-08	4.572E-08	4.572E-08
87	4.254E-07	4.321E-07	4.321E-07	4.321E-07	4.321E-07	4.321E-07	4.321E-07	4.321E-07
88	3.813E-07	3.831E-07	3.831E-07	3.831E-07	3.831E-07	3.831E-07	3.831E-07	3.831E-07
89	2.640E-07	2.646E-07	2.646E-07	2.646E-07	2.646E-07	2.646E-07	2.646E-07	2.646E-07
90	8.699E-07	8.580E-07	8.579E-07	8.579E-07	8.579E-07	8.579E-07	8.579E-07	8.579E-07
91	1.897E-07	1.902E-07	1.902E-07	1.902E-07	1.902E-07	1.902E-07	1.902E-07	1.902E-07
92	2.918E-07	2.950E-07	2.950E-07	2.950E-07	2.950E-07	2.950E-07	2.950E-07	2.950E-07
93	2.080E-07	2.093E-07	2.093E-07	2.093E-07	2.093E-07	2.093E-07	2.093E-07	2.093E-07
94	2.950E-07	3.051E-07	3.051E-07	3.051E-07	3.051E-07	3.051E-07	3.051E-07	3.051E-07
95	2.010E-09	3.605E-09	3.600E-09	3.600E-09	3.600E-09	3.600E-09	3.600E-09	3.600E-09
96	4.946E-08	5.361E-08	5.361E-08	5.361E-08	5.361E-08	5.361E-08	5.361E-08	5.361E-08
97	1.218E-09	2.975E-09	2.978E-09	2.978E-09	2.978E-09	2.977E-09	2.977E-09	2.977E-09

A	Precursor	1 s	1 min	1 h	1 d	1 wk	1 mo	1 yr
98	3.094E-09	4.965E-09	4.975E-09	4.975E-09	4.975E-09	4.975E-09	4.975E-09	4.975E-09
99	0.000E+00	1.977E-09	1.967E-09	1.967E-09	1.967E-09	1.967E-09	1.967E-09	1.967E-09
100	1.246E-09	3.411E-09	3.409E-09	3.409E-09	3.409E-09	3.409E-09	3.409E-09	3.409E-09
101	0.000E+00	2.068E-09	2.068E-09	2.067E-09	2.068E-09	2.068E-09	2.068E-09	2.068E-09
102	0.000E+00	2.115E-09	2.115E-09	2.115E-09	2.114E-09	2.114E-09	2.114E-09	2.114E-09
103	0.000E+00	2.107E-09	2.107E-09	2.107E-09	2.107E-09	2.107E-09	2.107E-09	2.107E-09
104	0.000E+00	1.823E-09	1.829E-09	1.829E-09	1.829E-09	1.829E-09	1.829E-09	1.829E-09
105	0.000E+00	1.507E-09	1.503E-09	1.503E-09	1.503E-09	1.503E-09	1.503E-09	1.503E-09
106	0.000E+00	1.058E-09	1.055E-09	1.055E-09	1.055E-09	1.055E-09	1.055E-09	1.055E-09
107	0.000E+00	7.034E-10	7.032E-10	7.032E-10	7.032E-10	7.032E-10	7.032E-10	7.032E-10
108	0.000E+00	3.853E-10	3.853E-10	3.853E-10	3.853E-10	3.853E-10	3.853E-10	3.853E-10
109	0.000E+00	2.020E-10	2.020E-10	2.020E-10	2.020E-10	2.020E-10	2.020E-10	2.020E-10
110	0.000E+00	1.288E-10	1.288E-10	1.288E-10	1.288E-10	1.288E-10	1.288E-10	1.288E-10
111	0.000E+00	7.808E-11	7.808E-11	7.808E-11	7.808E-11	7.808E-11	7.808E-11	7.808E-11
112	0.000E+00	5.583E-11	5.582E-11	5.582E-11	5.582E-11	5.582E-11	5.582E-11	5.582E-11
113	0.000E+00	4.451E-11	4.451E-11	4.451E-11	4.451E-11	4.451E-11	4.451E-11	4.451E-11
114	0.000E+00	3.514E-11	3.515E-11	3.515E-11	3.515E-11	3.515E-11	3.515E-11	3.515E-11
115	0.000E+00	3.625E-11	3.626E-11	3.626E-11	3.626E-11	3.626E-11	3.626E-11	3.626E-11
116	0.000E+00	3.095E-11	3.095E-11	3.095E-11	3.095E-11	3.095E-11	3.095E-11	3.095E-11
117	0.000E+00	3.048E-11	3.048E-11	3.048E-11	3.048E-11	3.048E-11	3.048E-11	3.048E-11
118	0.000E+00	3.533E-11	3.532E-11	3.532E-11	3.532E-11	3.532E-11	3.532E-11	3.532E-11
119	0.000E+00	3.203E-11	3.203E-11	3.203E-11	3.203E-11	3.203E-11	3.203E-11	3.203E-11
120	0.000E+00	3.338E-11	3.338E-11	3.338E-11	3.338E-11	3.338E-11	3.338E-11	3.338E-11
121	2.590E-09	2.599E-09	2.599E-09	2.599E-09	2.599E-09	2.599E-09	2.599E-09	2.599E-09
122	0.000E+00	4.524E-11	4.524E-11	4.524E-11	4.524E-11	4.524E-11	4.524E-11	4.524E-11

A	Precursor	1 s	1 min	1 h	1 d	1 wk	1 mo	1 yr
123	1.937E-09	1.994E-09	1.994E-09	1.994E-09	1.994E-09	1.994E-09	1.994E-09	1.994E-09
124	0.000E+00	5.303E-11	5.302E-11	5.302E-11	5.302E-11	5.302E-11	5.302E-11	5.302E-11
125	0.000E+00	6.191E-11	6.191E-11	6.191E-11	6.191E-11	6.191E-11	6.191E-11	6.191E-11
126	0.000E+00	7.943E-11	7.955E-11	7.955E-11	7.955E-11	7.955E-11	7.955E-11	7.955E-11
127	0.000E+00	1.375E-10	1.374E-10	1.374E-10	1.374E-10	1.374E-10	1.374E-10	1.374E-10
128	0.000E+00	2.373E-10	2.376E-10	2.376E-10	2.376E-10	2.376E-10	2.376E-10	2.376E-10
129	0.000E+00	5.056E-10	5.053E-10	5.053E-10	5.053E-10	5.053E-10	5.053E-10	5.053E-10
130	2.072E-09	2.862E-09	2.862E-09	2.862E-09	2.862E-09	2.862E-09	2.862E-09	2.862E-09
131	0.000E+00	1.506E-09	1.506E-09	1.506E-09	1.506E-09	1.506E-09	1.506E-09	1.506E-09
132	1.974E-09	4.111E-09	4.111E-09	4.111E-09	4.111E-09	4.111E-09	4.111E-09	4.111E-09
133	4.229E-08	4.517E-08	4.518E-08	4.518E-08	4.518E-08	4.518E-08	4.518E-08	4.518E-08
134	4.723E-08	4.930E-08	4.933E-08	4.933E-08	4.933E-08	4.933E-08	4.933E-08	4.933E-08
135	1.288E-07	1.296E-07	1.295E-07	1.296E-07	1.296E-07	1.296E-07	1.296E-07	1.296E-07
136	1.562E-07	1.576E-07	1.577E-07	1.577E-07	1.577E-07	1.577E-07	1.577E-07	1.577E-07
137	2.195E-07	2.216E-07	2.216E-07	2.216E-07	2.216E-07	2.216E-07	2.216E-07	2.216E-07
138	1.406E-06	1.414E-06	1.414E-06	1.414E-06	1.414E-06	1.414E-06	1.414E-06	1.414E-06
139	7.054E-07	7.078E-07	7.078E-07	7.078E-07	7.078E-07	7.078E-07	7.078E-07	7.078E-07
140	1.314E-06	1.314E-06	1.314E-06	1.314E-06	1.314E-06	1.314E-06	1.314E-06	1.314E-06
141	0.000E+00	2.555E-09	2.552E-09	2.552E-09	2.552E-09	2.552E-09	2.552E-09	2.552E-09
142	2.237E-07	2.270E-07	2.270E-07	2.270E-07	2.270E-07	2.270E-07	2.270E-07	2.270E-07
143	2.626E-08	2.823E-08	2.822E-08	2.822E-08	2.822E-08	2.822E-08	2.822E-08	2.822E-08
144	5.259E-08	5.442E-08	5.441E-08	5.441E-08	5.441E-08	5.441E-08	5.441E-08	5.441E-08
145	1.789E-08	1.966E-08	1.965E-08	1.965E-08	1.965E-08	1.965E-08	1.965E-08	1.965E-08
146	3.708E-08	3.898E-08	3.898E-08	3.898E-08	3.898E-08	3.898E-08	3.898E-08	3.898E-08
147	6.150E-09	7.139E-09	7.139E-09	7.139E-09	7.139E-09	7.139E-09	7.139E-09	7.139E-09

A	Precursor	1 s	1 min	1 h	1 d	1 wk	1 mo	1 yr
148	1.703E-08	1.808E-08	1.808E-08	1.808E-08	1.808E-08	1.808E-08	1.808E-08	1.808E-08
149	5.670E-09	6.326E-09	6.325E-09	6.325E-09	6.325E-09	6.325E-09	6.325E-09	6.325E-09
150	1.519E-08	1.616E-08	1.616E-08	1.616E-08	1.616E-08	1.616E-08	1.616E-08	1.616E-08
151	1.146E-09	1.533E-09	1.533E-09	1.533E-09	1.533E-09	1.533E-09	1.533E-09	1.533E-09
152	1.097E-08	1.135E-08	1.135E-08	1.135E-08	1.135E-08	1.135E-08	1.135E-08	1.135E-08
153	1.251E-09	1.482E-09	1.482E-09	1.482E-09	1.482E-09	1.482E-09	1.482E-09	1.482E-09
154	9.334E-09	9.662E-09	9.662E-09	9.662E-09	9.662E-09	9.662E-09	9.662E-09	9.662E-09
155	0.000E+00	9.689E-11	9.688E-11	9.689E-11	9.688E-11	9.689E-11	9.689E-11	9.689E-11
156	0.000E+00	5.197E-11	5.197E-11	5.197E-11	5.197E-11	5.197E-11	5.197E-11	5.197E-11
157	0.000E+00	3.260E-11	3.260E-11	3.260E-11	3.260E-11	3.260E-11	3.260E-11	3.260E-11
158	0.000E+00	1.802E-11	1.802E-11	1.802E-11	1.802E-11	1.802E-11	1.802E-11	1.802E-11
159	5.370E-09	5.355E-09	5.355E-09	5.355E-09	5.355E-09	5.355E-09	5.355E-09	5.355E-09
160	0.000E+00	2.775E-11	2.775E-11	2.775E-11	2.775E-11	2.775E-11	2.775E-11	2.775E-11
161	0.000E+00	2.145E-12	2.145E-12	2.145E-12	2.145E-12	2.145E-12	2.145E-12	2.145E-12
162	0.000E+00	1.311E-12	1.311E-12	1.311E-12	1.311E-12	1.311E-12	1.311E-12	1.311E-12
163	0.000E+00	6.823E-13	6.823E-13	6.823E-13	6.823E-13	6.823E-13	6.823E-13	6.823E-13
164	0.000E+00	3.936E-13	3.936E-13	3.936E-13	3.936E-13	3.936E-13	3.936E-13	3.936E-13
165	0.000E+00	2.056E-13	2.056E-13	2.056E-13	2.056E-13	2.056E-13	2.056E-13	2.056E-13
166	0.000E+00	1.416E-13	1.416E-13	1.416E-13	1.416E-13	1.416E-13	1.416E-13	1.416E-13
167	0.000E+00	7.064E-14	7.064E-14	7.064E-14	7.064E-14	7.064E-14	7.064E-14	7.064E-14
168	2.700E-11	2.757E-11	2.757E-11	2.757E-11	2.757E-11	2.757E-11	2.757E-11	2.757E-11
169	0.000E+00	1.162E-13	1.162E-13	1.162E-13	1.162E-13	1.162E-13	1.162E-13	1.162E-13
170	6.545E-10	6.523E-10	6.523E-10	6.523E-10	6.523E-10	6.523E-10	6.523E-10	6.523E-10
171	3.092E-09	3.086E-09	3.086E-09	3.086E-09	3.086E-09	3.086E-09	3.086E-09	3.086E-09
172	4.758E-09	4.764E-09	4.764E-09	4.764E-09	4.764E-09	4.764E-09	4.764E-09	4.764E-09

A	Precursor	1 s	1 min	1 h	1 d	1 wk	1 mo	1 yr
173	3.534E-09	3.539E-09	3.539E-09	3.539E-09	3.539E-09	3.539E-09	3.539E-09	3.539E-09
174	7.100E-09	7.091E-09	7.091E-09	7.091E-09	7.091E-09	7.091E-09	7.091E-09	7.091E-09
175	3.213E-09	3.205E-09	3.205E-09	3.205E-09	3.205E-09	3.205E-09	3.205E-09	3.204E-09
176	5.274E-09	5.242E-09	5.242E-09	5.242E-09	5.242E-09	5.242E-09	5.242E-09	5.242E-09
177	8.259E-09	8.154E-09	8.154E-09	8.154E-09	8.154E-09	8.153E-09	8.153E-09	8.153E-09
178	1.211E-08	1.210E-08	1.210E-08	1.210E-08	1.210E-08	1.210E-08	1.210E-08	1.210E-08
179	6.048E-09	6.064E-09	6.064E-09	6.064E-09	6.064E-09	6.064E-09	6.064E-09	6.064E-09
180	1.560E-08	1.572E-08	1.572E-08	1.572E-08	1.572E-08	1.572E-08	1.572E-08	1.572E-08
181	1.209E-08	1.207E-08	1.207E-08	1.207E-08	1.207E-08	1.207E-08	1.207E-08	1.207E-08
182	3.586E-09	3.579E-09	3.579E-09	3.579E-09	3.579E-09	3.579E-09	3.579E-09	3.579E-09
183	1.937E-09	1.930E-09	1.930E-09	1.930E-09	1.930E-09	1.930E-09	1.930E-09	1.930E-09
184	4.147E-09	4.146E-09	4.146E-09	4.146E-09	4.146E-09	4.146E-09	4.146E-09	4.146E-09
185	0.000E+00	4.444E-12	4.444E-12	4.444E-12	4.444E-12	4.444E-12	4.444E-12	4.444E-12
186	3.848E-09	3.887E-09	3.887E-09	3.887E-09	3.887E-09	3.887E-09	3.887E-09	3.887E-09
187	0.000E+00	3.905E-12	3.905E-12	3.905E-12	3.905E-12	3.905E-12	3.905E-12	3.905E-12
188	0.000E+00	3.755E-16	3.755E-16	3.755E-16	3.755E-16	3.755E-16	3.755E-16	3.755E-16
189	0.000E+00	2.105E-20	2.105E-20	2.105E-20	2.105E-20	2.105E-20	2.105E-20	2.105E-20
190	0.000E+00	2.587E-33	2.587E-33	2.587E-33	2.588E-33	2.587E-33	2.588E-33	2.587E-33
191	0.000E+00	1.346E-29	1.346E-29	1.346E-29	1.346E-29	1.346E-29	1.346E-29	1.346E-29
192	0.000E+00	1.837E-26	1.837E-26	1.837E-26	1.837E-26	1.837E-26	1.837E-26	1.837E-26
193	0.000E+00	2.341E-22	2.341E-22	2.341E-22	2.341E-22	2.341E-22	2.341E-22	2.341E-22
194	0.000E+00	1.215E-19	1.215E-19	1.215E-19	1.215E-19	1.215E-19	1.215E-19	1.215E-19
195	0.000E+00	1.242E-18	1.242E-18	1.242E-18	1.242E-18	1.242E-18	1.242E-18	1.242E-18
196	0.000E+00	1.688E-15	1.688E-15	1.688E-15	1.688E-15	1.688E-15	1.688E-15	1.688E-15
197	4.060E-11	4.051E-11	4.051E-11	4.051E-11	4.051E-11	4.051E-11	4.051E-11	4.051E-11

A	Precursor	1 s	1 min	1 h	1 d	1 wk	1 mo	1 yr
198	0.000E+00	8.646E-14	8.646E-14	8.646E-14	8.646E-14	8.646E-14	8.646E-14	8.646E-14
199	0.000E+00	8.436E-17	8.436E-17	8.436E-17	8.436E-17	8.436E-17	8.436E-17	8.436E-17
200	0.000E+00	1.936E-20	1.936E-20	1.936E-20	1.936E-20	1.936E-20	1.936E-20	1.936E-20
201	0.000E+00	8.465E-35	8.465E-35	8.465E-35	8.465E-35	8.465E-35	8.465E-35	8.465E-35
202	0.000E+00	1.005E-38	1.005E-38	1.005E-38	1.005E-38	1.005E-38	1.005E-38	1.005E-38
203	0.000E+00	4.023E-43	4.023E-43	4.021E-43	4.016E-43	4.016E-43	4.016E-43	4.016E-43
204	0.000E+00	0.000E+00	0.000E+00	0.000E+00	0.000E+00	0.000E+00	0.000E+00	0.000E+00
205	0.000E+00	0.000E+00	0.000E+00	0.000E+00	0.000E+00	0.000E+00	0.000E+00	0.000E+00
206	0.000E+00	0.000E+00	8.272E-44	5.256E-39	7.269E-34	1.225E-30	2.377E-28	1.203E-24
207	0.000E+00	4.986E-45	1.312E-36	3.509E-30	1.352E-26	2.762E-23	9.113E-21	1.145E-17
208	0.000E+00	9.707E-44	2.773E-37	2.176E-29	1.273E-24	1.309E-22	1.641E-21	1.613E-19
209	0.000E+00	0.000E+00	3.787E-40	9.540E-32	8.717E-27	2.877E-24	1.447E-22	6.747E-20
210	0.000E+00	7.391E-32	2.065E-28	2.142E-26	2.672E-25	1.651E-24	6.623E-24	3.516E-22
211	0.000E+00	5.996E-38	3.207E-33	1.036E-29	1.549E-27	6.472E-25	4.240E-23	2.748E-21
212	0.000E+00	1.378E-36	4.287E-31	7.088E-27	2.769E-24	2.500E-23	5.980E-23	6.897E-22
213	0.000E+00	1.889E-44	1.227E-37	4.474E-31	1.216E-27	5.435E-26	5.397E-25	1.991E-23
214	0.000E+00	2.262E-34	8.500E-33	1.526E-32	1.954E-29	7.647E-28	6.287E-27	9.224E-26
215	0.000E+00	1.234E-21	4.420E-20	1.166E-18	1.355E-18	1.355E-18	1.355E-18	1.355E-18
216	0.000E+00	1.013E-36	4.336E-33	8.558E-31	1.954E-29	9.384E-29	2.131E-28	2.429E-27
217	0.000E+00	3.276E-45	3.851E-40	2.369E-35	1.661E-32	6.538E-31	6.493E-30	2.395E-28
218	0.000E+00	8.061E-33	3.031E-31	2.363E-31	1.605E-30	5.181E-29	4.250E-28	6.234E-27
219	0.000E+00	2.763E-35	0.000E+00	0.000E+00	0.000E+00	0.000E+00	0.000E+00	0.000E+00
220	0.000E+00	5.916E-34	1.691E-30	3.342E-28	7.631E-27	3.665E-26	8.321E-26	9.489E-25
221	0.000E+00	1.204E-14	5.861E-26	0.000E+00	0.000E+00	0.000E+00	0.000E+00	0.000E+00
222	0.000E+00	8.930E-30	3.187E-28	2.510E-28	2.790E-27	9.363E-26	7.688E-25	1.128E-23

A	Precursor	1 s	1 min	1 h	1 d	1 wk	1 mo	1 yr
223	0.000E+00	3.242E-30	1.946E-28	1.173E-26	7.873E-25	2.948E-22	1.929E-20	1.250E-18
224	0.000E+00	5.517E-28	3.309E-26	1.979E-24	4.418E-23	2.122E-22	4.818E-22	5.495E-21
225	0.000E+00	3.180E-28	1.436E-26	8.571E-25	2.056E-23	1.430E-22	6.240E-22	1.701E-20
226	0.000E+00	2.543E-25	3.528E-24	1.999E-22	4.794E-21	3.356E-20	1.460E-19	1.755E-18
227	0.000E+00	3.078E-21	3.078E-21	4.648E-21	7.459E-19	1.535E-17	8.091E-17	1.005E-15
228	0.000E+00	1.163E-19	1.163E-19	1.174E-19	1.445E-19	3.137E-19	9.742E-19	1.026E-17
229	0.000E+00	8.097E-17	8.097E-17	8.097E-17	8.104E-17	8.449E-17	1.365E-16	2.027E-15
230	0.000E+00	1.938E-13	1.938E-13	1.938E-13	1.938E-13	1.938E-13	1.939E-13	1.949E-13
231	0.000E+00	4.919E-11	4.919E-11	4.919E-11	4.919E-11	4.919E-11	4.919E-11	4.918E-11
232	2.009E-07	2.000E-07	2.000E-07	2.000E-07	2.000E-07	2.000E-07	2.000E-07	2.000E-07
233	0.000E+00	5.090E-10	5.090E-10	5.090E-10	5.090E-10	5.090E-10	5.090E-10	5.090E-10
234	2.080E-12	3.842E-10	3.842E-10	3.842E-10	3.842E-10	3.842E-10	3.843E-10	3.844E-10
235	2.775E-10	4.999E-08	4.999E-08	4.999E-08	4.999E-08	4.999E-08	4.999E-08	5.001E-08
236	0.000E+00	1.372E-10	1.372E-10	1.372E-10	1.372E-10	1.373E-10	1.376E-10	1.413E-10
237	0.000E+00	1.651E-09	1.651E-09	1.651E-09	1.651E-09	1.651E-09	1.651E-09	1.651E-09
238	3.824E-08	7.062E-06	7.062E-06	7.062E-06	7.062E-06	7.062E-06	7.062E-06	7.062E-06
239	0.000E+00	5.199E-07	5.199E-07	5.199E-07	5.199E-07	5.199E-07	5.199E-07	5.199E-07
240	0.000E+00	3.961E-08	3.961E-08	3.961E-08	3.961E-08	3.961E-08	3.961E-08	3.961E-08
241	0.000E+00	8.568E-11	8.568E-11	8.568E-11	8.568E-11	8.568E-11	8.568E-11	8.567E-11
242	0.000E+00	3.169E-13	3.169E-13	3.169E-13	3.169E-13	3.169E-13	3.169E-13	3.169E-13
243	0.000E+00	2.583E-16	2.583E-16	2.583E-16	2.583E-16	2.583E-16	2.583E-16	2.583E-16
244	0.000E+00	2.150E-30	2.150E-30	2.150E-30	2.150E-30	2.148E-30	2.143E-30	2.069E-30
245	0.000E+00	9.363E-44	9.363E-44	9.363E-44	9.363E-44	9.363E-44	9.363E-44	9.362E-44

AV.2 WGPu IND Mass Fraction Results by Atomic Number (Z) and Time

Z	Precursor	1 s	1 min	1 h	1 d	1 wk	1 mo	1 yr
1	1.902E-02	1.903E-02	1.903E-02	1.903E-02	1.903E-02	1.903E-02	1.903E-02	1.903E-02
2	0.000E+00	3.731E-05	3.731E-05	3.731E-05	3.731E-05	3.731E-05	3.731E-05	3.731E-05
3	0.000E+00	2.439E-12	2.474E-12	2.474E-12	2.474E-12	2.474E-12	2.474E-12	2.474E-12
4	0.000E+00	1.855E-09	1.855E-09	1.855E-09	1.855E-09	1.855E-09	1.855E-09	1.855E-09
5	0.000E+00	9.772E-08	9.772E-08	9.772E-08	9.772E-08	9.772E-08	9.772E-08	9.772E-08
6	0.000E+00	1.392E-04	1.392E-04	1.392E-04	1.392E-04	1.392E-04	1.392E-04	1.392E-04
7	0.000E+00	6.503E-05	6.489E-05	6.489E-05	6.489E-05	6.489E-05	6.489E-05	6.489E-05
8	5.607E-01	5.605E-01	5.605E-01	5.605E-01	5.605E-01	5.605E-01	5.605E-01	5.605E-01
9	0.000E+00	1.633E-07	6.192E-09	2.454E-09	2.454E-09	2.454E-09	2.454E-09	2.454E-09
10	0.000E+00	6.174E-07	4.153E-07	2.389E-07	2.389E-07	2.389E-07	2.389E-07	2.391E-07
11	2.055E-02	2.054E-02	2.054E-02	2.054E-02	2.054E-02	2.054E-02	2.054E-02	2.054E-02
12	6.050E-04	6.219E-04	6.215E-04	6.165E-04	6.169E-04	6.172E-04	6.172E-04	6.172E-04
13	6.379E-02	6.381E-02	6.381E-02	6.379E-02	6.379E-02	6.379E-02	6.379E-02	6.379E-02
14	2.935E-01	2.934E-01	2.934E-01	2.934E-01	2.934E-01	2.934E-01	2.934E-01	2.934E-01
15	6.200E-05	6.192E-05	6.193E-05	6.198E-05	6.214E-05	6.214E-05	6.214E-05	6.214E-05
16	0.000E+00	1.661E-08	1.661E-08	1.662E-08	1.673E-08	1.734E-08	1.861E-08	1.928E-08
17	0.000E+00	6.462E-06	6.462E-06	6.453E-06	6.497E-06	6.784E-06	7.629E-06	9.059E-06
18	0.000E+00	1.944E-04	1.944E-04	1.944E-04	1.943E-04	1.940E-04	1.931E-04	1.913E-04
19	3.135E-02	3.116E-02	3.116E-02	3.116E-02	3.116E-02	3.116E-02	3.116E-02	3.116E-02
20	2.710E-03	2.701E-03	2.701E-03	2.701E-03	2.701E-03	2.701E-03	2.701E-03	2.701E-03
21	1.852E-08	7.032E-08	7.031E-08	6.985E-08	6.296E-08	4.205E-08	3.208E-08	2.255E-08
22	9.826E-04	9.824E-04	9.824E-04	9.823E-04	9.824E-04	9.824E-04	9.824E-04	9.824E-04

Z	Precursor	1 s	1 min	1 h	1 d	1 wk	1 mo	1 yr
23	0.000E+00	7.827E-10	7.275E-10	6.713E-10	7.822E-10	1.417E-09	3.155E-09	5.334E-09
24	0.000E+00	3.939E-08	3.844E-08	3.415E-08	3.531E-08	4.255E-08	7.060E-08	3.609E-07
25	5.765E-04	5.772E-04	5.772E-04	5.771E-04	5.770E-04	5.770E-04	5.770E-04	5.767E-04
26	6.176E-03	6.174E-03	6.174E-03	6.174E-03	6.174E-03	6.174E-03	6.174E-03	6.174E-03
27	2.960E-09	2.962E-09	2.962E-09	2.963E-09	2.982E-09	3.093E-09	3.438E-09	4.218E-09
28	0.000E+00	2.135E-10	2.136E-10	2.224E-10	3.371E-10	3.833E-10	3.833E-10	3.826E-10
29	0.000E+00	4.285E-07	4.285E-07	4.285E-07	4.283E-07	4.282E-07	4.282E-07	4.283E-07
30	4.729E-07	4.725E-07	4.725E-07	4.726E-07	4.726E-07	4.727E-07	4.727E-07	4.726E-07
31	0.000E+00	1.332E-11	1.107E-12	4.676E-12	9.311E-12	9.659E-12	9.657E-12	9.657E-12
32	0.000E+00	8.954E-11	1.393E-11	6.632E-12	1.942E-12	1.544E-12	1.569E-12	1.580E-12
33	1.700E-08	1.726E-08	1.703E-08	1.700E-08	1.699E-08	1.698E-08	1.698E-08	1.698E-08
34	0.000E+00	7.250E-10	4.171E-10	1.156E-10	1.064E-10	1.159E-10	1.162E-10	1.162E-10
35	0.000E+00	1.187E-09	5.627E-10	1.662E-10	3.251E-11	3.232E-11	3.231E-11	3.231E-11
36	0.000E+00	2.379E-09	1.704E-09	1.366E-09	7.257E-10	7.205E-10	7.209E-10	7.181E-10
37	1.413E-06	1.415E-06	1.413E-06	1.412E-06	1.413E-06	1.413E-06	1.412E-06	1.412E-06
38	4.618E-07	4.654E-07	4.657E-07	4.652E-07	4.640E-07	4.640E-07	4.641E-07	4.639E-07
39	2.640E-07	2.680E-07	2.659E-07	2.658E-07	2.651E-07	2.649E-07	2.649E-07	2.647E-07
40	1.691E-06	1.697E-06	1.695E-06	1.697E-06	1.698E-06	1.698E-06	1.698E-06	1.697E-06
41	2.080E-07	2.121E-07	2.087E-07	2.080E-07	2.081E-07	2.081E-07	2.083E-07	2.080E-07
42	1.269E-08	1.722E-08	2.388E-08	1.881E-08	1.926E-08	1.877E-08	1.854E-08	1.996E-08
43	0.000E+00	1.122E-09	3.132E-09	5.564E-10	4.380E-10	1.630E-09	1.966E-09	1.967E-09
44	0.000E+00	6.389E-10	2.091E-09	9.786E-09	9.171E-09	8.915E-09	8.239E-09	6.548E-09
45	0.000E+00	1.302E-10	2.444E-10	3.044E-10	1.073E-09	3.091E-10	8.762E-10	2.104E-09
46	0.000E+00	1.122E-10	3.461E-10	1.352E-09	1.735E-09	2.671E-09	2.779E-09	3.241E-09
47	0.000E+00	6.467E-11	8.659E-11	1.057E-10	2.184E-10	2.425E-10	2.065E-10	2.020E-10

Z	Precursor	1 s	1 min	1 h	1 d	1 wk	1 mo	1 yr
48	0.000E+00	1.189E-10	1.035E-10	1.559E-10	1.700E-10	2.095E-10	2.412E-10	2.445E-10
49	0.000E+00	1.807E-10	3.568E-11	8.477E-12	8.794E-12	2.900E-11	3.325E-11	3.456E-11
50	0.000E+00	2.872E-09	1.999E-09	4.836E-10	3.400E-10	3.176E-10	3.076E-10	3.030E-10
51	4.526E-09	8.406E-09	8.199E-09	5.510E-09	4.752E-09	4.680E-09	4.648E-09	4.638E-09
52	0.000E+00	7.475E-09	5.702E-09	5.359E-09	3.128E-09	1.732E-09	1.222E-09	1.173E-09
53	0.000E+00	6.239E-09	5.331E-09	6.912E-09	3.337E-09	1.376E-09	6.908E-10	6.404E-10
54	0.000E+00	7.092E-09	6.905E-09	4.662E-09	9.210E-09	1.012E-08	1.000E-08	1.006E-08
55	4.229E-08	4.704E-08	4.657E-08	4.615E-08	4.715E-08	4.969E-08	5.104E-08	5.103E-08
56	1.954E-06	1.960E-06	1.959E-06	1.960E-06	1.959E-06	1.958E-06	1.957E-06	1.957E-06
57	7.061E-07	7.089E-07	7.093E-07	7.103E-07	7.087E-07	7.087E-07	7.085E-07	7.085E-07
58	1.486E-06	1.488E-06	1.490E-06	1.490E-06	1.493E-06	1.492E-06	1.493E-06	1.491E-06
59	0.000E+00	8.788E-10	1.800E-09	2.020E-09	9.631E-10	1.944E-09	1.717E-09	2.551E-09
60	2.157E-07	2.161E-07	2.172E-07	2.199E-07	2.213E-07	2.215E-07	2.222E-07	2.236E-07
61	0.000E+00	1.206E-10	2.902E-10	6.124E-10	8.474E-10	5.059E-10	9.813E-10	9.069E-10
62	4.103E-08	4.107E-08	4.119E-08	4.166E-08	4.190E-08	4.243E-08	4.251E-08	4.276E-08
63	2.397E-09	2.406E-09	2.416E-09	2.525E-09	2.612E-09	2.741E-09	2.734E-09	2.710E-09
64	0.000E+00	2.603E-12	6.446E-12	2.411E-11	5.198E-11	7.174E-11	9.815E-11	1.242E-10
65	5.370E-09	5.370E-09	5.370E-09	5.372E-09	5.377E-09	5.379E-09	5.373E-09	5.356E-09
66	0.000E+00	1.105E-13	3.308E-13	2.570E-12	2.930E-12	5.027E-12	1.038E-11	2.731E-11
67	0.000E+00	9.456E-15	2.624E-14	1.104E-13	2.255E-13	2.217E-13	2.062E-13	2.060E-13
68	0.000E+00	1.028E-15	8.384E-15	6.997E-14	1.297E-13	2.069E-13	2.486E-13	2.475E-13
69	0.000E+00	7.205E-16	7.466E-16	1.735E-15	8.485E-15	2.574E-14	6.596E-14	1.188E-13
70	2.195E-08	2.194E-08	2.194E-08	2.194E-08	2.194E-08	2.194E-08	2.194E-08	2.194E-08
71	3.299E-09	3.299E-09	3.299E-09	3.297E-09	3.291E-09	3.293E-09	3.295E-09	3.295E-09
72	4.441E-08	4.440E-08	4.440E-08	4.440E-08	4.441E-08	4.440E-08	4.440E-08	4.439E-08

Z	Precursor	1 s	1 min	1 h	1 d	1 wk	1 mo	1 yr
73	1.210E-08	1.209E-08	1.209E-08	1.209E-08	1.209E-08	1.209E-08	1.209E-08	1.207E-08
74	1.353E-08	1.353E-08	1.353E-08	1.353E-08	1.353E-08	1.353E-08	1.353E-08	1.355E-08
75	0.000E+00	3.178E-17	1.907E-15	1.129E-13	1.993E-12	4.153E-12	4.994E-12	8.196E-12
76	0.000E+00	3.366E-27	1.200E-24	3.569E-21	1.356E-18	2.166E-17	9.515E-17	3.655E-16
77	0.000E+00	1.217E-19	1.216E-19	1.174E-19	5.149E-20	5.235E-22	2.341E-22	2.341E-22
78	0.000E+00	4.512E-18	4.632E-18	1.176E-17	1.690E-16	8.552E-16	1.519E-15	1.571E-15
79	4.060E-11	4.060E-11	4.060E-11	4.059E-11	4.058E-11	4.052E-11	4.051E-11	4.051E-11
80	0.000E+00	2.575E-19	1.545E-17	9.219E-16	1.962E-14	7.228E-14	8.662E-14	8.666E-14
81	0.000E+00	4.986E-45	1.370E-36	2.794E-30	4.144E-27	1.180E-25	5.268E-24	3.364E-22
82	0.000E+00	7.391E-32	2.069E-28	2.842E-26	4.103E-24	1.837E-22	1.085E-20	1.162E-17
83	0.000E+00	3.375E-41	1.427E-34	1.285E-28	2.264E-25	4.953E-24	1.506E-22	6.762E-20
84	0.000E+00	2.272E-34	1.284E-32	8.648E-31	2.160E-29	2.804E-28	6.080E-27	2.402E-24
85	0.000E+00	3.276E-45	3.852E-40	2.370E-35	1.661E-32	6.539E-31	6.493E-30	2.396E-28
86	0.000E+00	8.657E-33	1.996E-30	3.393E-28	1.027E-26	1.313E-25	9.279E-25	1.715E-23
87	0.000E+00	5.747E-36	2.049E-32	4.808E-29	1.884E-26	4.058E-25	2.166E-24	2.833E-23
88	0.000E+00	7.047E-20	7.044E-20	6.985E-20	9.878E-20	2.870E-19	1.037E-18	1.222E-17
89	0.000E+00	8.411E-25	5.047E-23	3.495E-21	7.459E-19	1.535E-17	8.083E-17	1.002E-15
90	2.009E-07	2.005E-07	2.005E-07	2.001E-07	2.000E-07	2.000E-07	2.000E-07	2.000E-07
91	0.000E+00	2.650E-13	1.560E-11	4.312E-10	5.199E-10	4.741E-10	2.822E-10	4.923E-11
92	3.520E-08	7.128E-06	7.127E-06	7.116E-06	7.114E-06	7.113E-06	7.113E-06	7.113E-06
93	0.000E+00	6.681E-12	3.944E-10	1.116E-08	1.032E-08	2.585E-09	1.580E-09	1.651E-09
94	0.000E+00	5.460E-07	5.460E-07	5.461E-07	5.494E-07	5.579E-07	5.596E-07	5.596E-07
95	0.000E+00	1.417E-19	8.501E-18	5.078E-16	1.163E-14	7.986E-14	3.459E-13	4.054E-12
96	0.000E+00	2.402E-33	1.434E-31	6.963E-30	8.414E-29	1.261E-28	1.145E-28	2.918E-29
97	0.000E+00	0.000E+00	0.000E+00	0.000E+00	0.000E+00	0.000E+00	0.000E+00	0.000E+00

Z	Precursor	1 s	1 min	1 h	1 d	1 wk	1 mo	1 yr
98	0.000E+00	0.000E+00	0.000E+00	0.000E+00	0.000E+00	0.000E+00	0.000E+00	0.000E+00
99	0.000E+00	0.000E+00	0.000E+00	0.000E+00	0.000E+00	0.000E+00	0.000E+00	0.000E+00

AV.3 WGU IND Mass Fraction Results by Mass Number (A) and Time

A	Precursor	1 s	1 min	1 h	1 d	1 wk	1 mo	1 yr
1	1.902E-02	1.903E-02	1.903E-02	1.903E-02	1.903E-02	1.903E-02	1.903E-02	1.903E-02
2	2.187E-06	4.014E-08	4.014E-08	4.014E-08	4.014E-08	4.014E-08	4.014E-08	4.014E-08
3	0.000E+00	1.769E-09	1.769E-09	1.769E-09	1.769E-09	1.769E-09	1.769E-09	1.769E-09
4	0.000E+00	2.913E-05	2.913E-05	2.913E-05	2.913E-05	2.913E-05	2.913E-05	2.913E-05
5	0.000E+00	0.000E+00	0.000E+00	0.000E+00	0.000E+00	0.000E+00	0.000E+00	0.000E+00
6	0.000E+00	6.612E-14	6.612E-14	6.612E-14	6.612E-14	6.612E-14	6.612E-14	6.612E-14
7	0.000E+00	1.847E-12	1.847E-12	1.847E-12	1.847E-12	1.847E-12	1.847E-12	1.847E-12
8	0.000E+00	6.593E-15	4.215E-36	0.000E+00	0.000E+00	0.000E+00	0.000E+00	0.000E+00
9	0.000E+00	3.123E-10	3.123E-10	3.123E-10	3.123E-10	3.123E-10	3.123E-10	3.123E-10
10	0.000E+00	8.880E-10	8.880E-10	8.880E-10	8.880E-10	8.880E-10	8.880E-10	8.880E-10
11	0.000E+00	7.632E-08	7.632E-08	7.632E-08	7.632E-08	7.632E-08	7.632E-08	7.632E-08
12	0.000E+00	2.831E-05	2.831E-05	2.831E-05	2.831E-05	2.831E-05	2.831E-05	2.831E-05
13	0.000E+00	8.625E-05	8.625E-05	8.625E-05	8.625E-05	8.625E-05	8.625E-05	8.625E-05
14	0.000E+00	6.487E-05	6.487E-05	6.487E-05	6.487E-05	6.487E-05	6.487E-05	6.487E-05
15	0.000E+00	2.760E-07	2.760E-07	2.760E-07	2.760E-07	2.760E-07	2.760E-07	2.760E-07
16	5.593E-01	5.590E-01	5.590E-01	5.590E-01	5.590E-01	5.590E-01	5.590E-01	5.590E-01
17	2.131E-04	2.270E-04	2.270E-04	2.270E-04	2.270E-04	2.270E-04	2.270E-04	2.270E-04
18	1.149E-03	1.261E-03	1.261E-03	1.261E-03	1.261E-03	1.261E-03	1.261E-03	1.261E-03
19	0.000E+00	1.916E-09	1.916E-09	1.916E-09	1.916E-09	1.916E-09	1.916E-09	1.916E-09
20	0.000E+00	1.354E-07	1.354E-07	1.354E-07	1.354E-07	1.354E-07	1.354E-07	1.354E-07
21	0.000E+00	2.144E-08	2.144E-08	2.144E-08	2.144E-08	2.144E-08	2.144E-08	2.144E-08
22	0.000E+00	3.010E-08	3.010E-08	3.010E-08	3.010E-08	3.010E-08	3.010E-08	3.010E-08
23	2.055E-02	2.054E-02	2.054E-02	2.054E-02	2.054E-02	2.054E-02	2.054E-02	2.054E-02

A	Precursor	1 s	1 min	1 h	1 d	1 wk	1 mo	1 yr
24	4.779E-04	4.722E-04	4.722E-04	4.722E-04	4.722E-04	4.722E-04	4.722E-04	4.722E-04
25	6.050E-05	6.995E-05	6.995E-05	6.995E-05	6.995E-05	6.995E-05	6.995E-05	6.995E-05
26	6.661E-05	7.238E-05	7.238E-05	7.238E-05	7.238E-05	7.238E-05	7.238E-05	7.238E-05
27	6.379E-02	6.379E-02	6.379E-02	6.379E-02	6.379E-02	6.379E-02	6.379E-02	6.379E-02
28	2.707E-01	2.696E-01	2.696E-01	2.696E-01	2.696E-01	2.696E-01	2.696E-01	2.696E-01
29	1.375E-02	1.418E-02	1.418E-02	1.418E-02	1.418E-02	1.418E-02	1.418E-02	1.418E-02
30	9.075E-03	9.667E-03	9.667E-03	9.667E-03	9.667E-03	9.667E-03	9.667E-03	9.667E-03
31	6.198E-05	6.210E-05	6.210E-05	6.210E-05	6.210E-05	6.210E-05	6.210E-05	6.210E-05
32	0.000E+00	1.683E-09	1.683E-09	1.683E-09	1.683E-09	1.683E-09	1.683E-09	1.683E-09
33	0.000E+00	4.083E-10	4.083E-10	4.083E-10	4.083E-10	4.083E-10	4.083E-10	4.083E-10
34	0.000E+00	5.691E-09	5.691E-09	5.691E-09	5.691E-09	5.691E-09	5.691E-09	5.691E-09
35	0.000E+00	2.211E-09	2.211E-09	2.211E-09	2.211E-09	2.211E-09	2.211E-09	2.211E-09
36	0.000E+00	5.008E-06	5.008E-06	5.008E-06	5.008E-06	5.008E-06	5.008E-06	5.008E-06
37	0.000E+00	2.075E-06	2.075E-06	2.075E-06	2.075E-06	2.075E-06	2.075E-06	2.075E-06
38	0.000E+00	1.750E-07	1.750E-07	1.750E-07	1.750E-07	1.750E-07	1.750E-07	1.750E-07
39	2.924E-02	2.913E-02	2.913E-02	2.913E-02	2.913E-02	2.913E-02	2.913E-02	2.913E-02
40	2.631E-03	2.622E-03	2.622E-03	2.622E-03	2.622E-03	2.622E-03	2.622E-03	2.622E-03
41	2.110E-03	2.210E-03	2.210E-03	2.210E-03	2.210E-03	2.210E-03	2.210E-03	2.210E-03
42	1.754E-05	1.864E-05	1.864E-05	1.864E-05	1.864E-05	1.864E-05	1.864E-05	1.864E-05
43	3.659E-06	3.922E-06	3.922E-06	3.922E-06	3.922E-06	3.922E-06	3.922E-06	3.922E-06
44	5.654E-05	6.211E-05	6.211E-05	6.211E-05	6.211E-05	6.211E-05	6.211E-05	6.211E-05
45	1.852E-08	2.170E-08	2.170E-08	2.169E-08	2.170E-08	2.169E-08	2.170E-08	2.169E-08
46	8.118E-05	7.792E-05	7.792E-05	7.792E-05	7.792E-05	7.792E-05	7.792E-05	7.792E-05
47	7.311E-05	7.169E-05	7.169E-05	7.169E-05	7.169E-05	7.169E-05	7.169E-05	7.169E-05
48	7.295E-04	7.315E-04	7.315E-04	7.315E-04	7.315E-04	7.315E-04	7.315E-04	7.315E-04

A	Precursor	1 s	1 min	1 h	1 d	1 wk	1 mo	1 yr
49	5.316E-05	5.438E-05	5.438E-05	5.438E-05	5.438E-05	5.438E-05	5.438E-05	5.438E-05
50	5.090E-05	5.310E-05	5.310E-05	5.310E-05	5.310E-05	5.310E-05	5.310E-05	5.310E-05
51	0.000E+00	4.166E-09	4.166E-09	4.166E-09	4.166E-09	4.166E-09	4.166E-09	4.166E-09
52	0.000E+00	6.209E-10	6.209E-10	6.209E-10	6.209E-10	6.209E-10	6.209E-10	6.209E-10
53	0.000E+00	2.014E-08	2.014E-08	2.014E-08	2.014E-08	2.014E-08	2.014E-08	2.014E-08
54	3.610E-04	3.486E-04	3.486E-04	3.486E-04	3.486E-04	3.486E-04	3.486E-04	3.486E-04
55	5.765E-04	5.765E-04	5.765E-04	5.765E-04	5.765E-04	5.765E-04	5.765E-04	5.765E-04
56	5.667E-03	5.675E-03	5.675E-03	5.675E-03	5.675E-03	5.675E-03	5.675E-03	5.675E-03
57	1.309E-04	1.338E-04	1.338E-04	1.338E-04	1.338E-04	1.338E-04	1.338E-04	1.338E-04
58	1.742E-05	1.807E-05	1.807E-05	1.807E-05	1.807E-05	1.807E-05	1.807E-05	1.807E-05
59	2.960E-09	3.944E-09	3.944E-09	3.944E-09	3.944E-09	3.944E-09	3.944E-09	3.944E-09
60	0.000E+00	2.545E-12	2.545E-12	2.545E-12	2.544E-12	2.545E-12	2.545E-12	2.544E-12
61	0.000E+00	4.452E-11	4.452E-11	4.452E-11	4.452E-11	4.452E-11	4.452E-11	4.452E-11
62	0.000E+00	2.243E-12	2.243E-12	2.243E-12	2.243E-12	2.243E-12	2.243E-12	2.243E-12
63	0.000E+00	2.934E-07	2.934E-07	2.934E-07	2.934E-07	2.934E-07	2.934E-07	2.934E-07
64	2.325E-07	2.247E-07	2.247E-07	2.247E-07	2.247E-07	2.247E-07	2.247E-07	2.247E-07
65	0.000E+00	1.350E-07	1.350E-07	1.350E-07	1.350E-07	1.350E-07	1.350E-07	1.350E-07
66	1.311E-07	1.330E-07	1.330E-07	1.330E-07	1.330E-07	1.330E-07	1.330E-07	1.330E-07
67	1.910E-08	1.985E-08	1.985E-08	1.985E-08	1.985E-08	1.985E-08	1.985E-08	1.985E-08
68	8.725E-08	9.208E-08	9.208E-08	9.208E-08	9.208E-08	9.208E-08	9.208E-08	9.208E-08
69	0.000E+00	7.400E-12	7.400E-12	7.400E-12	7.400E-12	7.400E-12	7.400E-12	7.400E-12
70	2.885E-09	3.134E-09	3.134E-09	3.134E-09	3.134E-09	3.134E-09	3.134E-09	3.134E-09
71	0.000E+00	1.341E-13	1.341E-13	1.341E-13	1.341E-13	1.341E-13	1.341E-13	1.341E-13
72	0.000E+00	6.808E-14	6.815E-14	6.815E-14	6.815E-14	6.815E-14	6.815E-14	6.815E-14
73	0.000E+00	1.409E-13	1.409E-13	1.409E-13	1.409E-13	1.409E-13	1.409E-13	1.409E-13

A	Precursor	1 s	1 min	1 h	1 d	1 wk	1 mo	1 yr
74	0.000E+00	3.264E-13	3.285E-13	3.285E-13	3.285E-13	3.285E-13	3.285E-13	3.285E-13
75	1.700E-08	1.699E-08	1.699E-08	1.699E-08	1.699E-08	1.699E-08	1.699E-08	1.699E-08
76	0.000E+00	1.437E-11	1.437E-11	1.437E-11	1.437E-11	1.437E-11	1.437E-11	1.437E-11
77	0.000E+00	4.698E-12	4.697E-12	4.697E-12	4.697E-12	4.697E-12	4.697E-12	4.697E-12
78	0.000E+00	9.266E-12	9.276E-12	9.277E-12	9.277E-12	9.277E-12	9.277E-12	9.277E-12
79	0.000E+00	1.737E-11	1.740E-11	1.739E-11	1.740E-11	1.740E-11	1.740E-11	1.740E-11
80	0.000E+00	3.131E-11	3.152E-11	3.152E-11	3.152E-11	3.152E-11	3.152E-11	3.152E-11
81	0.000E+00	4.652E-11	4.634E-11	4.634E-11	4.634E-11	4.634E-11	4.634E-11	4.634E-11
82	0.000E+00	8.152E-11	8.152E-11	8.152E-11	8.152E-11	8.152E-11	8.152E-11	8.152E-11
83	0.000E+00	1.425E-10	1.434E-10	1.434E-10	1.434E-10	1.434E-10	1.434E-10	1.434E-10
84	2.586E-09	2.719E-09	2.755E-09	2.755E-09	2.755E-09	2.755E-09	2.755E-09	2.755E-09
85	1.019E-06	1.012E-06	1.012E-06	1.012E-06	1.012E-06	1.012E-06	1.012E-06	1.012E-06
86	4.553E-08	4.570E-08	4.570E-08	4.571E-08	4.571E-08	4.571E-08	4.571E-08	4.571E-08
87	4.254E-07	4.323E-07	4.323E-07	4.323E-07	4.323E-07	4.323E-07	4.323E-07	4.323E-07
88	3.813E-07	3.834E-07	3.834E-07	3.834E-07	3.834E-07	3.834E-07	3.834E-07	3.834E-07
89	2.640E-07	2.650E-07	2.650E-07	2.650E-07	2.650E-07	2.650E-07	2.650E-07	2.650E-07
90	8.699E-07	8.585E-07	8.584E-07	8.584E-07	8.584E-07	8.585E-07	8.585E-07	8.584E-07
91	1.897E-07	1.906E-07	1.906E-07	1.906E-07	1.906E-07	1.906E-07	1.906E-07	1.906E-07
92	2.918E-07	2.954E-07	2.955E-07	2.955E-07	2.955E-07	2.955E-07	2.955E-07	2.955E-07
93	2.080E-07	2.097E-07	2.097E-07	2.097E-07	2.097E-07	2.097E-07	2.097E-07	2.097E-07
94	2.950E-07	3.055E-07	3.054E-07	3.054E-07	3.054E-07	3.054E-07	3.054E-07	3.054E-07
95	2.010E-09	3.921E-09	3.916E-09	3.916E-09	3.916E-09	3.916E-09	3.916E-09	3.916E-09
96	4.946E-08	5.386E-08	5.386E-08	5.386E-08	5.386E-08	5.386E-08	5.386E-08	5.386E-08
97	1.218E-09	3.155E-09	3.157E-09	3.157E-09	3.157E-09	3.156E-09	3.156E-09	3.156E-09
98	3.094E-09	5.085E-09	5.095E-09	5.095E-09	5.095E-09	5.095E-09	5.095E-09	5.095E-09

A	Precursor	1 s	1 min	1 h	1 d	1 wk	1 mo	1 yr
99	0.000E+00	2.060E-09	2.050E-09	2.050E-09	2.050E-09	2.050E-09	2.050E-09	2.050E-09
100	1.246E-09	3.471E-09	3.470E-09	3.470E-09	3.470E-09	3.470E-09	3.470E-09	3.470E-09
101	0.000E+00	1.946E-09	1.945E-09	1.945E-09	1.945E-09	1.945E-09	1.945E-09	1.945E-09
102	0.000E+00	1.849E-09	1.849E-09	1.849E-09	1.849E-09	1.849E-09	1.849E-09	1.849E-09
103	0.000E+00	1.642E-09	1.642E-09	1.642E-09	1.642E-09	1.642E-09	1.642E-09	1.642E-09
104	0.000E+00	1.235E-09	1.240E-09	1.240E-09	1.240E-09	1.240E-09	1.240E-09	1.240E-09
105	0.000E+00	9.323E-10	9.293E-10	9.293E-10	9.293E-10	9.294E-10	9.293E-10	9.293E-10
106	0.000E+00	5.431E-10	5.408E-10	5.408E-10	5.408E-10	5.408E-10	5.408E-10	5.408E-10
107	0.000E+00	3.189E-10	3.187E-10	3.187E-10	3.187E-10	3.187E-10	3.187E-10	3.187E-10
108	0.000E+00	1.432E-10	1.432E-10	1.432E-10	1.432E-10	1.432E-10	1.432E-10	1.432E-10
109	0.000E+00	7.464E-11	7.460E-11	7.460E-11	7.461E-11	7.461E-11	7.461E-11	7.461E-11
110	0.000E+00	5.256E-11	5.257E-11	5.257E-11	5.257E-11	5.257E-11	5.257E-11	5.257E-11
111	0.000E+00	3.589E-11	3.588E-11	3.588E-11	3.588E-11	3.588E-11	3.588E-11	3.588E-11
112	0.000E+00	3.332E-11	3.331E-11	3.331E-11	3.331E-11	3.331E-11	3.331E-11	3.331E-11
113	0.000E+00	2.915E-11	2.915E-11	2.915E-11	2.915E-11	2.915E-11	2.915E-11	2.915E-11
114	0.000E+00	2.486E-11	2.486E-11	2.486E-11	2.486E-11	2.486E-11	2.486E-11	2.486E-11
115	0.000E+00	2.737E-11	2.737E-11	2.737E-11	2.737E-11	2.737E-11	2.737E-11	2.737E-11
116	0.000E+00	2.497E-11	2.497E-11	2.497E-11	2.497E-11	2.497E-11	2.497E-11	2.497E-11
117	0.000E+00	2.429E-11	2.429E-11	2.429E-11	2.429E-11	2.429E-11	2.429E-11	2.429E-11
118	0.000E+00	2.854E-11	2.854E-11	2.854E-11	2.854E-11	2.854E-11	2.854E-11	2.854E-11
119	0.000E+00	2.662E-11	2.662E-11	2.662E-11	2.662E-11	2.662E-11	2.662E-11	2.662E-11
120	0.000E+00	2.765E-11	2.765E-11	2.765E-11	2.765E-11	2.765E-11	2.765E-11	2.765E-11
121	2.590E-09	2.594E-09	2.594E-09	2.594E-09	2.594E-09	2.594E-09	2.594E-09	2.594E-09
122	0.000E+00	3.656E-11	3.656E-11	3.656E-11	3.656E-11	3.656E-11	3.656E-11	3.656E-11
123	1.937E-09	1.986E-09	1.986E-09	1.986E-09	1.986E-09	1.986E-09	1.986E-09	1.986E-09

A	Precursor	1 s	1 min	1 h	1 d	1 wk	1 mo	1 yr
124	0.000E+00	4.221E-11	4.221E-11	4.221E-11	4.221E-11	4.221E-11	4.221E-11	4.221E-11
125	0.000E+00	4.489E-11	4.489E-11	4.489E-11	4.489E-11	4.489E-11	4.489E-11	4.489E-11
126	0.000E+00	5.488E-11	5.499E-11	5.499E-11	5.499E-11	5.499E-11	5.499E-11	5.499E-11
127	0.000E+00	1.183E-10	1.182E-10	1.182E-10	1.182E-10	1.182E-10	1.182E-10	1.182E-10
128	0.000E+00	2.004E-10	2.007E-10	2.007E-10	2.007E-10	2.007E-10	2.007E-10	2.007E-10
129	0.000E+00	4.215E-10	4.214E-10	4.214E-10	4.214E-10	4.214E-10	4.214E-10	4.214E-10
130	2.072E-09	2.801E-09	2.801E-09	2.801E-09	2.801E-09	2.801E-09	2.801E-09	2.801E-09
131	0.000E+00	1.469E-09	1.469E-09	1.469E-09	1.469E-09	1.469E-09	1.469E-09	1.469E-09
132	1.974E-09	4.089E-09	4.089E-09	4.089E-09	4.089E-09	4.089E-09	4.089E-09	4.089E-09
133	4.229E-08	4.529E-08	4.530E-08	4.530E-08	4.530E-08	4.530E-08	4.530E-08	4.530E-08
134	4.723E-08	4.951E-08	4.954E-08	4.954E-08	4.954E-08	4.954E-08	4.954E-08	4.954E-08
135	1.288E-07	1.296E-07	1.296E-07	1.296E-07	1.296E-07	1.296E-07	1.296E-07	1.296E-07
136	1.562E-07	1.576E-07	1.576E-07	1.577E-07	1.577E-07	1.577E-07	1.577E-07	1.577E-07
137	2.195E-07	2.217E-07	2.217E-07	2.217E-07	2.217E-07	2.217E-07	2.217E-07	2.217E-07
138	1.406E-06	1.414E-06	1.414E-06	1.414E-06	1.414E-06	1.414E-06	1.414E-06	1.414E-06
139	7.054E-07	7.081E-07	7.081E-07	7.081E-07	7.081E-07	7.081E-07	7.081E-07	7.081E-07
140	1.314E-06	1.315E-06	1.315E-06	1.315E-06	1.315E-06	1.315E-06	1.315E-06	1.315E-06
141	0.000E+00	2.814E-09	2.813E-09	2.812E-09	2.812E-09	2.812E-09	2.812E-09	2.812E-09
142	2.237E-07	2.273E-07	2.273E-07	2.273E-07	2.273E-07	2.273E-07	2.273E-07	2.273E-07
143	2.626E-08	2.863E-08	2.863E-08	2.863E-08	2.863E-08	2.863E-08	2.863E-08	2.863E-08
144	5.259E-08	5.483E-08	5.483E-08	5.483E-08	5.483E-08	5.483E-08	5.483E-08	5.483E-08
145	1.789E-08	1.987E-08	1.986E-08	1.986E-08	1.986E-08	1.986E-08	1.986E-08	1.986E-08
146	3.708E-08	3.910E-08	3.910E-08	3.910E-08	3.910E-08	3.910E-08	3.910E-08	3.910E-08
147	6.150E-09	7.187E-09	7.187E-09	7.187E-09	7.187E-09	7.187E-09	7.187E-09	7.187E-09
148	1.703E-08	1.809E-08	1.809E-08	1.809E-08	1.809E-08	1.809E-08	1.809E-08	1.809E-08

A	Precursor	1 s	1 min	1 h	1 d	1 wk	1 mo	1 yr
149	5.670E-09	6.284E-09	6.283E-09	6.283E-09	6.283E-09	6.283E-09	6.283E-09	6.283E-09
150	1.519E-08	1.608E-08	1.608E-08	1.608E-08	1.608E-08	1.608E-08	1.608E-08	1.608E-08
151	1.146E-09	1.457E-09	1.456E-09	1.456E-09	1.456E-09	1.456E-09	1.456E-09	1.456E-09
152	1.097E-08	1.128E-08	1.128E-08	1.128E-08	1.128E-08	1.128E-08	1.128E-08	1.128E-08
153	1.251E-09	1.424E-09	1.424E-09	1.424E-09	1.424E-09	1.424E-09	1.424E-09	1.424E-09
154	9.334E-09	9.624E-09	9.623E-09	9.624E-09	9.624E-09	9.624E-09	9.624E-09	9.624E-09
155	0.000E+00	5.989E-11	5.989E-11	5.989E-11	5.989E-11	5.989E-11	5.989E-11	5.989E-11
156	0.000E+00	2.633E-11	2.632E-11	2.632E-11	2.632E-11	2.632E-11	2.632E-11	2.632E-11
157	0.000E+00	1.467E-11	1.467E-11	1.467E-11	1.467E-11	1.467E-11	1.467E-11	1.467E-11
158	0.000E+00	7.326E-12	7.326E-12	7.326E-12	7.326E-12	7.326E-12	7.326E-12	7.326E-12
159	5.370E-09	5.354E-09	5.354E-09	5.354E-09	5.354E-09	5.354E-09	5.354E-09	5.354E-09
160	0.000E+00	1.989E-11	1.989E-11	1.989E-11	1.989E-11	1.989E-11	1.989E-11	1.989E-11
161	0.000E+00	6.106E-13	6.105E-13	6.105E-13	6.105E-13	6.105E-13	6.105E-13	6.105E-13
162	0.000E+00	2.384E-13	2.384E-13	2.384E-13	2.384E-13	2.384E-13	2.384E-13	2.384E-13
163	0.000E+00	1.335E-13	1.334E-13	1.334E-13	1.335E-13	1.335E-13	1.335E-13	1.335E-13
164	0.000E+00	8.006E-14	8.009E-14	8.009E-14	8.009E-14	8.009E-14	8.009E-14	8.009E-14
165	0.000E+00	4.618E-14	4.615E-14	4.615E-14	4.615E-14	4.615E-14	4.615E-14	4.615E-14
166	0.000E+00	2.984E-14	2.984E-14	2.984E-14	2.984E-14	2.984E-14	2.984E-14	2.984E-14
167	0.000E+00	2.073E-14	2.073E-14	2.073E-14	2.073E-14	2.073E-14	2.073E-14	2.073E-14
168	2.700E-11	2.758E-11	2.758E-11	2.758E-11	2.758E-11	2.758E-11	2.758E-11	2.758E-11
169	0.000E+00	8.686E-14	8.686E-14	8.686E-14	8.686E-14	8.686E-14	8.686E-14	8.686E-14
170	6.545E-10	0.000E+00	0.000E+00	0.000E+00	0.000E+00	0.000E+00	0.000E+00	0.000E+00
171	3.092E-09	3.088E-09	3.088E-09	3.088E-09	3.088E-09	3.088E-09	3.088E-09	3.088E-09
172	4.758E-09	4.763E-09	4.763E-09	4.763E-09	4.763E-09	4.763E-09	4.763E-09	4.763E-09
173	3.534E-09	3.539E-09	3.539E-09	3.539E-09	3.539E-09	3.539E-09	3.539E-09	3.539E-09

A	Precursor	1 s	1 min	1 h	1 d	1 wk	1 mo	1 yr
174	7.100E-09	7.091E-09	7.091E-09	7.091E-09	7.091E-09	7.091E-09	7.091E-09	7.091E-09
175	3.213E-09	3.206E-09	3.206E-09	3.206E-09	3.206E-09	3.206E-09	3.206E-09	3.206E-09
176	5.274E-09	5.240E-09	5.240E-09	5.240E-09	5.240E-09	5.240E-09	5.240E-09	5.240E-09
177	8.259E-09	8.161E-09	8.161E-09	8.161E-09	8.161E-09	8.161E-09	8.161E-09	8.161E-09
178	1.211E-08	1.209E-08	1.209E-08	1.209E-08	1.209E-08	1.209E-08	1.209E-08	1.209E-08
179	6.048E-09	6.063E-09	6.063E-09	6.063E-09	6.063E-09	6.063E-09	6.063E-09	6.063E-09
180	1.560E-08	1.572E-08	1.572E-08	1.572E-08	1.572E-08	1.572E-08	1.572E-08	1.572E-08
181	1.209E-08	1.207E-08	1.207E-08	1.207E-08	1.207E-08	1.207E-08	1.207E-08	1.207E-08
182	3.586E-09	3.572E-09	3.572E-09	3.572E-09	3.572E-09	3.572E-09	3.572E-09	3.572E-09
183	1.937E-09	1.929E-09	1.929E-09	1.929E-09	1.929E-09	1.929E-09	1.929E-09	1.929E-09
184	4.147E-09	4.147E-09	4.147E-09	4.147E-09	4.147E-09	4.147E-09	4.147E-09	4.147E-09
185	0.000E+00	3.470E-12	3.470E-12	3.470E-12	3.470E-12	3.470E-12	3.470E-12	3.470E-12
186	3.848E-09	3.888E-09	3.888E-09	3.888E-09	3.888E-09	3.888E-09	3.888E-09	3.888E-09
187	0.000E+00	3.050E-12	3.050E-12	3.050E-12	3.050E-12	3.050E-12	3.050E-12	3.050E-12
188	0.000E+00	2.290E-16	2.290E-16	2.290E-16	2.290E-16	2.290E-16	2.290E-16	2.290E-16
189	0.000E+00	1.002E-20	1.002E-20	1.002E-20	1.002E-20	1.002E-20	1.002E-20	1.002E-20
190	0.000E+00	1.233E-33	1.233E-33	1.233E-33	1.233E-33	1.233E-33	1.233E-33	1.233E-33
191	0.000E+00	8.072E-30	8.072E-30	8.072E-30	8.072E-30	8.072E-30	8.072E-30	8.072E-30
192	0.000E+00	1.116E-26	1.116E-26	1.116E-26	1.116E-26	1.116E-26	1.116E-26	1.116E-26
193	0.000E+00	1.784E-22	1.784E-22	1.784E-22	1.784E-22	1.784E-22	1.784E-22	1.784E-22
194	0.000E+00	9.489E-20	9.490E-20	9.489E-20	9.489E-20	9.489E-20	9.490E-20	9.490E-20
195	0.000E+00	9.494E-19	9.494E-19	9.494E-19	9.495E-19	9.494E-19	9.494E-19	9.495E-19
196	0.000E+00	1.318E-15	1.318E-15	1.318E-15	1.318E-15	1.318E-15	1.318E-15	1.318E-15
197	4.060E-11	4.053E-11	4.053E-11	4.053E-11	4.053E-11	4.053E-11	4.053E-11	4.053E-11
198	0.000E+00	6.754E-14	6.754E-14	6.754E-14	6.754E-14	6.754E-14	6.754E-14	6.754E-14

A	Precursor	1 s	1 min	1 h	1 d	1 wk	1 mo	1 yr
199	0.000E+00	5.145E-17	5.145E-17	5.145E-17	5.145E-17	5.145E-17	5.145E-17	5.145E-17
200	0.000E+00	9.216E-21	9.216E-21	9.216E-21	9.216E-21	9.216E-21	9.216E-21	9.216E-21
201	0.000E+00	3.149E-35	3.149E-35	3.149E-35	3.149E-35	3.149E-35	3.149E-35	3.149E-35
202	0.000E+00	2.917E-39	2.917E-39	2.917E-39	2.917E-39	2.917E-39	2.917E-39	2.917E-39
203	0.000E+00	9.105E-44	9.105E-44	9.100E-44	9.027E-44	9.027E-44	9.027E-44	9.027E-44
204	0.000E+00	0.000E+00	0.000E+00	0.000E+00	0.000E+00	0.000E+00	0.000E+00	0.000E+00
205	0.000E+00	0.000E+00	0.000E+00	0.000E+00	0.000E+00	0.000E+00	0.000E+00	0.000E+00
206	0.000E+00	0.000E+00	3.775E-44	2.639E-39	5.724E-34	1.083E-30	2.116E-28	9.433E-25
207	0.000E+00	2.162E-45	6.125E-37	1.638E-30	8.202E-27	2.149E-23	7.124E-21	8.953E-18
208	0.000E+00	2.584E-44	1.508E-37	1.184E-29	7.002E-25	7.842E-23	1.267E-21	1.785E-19
209	0.000E+00	0.000E+00	2.288E-40	5.811E-32	5.311E-27	1.755E-24	9.046E-23	5.163E-20
210	0.000E+00	3.385E-32	9.482E-29	1.194E-26	2.320E-25	1.481E-24	5.759E-24	2.726E-22
211	0.000E+00	2.799E-38	1.497E-33	4.838E-30	1.031E-27	5.049E-25	3.315E-23	2.149E-21
212	0.000E+00	7.491E-37	2.331E-31	3.858E-27	1.532E-24	1.575E-23	5.274E-23	7.671E-22
213	0.000E+00	9.163E-45	7.422E-38	2.726E-31	7.409E-28	3.319E-26	3.438E-25	1.541E-23
214	0.000E+00	1.036E-34	3.911E-33	1.118E-32	1.507E-29	5.896E-28	4.848E-27	7.133E-26
215	0.000E+00	2.175E-40	1.428E-37	9.496E-36	8.969E-34	3.994E-31	2.622E-29	1.699E-27
216	0.000E+00	5.509E-37	2.358E-33	4.659E-31	1.088E-29	5.987E-29	1.888E-28	2.702E-27
217	0.000E+00	1.675E-45	2.334E-40	1.443E-35	1.012E-32	3.993E-31	4.136E-30	1.853E-28
218	0.000E+00	3.692E-33	1.394E-31	1.613E-31	1.258E-30	3.996E-29	3.277E-28	4.821E-27
219	0.000E+00	4.924E-37	3.235E-34	2.151E-32	2.031E-30	9.045E-28	5.939E-26	3.849E-24
220	0.000E+00	3.217E-34	9.195E-31	1.819E-28	4.248E-27	2.338E-26	7.373E-26	1.055E-24
221	0.000E+00	1.747E-41	2.164E-36	1.338E-31	9.380E-29	3.702E-27	3.834E-26	1.718E-24
222	0.000E+00	4.090E-30	1.466E-28	1.716E-28	2.172E-27	7.220E-26	5.928E-25	8.725E-24
223	0.000E+00	1.513E-30	9.081E-29	5.493E-27	5.304E-25	2.300E-22	1.508E-20	9.773E-19

A	Precursor	1 s	1 min	1 h	1 d	1 wk	1 mo	1 yr
224	0.000E+00	3.000E-28	1.800E-26	1.077E-24	2.460E-23	1.354E-22	4.269E-22	6.112E-21
225	0.000E+00	1.784E-28	8.736E-27	5.222E-25	1.253E-23	8.747E-23	4.040E-22	1.317E-20
226	0.000E+00	1.370E-25	2.661E-24	1.541E-22	3.696E-21	2.587E-20	1.125E-19	1.358E-18
227	0.000E+00	1.859E-21	1.859E-21	3.087E-21	5.827E-19	1.200E-17	6.325E-17	7.855E-16
228	0.000E+00	6.771E-20	6.773E-20	6.890E-20	9.642E-20	2.687E-19	9.407E-19	1.036E-17
229	0.000E+00	4.933E-17	4.933E-17	4.933E-17	4.939E-17	5.209E-17	9.275E-17	1.570E-15
230	0.000E+00	1.494E-13	1.494E-13	1.494E-13	1.494E-13	1.494E-13	1.495E-13	1.512E-13
231	0.000E+00	3.846E-11	3.846E-11	3.846E-11	3.846E-11	3.846E-11	3.846E-11	3.846E-11
232	2.009E-07	2.002E-07	2.002E-07	2.002E-07	2.002E-07	2.002E-07	2.002E-07	2.002E-07
233	0.000E+00	3.978E-10	3.977E-10	3.978E-10	3.978E-10	3.977E-10	3.977E-10	3.977E-10
234	2.080E-12	6.309E-10	6.309E-10	6.309E-10	6.309E-10	6.309E-10	6.309E-10	6.309E-10
235	2.775E-10	1.622E-06	1.622E-06	1.622E-06	1.622E-06	1.622E-06	1.622E-06	1.622E-06
236	0.000E+00	3.328E-09	3.328E-09	3.328E-09	3.328E-09	3.328E-09	3.328E-09	3.328E-09
237	0.000E+00	1.328E-09	1.328E-09	1.328E-09	1.328E-09	1.328E-09	1.328E-09	1.328E-09
238	3.824E-08	7.247E-06	7.247E-06	7.247E-06	7.247E-06	7.247E-06	7.247E-06	7.247E-06
239	0.000E+00	1.085E-08	1.085E-08	1.085E-08	1.085E-08	1.085E-08	1.085E-08	1.085E-08
240	0.000E+00	9.909E-12	9.909E-12	9.909E-12	9.909E-12	9.909E-12	9.909E-12	9.908E-12
241	0.000E+00	7.710E-15	7.710E-15	7.710E-15	7.709E-15	7.710E-15	7.710E-15	7.710E-15
242	0.000E+00	1.047E-36	1.047E-36	1.047E-36	1.047E-36	1.047E-36	1.047E-36	1.047E-36
243	0.000E+00	2.847E-40	2.847E-40	2.847E-40	2.847E-40	2.847E-40	2.847E-40	2.847E-40

AV.4 WGU IND Mass Fraction Results by Atomic Number (Z) and Time

Z	Precursor	1 s	1 min	1 h	1 d	1 wk	1 mo	1 yr
1	1.902E-02	1.903E-02	1.903E-02	1.903E-02	1.903E-02	1.903E-02	1.903E-02	1.903E-02
2	0.000E+00	2.913E-05	2.913E-05	2.913E-05	2.913E-05	2.913E-05	2.913E-05	2.913E-05
3	0.000E+00	1.892E-12	1.913E-12	1.913E-12	1.913E-12	1.913E-12	1.913E-12	1.913E-12
4	0.000E+00	1.200E-09	1.200E-09	1.200E-09	1.200E-09	1.200E-09	1.200E-09	1.200E-09
5	0.000E+00	7.632E-08	7.632E-08	7.632E-08	7.632E-08	7.632E-08	7.632E-08	7.632E-08
6	0.000E+00	1.148E-04	1.148E-04	1.148E-04	1.148E-04	1.148E-04	1.148E-04	1.148E-04
7	0.000E+00	6.503E-05	6.492E-05	6.492E-05	6.492E-05	6.492E-05	6.492E-05	6.492E-05
8	5.607E-01	5.605E-01	5.605E-01	5.605E-01	5.605E-01	5.605E-01	5.605E-01	5.605E-01
9	0.000E+00	1.275E-07	4.835E-09	1.916E-09	1.916E-09	1.916E-09	1.916E-09	1.916E-09
10	0.000E+00	4.820E-07	3.242E-07	1.865E-07	1.865E-07	1.865E-07	1.865E-07	1.866E-07
11	2.055E-02	2.054E-02	2.054E-02	2.054E-02	2.054E-02	2.054E-02	2.054E-02	2.054E-02
12	6.050E-04	6.182E-04	6.179E-04	6.140E-04	6.143E-04	6.145E-04	6.145E-04	6.145E-04
13	6.379E-02	6.381E-02	6.380E-02	6.379E-02	6.379E-02	6.379E-02	6.379E-02	6.379E-02
14	2.935E-01	2.934E-01	2.934E-01	2.934E-01	2.934E-01	2.934E-01	2.934E-01	2.934E-01
15	6.200E-05	6.193E-05	6.194E-05	6.197E-05	6.210E-05	6.210E-05	6.210E-05	6.210E-05
16	0.000E+00	1.015E-08	1.015E-08	1.015E-08	1.024E-08	1.070E-08	1.165E-08	1.213E-08
17	0.000E+00	5.047E-06	5.046E-06	5.040E-06	5.074E-06	5.298E-06	5.959E-06	7.079E-06
18	0.000E+00	1.519E-04	1.519E-04	1.519E-04	1.518E-04	1.516E-04	1.509E-04	1.494E-04
19	3.135E-02	3.120E-02	3.120E-02	3.120E-02	3.120E-02	3.120E-02	3.120E-02	3.120E-02
20	2.710E-03	2.703E-03	2.703E-03	2.703E-03	2.703E-03	2.703E-03	2.703E-03	2.703E-03
21	1.852E-08	5.897E-08	5.896E-08	5.860E-08	5.322E-08	3.689E-08	2.911E-08	2.167E-08
22	9.826E-04	9.824E-04	9.824E-04	9.824E-04	9.824E-04	9.824E-04	9.824E-04	9.824E-04
23	0.000E+00	6.098E-10	5.667E-10	5.228E-10	6.095E-10	1.105E-09	2.463E-09	4.165E-09

Z	Precursor	1 s	1 min	1 h	1 d	1 wk	1 mo	1 yr
24	0.000E+00	3.075E-08	3.002E-08	2.666E-08	2.757E-08	3.323E-08	5.513E-08	2.818E-07
25	5.765E-04	5.770E-04	5.770E-04	5.770E-04	5.769E-04	5.769E-04	5.769E-04	5.766E-04
26	6.176E-03	6.175E-03	6.175E-03	6.175E-03	6.175E-03	6.175E-03	6.175E-03	6.175E-03
27	2.960E-09	2.962E-09	2.962E-09	2.962E-09	2.977E-09	3.064E-09	3.333E-09	3.942E-09
28	0.000E+00	1.667E-10	1.668E-10	1.737E-10	2.632E-10	2.993E-10	2.993E-10	2.988E-10
29	0.000E+00	4.285E-07	4.285E-07	4.285E-07	4.283E-07	4.283E-07	4.283E-07	4.283E-07
30	4.729E-07	4.726E-07	4.726E-07	4.726E-07	4.727E-07	4.727E-07	4.727E-07	4.727E-07
31	0.000E+00	2.062E-11	1.781E-12	3.664E-12	7.263E-12	7.536E-12	7.534E-12	7.534E-12
32	0.000E+00	1.310E-10	2.617E-11	1.344E-11	3.992E-12	2.981E-12	3.000E-12	3.008E-12
33	1.700E-08	1.732E-08	1.705E-08	1.700E-08	1.700E-08	1.699E-08	1.699E-08	1.699E-08
34	0.000E+00	1.052E-09	5.709E-10	1.590E-10	1.461E-10	1.558E-10	1.563E-10	1.563E-10
35	0.000E+00	1.625E-09	8.171E-10	2.242E-10	4.653E-11	4.634E-11	4.634E-11	4.634E-11
36	0.000E+00	3.453E-09	2.594E-09	2.018E-09	1.003E-09	9.950E-10	9.951E-10	9.911E-10
37	1.413E-06	1.415E-06	1.414E-06	1.413E-06	1.413E-06	1.413E-06	1.413E-06	1.412E-06
38	4.618E-07	4.666E-07	4.671E-07	4.669E-07	4.653E-07	4.651E-07	4.650E-07	4.645E-07
39	2.640E-07	2.684E-07	2.664E-07	2.663E-07	2.656E-07	2.654E-07	2.654E-07	2.650E-07
40	1.691E-06	1.697E-06	1.695E-06	1.698E-06	1.700E-06	1.700E-06	1.699E-06	1.699E-06
41	2.080E-07	2.115E-07	2.087E-07	2.081E-07	2.081E-07	2.081E-07	2.084E-07	2.080E-07
42	1.269E-08	1.563E-08	2.309E-08	1.906E-08	1.961E-08	1.914E-08	1.893E-08	2.062E-08
43	0.000E+00	3.005E-10	2.041E-09	4.714E-10	4.563E-10	1.699E-09	2.049E-09	2.050E-09
44	0.000E+00	1.267E-10	1.070E-09	7.423E-09	7.209E-09	7.018E-09	6.504E-09	5.310E-09
45	0.000E+00	6.673E-11	9.223E-11	1.673E-10	6.694E-10	2.305E-10	6.827E-10	1.639E-09
46	0.000E+00	8.704E-11	1.680E-10	5.671E-10	8.189E-10	1.411E-09	1.474E-09	1.711E-09
47	0.000E+00	5.205E-11	6.609E-11	5.436E-11	8.842E-11	9.324E-11	7.671E-11	7.461E-11
48	0.000E+00	1.014E-10	8.301E-11	1.174E-10	1.177E-10	1.337E-10	1.470E-10	1.482E-10

Z	Precursor	1 s	1 min	1 h	1 d	1 wk	1 mo	1 yr
49	0.000E+00	1.605E-10	2.983E-11	6.859E-12	6.644E-12	2.189E-11	2.510E-11	2.609E-11
50	0.000E+00	2.792E-09	1.901E-09	3.866E-10	2.608E-10	2.441E-10	2.384E-10	2.362E-10
51	4.526E-09	8.422E-09	8.234E-09	5.410E-09	4.715E-09	4.652E-09	4.622E-09	4.613E-09
52	0.000E+00	7.730E-09	6.033E-09	5.340E-09	2.984E-09	1.616E-09	1.111E-09	1.067E-09
53	0.000E+00	6.163E-09	5.220E-09	7.236E-09	3.322E-09	1.270E-09	5.943E-10	5.376E-10
54	0.000E+00	7.782E-09	7.272E-09	4.532E-09	9.460E-09	1.034E-08	1.015E-08	1.020E-08
55	4.229E-08	4.763E-08	4.692E-08	4.635E-08	4.721E-08	4.982E-08	5.122E-08	5.122E-08
56	1.954E-06	1.961E-06	1.960E-06	1.961E-06	1.959E-06	1.959E-06	1.957E-06	1.957E-06
57	7.061E-07	7.093E-07	7.099E-07	7.108E-07	7.090E-07	7.090E-07	7.088E-07	7.088E-07
58	1.486E-06	1.487E-06	1.491E-06	1.491E-06	1.494E-06	1.493E-06	1.494E-06	1.492E-06
59	0.000E+00	6.865E-10	1.796E-09	2.250E-09	1.134E-09	2.281E-09	1.936E-09	2.811E-09
60	2.157E-07	2.160E-07	2.169E-07	2.199E-07	2.216E-07	2.219E-07	2.228E-07	2.245E-07
61	0.000E+00	4.619E-11	1.975E-10	5.234E-10	7.711E-10	5.134E-10	1.015E-09	9.376E-10
62	4.103E-08	4.103E-08	4.111E-08	4.147E-08	4.171E-08	4.221E-08	4.229E-08	4.255E-08
63	2.397E-09	2.398E-09	2.403E-09	2.468E-09	2.531E-09	2.631E-09	2.631E-09	2.619E-09
64	0.000E+00	2.191E-13	1.723E-12	9.241E-12	2.284E-11	3.302E-11	4.652E-11	6.127E-11
65	5.370E-09	5.369E-09	5.370E-09	5.370E-09	5.372E-09	5.372E-09	5.368E-09	5.355E-09
66	0.000E+00	1.493E-14	7.301E-14	5.010E-13	7.095E-13	1.959E-12	5.679E-12	1.886E-11
67	0.000E+00	2.730E-15	1.108E-14	2.834E-14	5.027E-14	4.947E-14	4.619E-14	4.616E-14
68	0.000E+00	3.964E-16	5.113E-15	3.304E-14	4.800E-14	6.127E-14	6.780E-14	6.713E-14
69	0.000E+00	5.479E-16	5.679E-16	1.291E-15	5.928E-15	1.807E-14	4.762E-14	8.860E-14
70	2.195E-08	2.194E-08	2.194E-08	2.194E-08	2.194E-08	2.194E-08	2.194E-08	2.194E-08
71	3.299E-09	3.299E-09	3.299E-09	3.297E-09	3.293E-09	3.295E-09	3.296E-09	3.296E-09
72	4.441E-08	4.440E-08	4.440E-08	4.440E-08	4.440E-08	4.440E-08	4.440E-08	4.440E-08
73	1.210E-08	1.209E-08	1.209E-08	1.209E-08	1.209E-08	1.209E-08	1.209E-08	1.208E-08

Z	Precursor	1 s	1 min	1 h	1 d	1 wk	1 mo	1 yr
74	1.353E-08	1.353E-08	1.353E-08	1.353E-08	1.353E-08	1.353E-08	1.353E-08	1.355E-08
75	0.000E+00	2.482E-17	1.489E-15	8.816E-14	1.557E-12	3.243E-12	3.900E-12	6.401E-12
76	0.000E+00	2.040E-27	6.893E-25	2.117E-21	8.256E-19	1.320E-17	5.802E-17	2.228E-16
77	0.000E+00	9.506E-20	9.501E-20	9.171E-20	4.022E-20	4.044E-22	1.784E-22	1.784E-22
78	0.000E+00	3.524E-18	3.617E-18	9.183E-18	1.320E-16	6.681E-16	1.186E-15	1.227E-15
79	4.060E-11	4.060E-11	4.060E-11	4.060E-11	4.058E-11	4.054E-11	4.053E-11	4.053E-11
80	0.000E+00	2.011E-19	1.206E-17	7.201E-16	1.532E-14	5.645E-14	6.765E-14	6.768E-14
81	0.000E+00	2.162E-45	6.467E-37	1.447E-30	2.312E-27	8.621E-26	4.128E-24	2.634E-22
82	0.000E+00	3.385E-32	9.506E-29	1.575E-26	2.352E-24	1.163E-22	8.474E-21	9.134E-18
83	0.000E+00	1.597E-41	7.588E-35	6.993E-29	1.255E-25	3.071E-24	9.583E-23	5.177E-20
84	0.000E+00	1.041E-34	6.269E-33	4.722E-31	1.248E-29	2.194E-28	5.333E-27	1.870E-24
85	0.000E+00	1.675E-45	2.335E-40	1.444E-35	1.012E-32	3.994E-31	4.136E-30	1.854E-28
86	0.000E+00	4.016E-33	1.060E-30	1.859E-28	6.279E-27	9.637E-26	7.259E-25	1.363E-23
87	0.000E+00	3.473E-36	1.240E-32	3.209E-29	1.469E-26	3.163E-25	1.684E-24	2.213E-23
88	0.000E+00	4.298E-20	4.298E-20	4.308E-20	7.142E-20	2.531E-19	9.738E-19	1.153E-17
89	0.000E+00	5.082E-25	3.058E-23	2.391E-21	5.826E-19	1.200E-17	6.320E-17	7.838E-16
90	2.009E-07	2.006E-07	2.006E-07	2.003E-07	2.002E-07	2.002E-07	2.002E-07	2.002E-07
91	0.000E+00	2.325E-13	1.221E-11	3.368E-10	4.062E-10	3.704E-10	2.205E-10	3.849E-11
92	3.520E-08	8.885E-06	8.885E-06	8.876E-06	8.874E-06	8.874E-06	8.873E-06	8.873E-06
93	0.000E+00	5.346E-12	3.161E-10	8.945E-09	8.272E-09	2.074E-09	1.271E-09	1.328E-09
94	0.000E+00	9.216E-18	3.285E-14	7.083E-11	2.717E-09	9.469E-09	1.086E-08	1.086E-08
95	0.000E+00	3.789E-30	7.817E-25	2.439E-20	1.004E-18	7.144E-18	3.108E-17	3.647E-16
96	0.000E+00	0.000E+00	0.000E+00	0.000E+00	0.000E+00	0.000E+00	0.000E+00	0.000E+00
97	0.000E+00	0.000E+00	0.000E+00	0.000E+00	0.000E+00	0.000E+00	0.000E+00	0.000E+00
98	0.000E+00	0.000E+00	0.000E+00	0.000E+00	0.000E+00	0.000E+00	0.000E+00	0.000E+00

VITA

R. Boone Gilbreath was born 6 May 1986 in Fort Smith, Arkansas. Boone grew up in nearby Greenwood, Arkansas where he graduated from Greenwood High School in 2004. He received the A.S. degree in nuclear technology from Arkansas Tech University, Russellville, Arkansas in 2008; the B.S. degree in mechanical engineering from Arkansas Tech University, Russellville, Arkansas in 2008; and the M.S. degree in nuclear engineering from the University of Tennessee, Knoxville, Tennessee in 2017. Boone is a Captain in the United States Army with over eight years of service as an ordnance and multifunctional logistics officer. His military service includes a deployment to Afghanistan from 2010 to 2011 in support of Operation Enduring Freedom. In 2014, he was selected to serve in the Army's nuclear and counterproliferation functional area, FA 52. CPT Gilbreath will assume duty as an instructor in the Department of Physics and Nuclear Engineering at the United States Military Academy, West Point, New York in June 2017.